The Annealing of SCT Silicon Microstrip Sensors and the Search for the Standard Model Higgs Boson in the Four Muon Final State in the ATLAS Detector

Thesis submitted in accordance with the requirements of
the University of Liverpool for the degree of Doctor in Philosophy
by

Craig Wiglesworth

October 2010

Abstract

In order for the ATLAS experiment to achieve its physics potential its detector components must operate stably and reliably over their full lifetimes. However, in the harsh experimental environment of the LHC the inner detector will be subjected to extreme levels of radiation, which can have a significant impact on the performance of its silicon sensors. This thesis presents new measurements of the evolution of both the depletion voltage and the charge collection with annealing time in an irradiated silicon microstrip sensor of the SCT. The measurements are compared to the predictions of the *Second Order* and *Hamburg* radiation damage parameterisations, which show significant variation for long periods of annealing. Determining which of the two parameterisations best describes the data will allow for a more accurate prediction of the long-term performance of the SCT using the most up-to-date operational information from the LHC and the ATLAS detector.

Within the physics programme of the ATLAS experiment the discovery or exclusion of the Standard Model Higgs boson is of high priority. In searching for this elusive particle the four muon final state will be of particular importance as it provides one of the cleanest experimental signatures. This thesis presents the ATLAS experiment's sensitivity prospects for the Standard Model Higgs boson in the four muon final state with 1 fb^{-1} of 7 TeV collision data. Any potential observation of the Standard Model Higgs boson in this decay channel will depend crucially upon the performance of the tracking detectors and, in particular, their alignment precision. This thesis therefore also addresses the impact of detector misalignments on the muon identification and reconstruction performance and the subsequent impact on the sensitivity of the ATLAS detector to the Standard Model Higgs boson in the four muon final state.

Acknowledgements

I would like to thank both the University of Liverpool High Energy Physics Group and the ATLAS Collaboration for their help and support. In particular my supervisors Joost Vossebeld and Steve Maxfield, Tony Affolder, Phil Allport, John Bland, Henry Brown, Gianluigi Casse, Valery Chmill, Paul Dervan, Rob Fay, Carl Gwilliam, Helen Hayward, Sandra Horvat, Steve Jones, Carlo Schiavi, Ilya Tsurin and Mike Wormald. I would also like to thank Dave Muskett, George Sim and the Science and Technology Facilities Council. Thank you.

Contents

1 Introduction **1**

2 The LHC and the ATLAS Experiment **4**

2.1 The ATLAS Experiment 5

2.2 The Inner Detector 7

2.2.1 The Pixel Detector 10

2.2.2 The Semiconductor Tracker 11

2.2.3 The Transition Radiation Tracker 11

2.3 The Electromagnetic Calorimeter 12

2.4 The Hadronic Calorimeters 14

2.5 The Muon Spectrometer 16

2.6 The Trigger 19

3 The Annealing of SCT Silicon Microstrip Sensors **22**

3.1 The SCT Silicon Microstrip Sensors 23

3.2 Radiation Damage in Silicon Sensors 25

3.2.1 Displacement Damage 26

3.2.2 The NIEL Scaling Hypothesis 27

3.3 The Effects of Radiation Damage in Silicon Sensors 28

3.3.1 Signal Charge Trapping 30

3.3.2 Effective Doping Concentration 30

3.4 Review of Radiation Damage Parameterisations 32

3.4.1 Stable Damage 33

3.4.2 Beneficial Annealing 33

3.4.3 Reverse Annealing 34

3.5 Predicted Evolution of Sensor Properties 37

3.6 Measured Evolution of Sensor Properties 38
3.6.1 Depletion Voltage 39
3.6.2 Charge Collection Efficiency 42
3.7 Implications for the Long-Term Operation of the SCT 45

4 The Standard Model Higgs Boson **50**
4.1 The Electroweak Theory and the Higgs Mechanism 53
4.2 Constraints on the Standard Model Higgs Boson Mass 56
4.3 The Standard Model Higgs Boson at the LHC 59
4.3.1 Production Mechanisms 60
4.3.2 Decay Channels 62
4.4 ATLAS Sensitivity to the Standard Model Higgs Boson 63

5 Muon Identification and Reconstruction **69**
5.1 Muon Identification 70
5.1.1 Combined Muons 70
5.1.2 Tagged Muons 70
5.1.3 Standalone Muons 71
5.2 Muon Reconstruction 71
5.2.1 Inner Detector Tracks 74
5.2.2 Muon Spectrometer Tracks 75
5.2.3 Combined Muon Tracks 76
5.2.4 Tagged Inner Detector Tracks 77
5.3 Muon Identification and Reconstruction Performance 78
5.3.1 Identification Efficiency 79
5.3.2 $1/p_{\mathrm{T}}$ Scale 80
5.3.3 $1/p_{\mathrm{T}}$ Resolution 80

6 Sensitivity to $H \to ZZ^{(*)} \to 4\mu$ at $\sqrt{s} = 7$ TeV **85**
6.1 Monte Carlo Samples 87
6.1.1 Signals 87
6.1.2 Backgrounds 87
6.2 Triggering 89
6.3 Event Selection 89

6.3.1 Preselection . . . 91
6.3.2 Kinematic Reconstruction . . . 91
6.3.3 Background Rejection . . . 91
6.4 Results . . . 98
6.5 Systematic Uncertainties . . . 100
6.5.1 Theoretical . . . 106
6.5.2 Experimental . . . 106
6.6 Expected Exclusion Limits . . . 106

7 Impact of Detector Misalignments on the Sensitivity to $H \to ZZ^* \to 4\mu$ 109
7.1 Detector Misalignments . . . 110
7.1.1 Inner Detector . . . 111
7.1.2 Muon Spectrometer . . . 112
7.2 Muon Identification and Reconstruction Performance . . . 114
7.2.1 Identification Efficiency . . . 114
7.2.2 $1/p_{\mathrm{T}}$ Scale . . . 116
7.2.3 $1/p_{\mathrm{T}}$ Resolution . . . 116
7.3 Sensitivity to the Relative Misalignment of the Tracking Detectors . . . 123
7.4 Impact on the Sensitivity to $H \to ZZ^* \to 4\mu$ . . . 126
7.4.1 Z Mass Width . . . 126
7.4.2 H Mass Width . . . 127
7.4.3 Transverse Impact Parameter Significance . . . 128
7.4.4 Signal Selection Efficiency . . . 131
7.5 Relative Performance of the Tracking Detectors . . . 133
7.6 Summary . . . 137

8 Conclusion 138

Bibliography 146

Chapter 1

Introduction

The Large Hadron Collider (LHC) at CERN is now the world's highest energy particle collider and will soon address some of the most fundamental, unresolved questions in particle physics. The ATLAS experiment, one of four major experiments at the LHC, will analyse the collisions in order to test the validity of our current theoretical description of particles and their interactions, known as the Standard Model. In particular, one of the main objectives is the discovery or exclusion of the Standard Model Higgs boson. This elusive particle is the only remaining particle of the Standard Model that is yet to be discovered. In addition, searches will also be performed for more exotic phenomena beyond the Standard Model, such as supersymmetric particles, mini black holes and extra dimensions. However, the high energies required to reach the unexplored regions of particle physics and the high luminosities required to observe rare physics processes lead to a harsh experimental environment in which particle detectors can experience significant radiation damage. In order for the ATLAS experiment to achieve its physics potential its detector components must operate stably and reliably over their full lifetimes.

This first part of this thesis is concerned with the problems of radiation damage and annealing in the silicon microstrip sensors of the SemiConductor Tracker (SCT). In order to address these issues I designed a programme of accelerated annealing measurements in which the performance of irradiated silicon microstrip sensors was monitored following successive periods of exposure to high temperatures. Throughout the experimental programme I was responsible for both the preparation and maintenance of the equipment as well as the measurements that were taken after each period of annealing.

I also then analysed the collected data to determine the evolution in the performance of the silicon microstrip sensors with annealing time and developed the software necessary to compare the experimental observations to the predictions of two different radiation damage parameterisations.

The second part of this thesis is concerned with the ATLAS experiment's sensitivity prospects for the Standard Model Higgs boson in the four muon final state and, in particular the impact of detector misalignments on the sensitivity of the ATLAS detector. For these studies I had to produce the required misaligned Monte Carlo samples on the Grid[1] using the most up-to-date predictions for the alignment precisions of the tracking detectors. I was also involved in the development and maintenance of the OSCAR software package [1], which provides a number of tools and routines for performing various physics analyses within the ATLAS software framework. I then used this package to study and run the full $H \rightarrow ZZ^{(*)} \rightarrow 4\mu$ analysis chain to determine the sensitivity of the ATLAS detector to the four muon final state across a broad range of possible Standard Model Higgs boson masses.

The outline of the thesis is as follows: Chapter 2 provides an introduction to the LHC and the ATLAS experiment. The objectives of the experiment are reviewed and the main features of the ATLAS detector are discussed. Chapter 3 describes the silicon microstrip sensors of the SCT and the consequences of exposure to extreme levels of radiation. New measurements of the evolution of both the depletion voltage and the charge collection with annealing time are presented. The measurements are compared to the predictions of different radiation damage parameterisations and the implications for the long-term operation of the SCT are discussed. Chapter 4 provides a brief description of the Standard Model of particle physics and, in particular, the role of the Higgs boson. The experimental and theoretical constraints on the mass of the Standard Model Higgs boson are reviewed and the ATLAS experiment's sensitivity prospects for the Standard Model Higgs boson with 30 fb^{-1} of 14 TeV collision data are presented. Chapter 5 describes the muon identification and reconstruction procedures in the ATLAS experiment. The different identification strategies are outlined and the various reconstruction algorithms are discussed. The expected muon identification and reconstruction performance, based on simulated $H \rightarrow ZZ^* \rightarrow 4\mu$ events with $m_H = 130$ GeV,

[1]The Worldwide LHC Computing Grid

is also presented. Chapter 6 presents the ATLAS experiment's sensitivity prospects for the Standard Model Higgs boson in the four muon final state with 1 fb^{-1} of 7 TeV collision data. The analysis strategy and the related systematic uncertainties are discussed and the expected exclusion limits for the Standard Model Higgs boson in the four lepton (e,μ) final state are presented. Finally, Chapter 7 describes the impact of detector misalignments on the muon identification and reconstruction performance and the subsequent impact on the sensitivity of the ATLAS experiment to the Standard Model Higgs boson in the four muon final state. A potential track-based method of identifying relative misalignments between the inner detector and the muon spectrometer is also discussed.

Chapter 2

The LHC and the ATLAS Experiment

The LHC [2] is a two ring, superconducting, hadron accelerator and collider located at the site of the European Organisation for Nuclear Research (CERN), near Geneva. It occupies the 26.7 km underground tunnel that previously housed the Large Electron Positron (LEP) collider and uses CERN's (upgraded) accelerator complex as injection chain. During nominal operation it will collide counter-rotating proton beams with a centre-of-mass energy of 14 TeV at a luminosity of 10^{34} $\mathrm{cm}^{-2}\mathrm{s}^{-1}$. The beams consist of 2808 proton bunches with 1.15×10^{11} protons in each bunch and collide with a bunch crossing frequency of 40 MHz. In addition to proton beams, the LHC will also accelerate and collide heavy ion (Pb) beams with an energy of 2.76 TeV per nucleon at a luminosity of 10^{27} $\mathrm{cm}^{-2}\mathrm{s}^{-1}$.

Four major experiments each have a dedicated detector built around one of the four interaction points at the LHC, as shown in Figure 2.1: the ATLAS experiment [3, 4] and the CMS experiment [5] are both general purpose experiments, the LHCb experiment [6] is devoted to precision measurements of CP violation and rare decays of B hadrons and the ALICE experiment [7] will study the physics of strongly interacting matter and the quark-gluon plasma. The LHC also hosts two smaller experiments: the LHCf experiment [8] has detectors either side of the ATLAS detector to measure the properties of very forward neutral particles and the TOTEM [9] experiment has detectors either side of the CMS detector to measure the total proton-proton cross section.

In December 2009, the LHC became the highest energy particle collider in the world

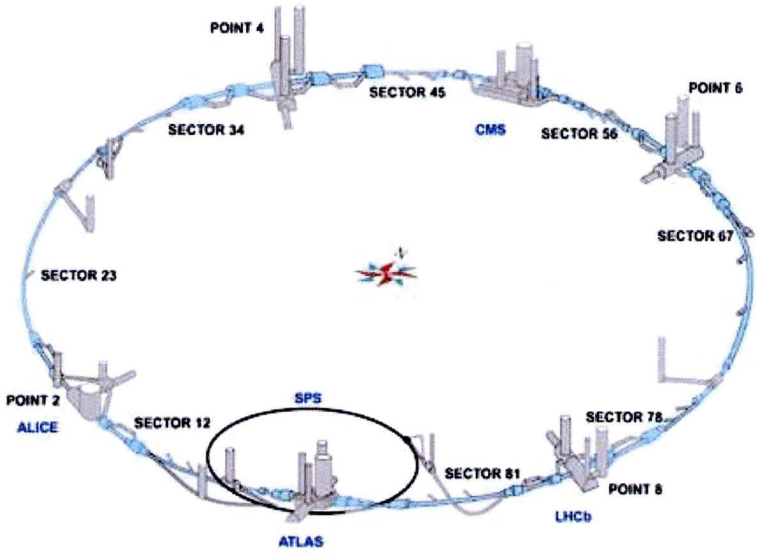

Figure 2.1: *A schematic view of the locations of the four major detectors at the LHC.*

when proton-proton collisions were recorded at a centre-of-mass energy of 2.36 TeV. Since then, both the beam energy and the beam intensity have been raised further, with the LHC currently colliding proton beams at a centre-of-mass energy of 7 TeV.

2.1 The ATLAS Experiment

The main objective of the ATLAS experiment is to search for new physics phenomena, both within and beyond the Standard Model. A major emphasis has been placed on the search for the Higgs boson and establishing the dynamics responsible for electroweak symmetry breaking. Beyond the SM, searches for new physics phenomena will include, amongst other things, searches for supersymmetric particles, new heavy gauge bosons ($W'$and Z') and extra dimensions. In addition, the ATLAS experiment will also perform precision measurements of SM parameters and processes and, in the collisions of heavy ions, investigate the properties of strongly interacting matter at extreme energy densities. The design of the ATLAS detector has therefore been guided by the need to be sensitive to a broad range of physics signatures. It consists of several independent detector systems, integrated into a central barrel section and two endcap sections. The detectors are positioned in consecutive layers, in an arrangement that is both forward-backward symmetric and near hermetic about the interaction point. A cut-away view of the ATLAS detector, indicating the positions of the different sub-detectors, is shown

in Figure 2.2. The sub-detector located closest to the interaction point is the inner detector (ID) [3, 10]. It is a tracking detector and provides measurements of primary and secondary vertices as well as measurements of the charge and momenta of charged particles. The electromagnetic (EM) calorimeter [3, 11] surrounds the inner detector. It provides energy deposition measurements and corresponding shower shape measurements for electrons, photons and the EM components of jets. Beyond the EM calorimeter, a series of hadronic calorimeters [3, 11, 12] provide similar measurements for strongly interacting particles. The outer dimensions of the ATLAS detector are defined by the muon spectrometer (MS) [3, 13], which is another tracking detector providing measurements of the charge and momenta of those charged particles (muons) that exit the calorimeters. In addition, an online trigger system identifies potentially interesting events and applies various selection criteria to determine which of these events should be recorded for offline analysis. However, the rate at which the event data can be written to CERN's data storage facility limits the rate at which events can be selected to ~200 Hz. The trigger system must therefore achieve a large rejection with respect to the 40 MHz bunch crossing frequency whilst maintaining sufficient selection efficiencies for rare processes. The first stage of this triggering process begins with the calorimeters and the muon spectrometer, where some preliminary selection criteria are applied in order to identify events with interesting physics signatures. The event data for the selected events are then passed off-detector, where additional criteria are then applied to reduce the event selection rate to an acceptable level. Further experimental difficulties arise from the fact that at nominal luminosity the expected inelastic proton-proton interaction rate is approximately 1 GHz, implying that every triggered bunch crossing will contain, on average, 23 events. This effect is referred to as event pile-up.

The performance requirements for each of the sub-detectors in terms of acceptance and measurement resolution, as set out in the ATLAS Technical Design Report (TDR) [4], are shown in Table 2.1. In addition to those listed in the table, the harsh experimental environment of the LHC has imposed further, stringent requirements on the speed, granularity and radiation hardness of the detectors' sensor elements and electronics.

The global ATLAS coordinate system is a right handed cartesian coordinate system in which the origin is defined to be the nominal interaction point. The beam axis defines

Detector Component	Required Resolution	η Coverage	
		Measurement	Trigger
Tracking	$\sigma_{p_T}/p_T = 0.05\%\ p_T \oplus 1\%$	± 2.5	–
EM Calorimetry	$\sigma_E/E = 10\%/\sqrt{E} \oplus 0.7\%$	± 3.2	± 2.5
Hadronic Calorimetry			
Barrel and Endcap	$\sigma_E/E = 50\%/\sqrt{E} \oplus 3\%$	± 3.2	± 3.2
Forward	$\sigma_E/E = 100\%/\sqrt{E} \oplus 10\%$	$3.1 < \lvert\eta\rvert < 4.9$	$3.1 < \lvert\eta\rvert < 4.9$
Muon Spectrometer	$\sigma_{p_T}/p_T = 10\%$	± 2.7	± 2.4

Table 2.1: *The general performance requirements of the ATLAS detector. The muon spectrometer performance is quoted for a muon with* $p_T = 1\ TeV$. *For high* p_T *muons the muon spectrometer performance is independent of the inner detector. The E and* p_T *are in units of GeV.*

the z axis, the positive x axis points towards the centre of the LHC and the positive y axis points directly upwards. The azimuthal angle (ϕ) is measured clockwise from the positive x axis in the range $[-\pi,\pi]$, the polar angle (θ) is measured from the positive z axis and the radial distance (r) from the interaction point is given by $r = \sqrt{x^2 + y^2}$. In addition, the pseudorapidity (η) is defined as $\eta = -\ln\tan(\theta/2)$, the transverse momentum (p_T) is defined in the $x - y$ plane and the distance in pseudorapidity-azimuthal angle space (ΔR) is defined as $\Delta R = \sqrt{\Delta\eta^2 + \Delta\phi^2}$.

2.2 The Inner Detector

The inner detector [3, 10], shown in Figure 2.3, spans the pseudorapidity range $|\eta| < 2.5$ and comprises three independent and complementary sub-systems: the pixel detector, the SemiConductor Tracker (SCT) and the Transition Radiation Tracker (TRT). The whole detector is positioned within a 2 T solenoid magnet to bend the paths of the charged particles traversing the detector. All three sub-systems measure the position

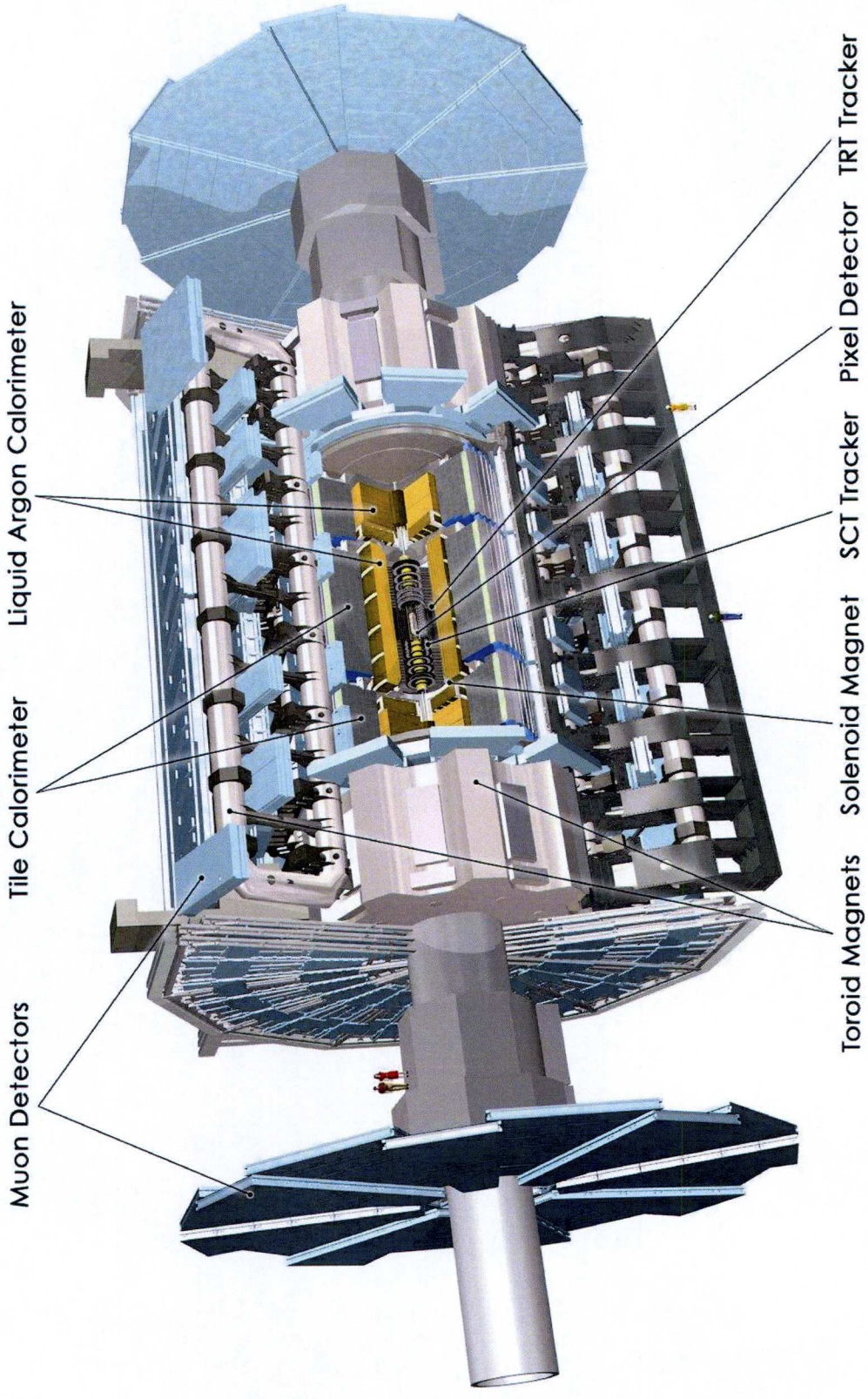

Figure 2.2: *A cut-away view of the ATLAS detector, indicating the positions of the different sub-detectors.*

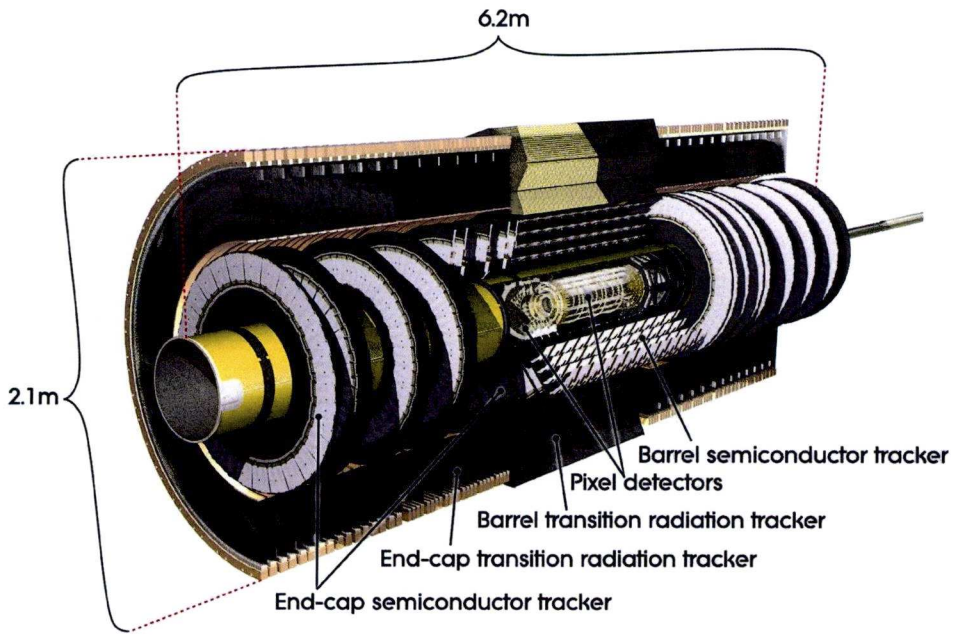

Figure 2.3: *A cut-away view of the inner detector, indicating the positions of the three different sub-detectors.*

coordinates of the charged particles as they traverse the detector. The pixel detector is positioned closest to the interaction point, followed by the SCT. They are both silicon-based detectors providing discrete, 3 dimensional space point measurements. The TRT occupies the outermost regions of the inner detector. It is a gaseous straw tube detector, providing continuous tracking measurements and aiding in particle identification.

The proximity of the inner detector to the interaction point means that its sensor elements and front end electronics will be subject to high levels of radiation. The pixel detector and the SCT have both been designed to withstand lifetime (10 year) 1 MeV neutron equivalent fluences[2] of 8×10^{14} cm^{-2} and 2×10^{14} cm^{-2}, respectively. The exception is the innermost barrel layer of the pixel detector, known as the B-layer, which lies only 5 cm away from the interaction point. This pixel layer will be subjected to even higher radiation levels and it is expected that it will need to be replaced after three years of operation at nominal luminosity. To maintain sufficient

[2]The 1 MeV neutron equivalent fluence is the fluence of 1 MeV neutrons believed to produce the same amount of radiation damage as that produced by a fluence of a given composition with a given energy spectrum.

long-term performance in the pixel detector and the SCT after irradiation, the silicon sensors are cooled to temperatures of approximately -5/-10°C. The TRT, in contrast, is intrinsically radiation hard and operates at room temperature.

For the inner detector to meet its peformance requirements and ensure that track parameter resolutions are kept below 20%, the positions of the sensor elements must be known to a precision of a few micrometers. This will be achieved through the application of track-based alignment procedures as well as an interferometer-based alignment monitoring system installed within the SCT [14]. Furthermore, an accurate map of the material distribution is also of crucial importance. The material causes multiple Coulomb scattering and leads to bremsstrahlung, photon conversion and secondaries from nuclear interactions, all of which affect the tracking performance. The amount of material present in the inner detector represents a compromise between a low material budget for optimal performance and a higher material budget due to structural features and services. To allow for an accurate description of the material distribution all detector elements were weighed prior to their installation such that the information could be incorporated into the ATLAS detector simulations. In addition, momentum measurements will also be affected by the uncertainty in the bending power of the solenoidal magnetic field. The aim is to determine the bending power of the magnetic field to a level that will limit the corresponding uncertainty on the track sagitta to 0.05%. Prior to the installation of the inner detector, a mobile array of Hall probes mapped the solenoidal magnetic field within the cavity. From the results of this field mapping, combined with simulation studies, the systematic error on the measurement of the track sagitta due to the magnetic field uncertainty was estimated to be in the range 0.02% to 0.12%, depending on the η coordinate of the charged particle [15]. Four nuclear magnetic resonance probles installed in the inner detector will continue to monitor the strength of the solenoidal magnetic field throughout the lifetime of the ATLAS experiment.

2.2.1 The Pixel Detector

The pixel detector is composed of silicon modules, arranged into three layers concentric with the beam axis in the barrel and three disks perpendicular to the beam axis in each of the endcaps. Each silicon module contains a silicon sensor segmented into 47232 pixels, 90% (10%) of which are of the dimensions, 50 μm in $r-\phi$ and 400 μm (600 μm)

in z (r for the disks). They provide measurements of the $r-\phi$ and z/r coordinates with resolutions at normal incidence of 12 μm and 66 μm, respectively. The pixel detector is therefore expected to provide at least three position measurements in $r-\phi$ and z/r for each charged particle within its acceptance. In total, there are 1744 silicon modules in the pixel detector, providing 80.4 million readout channels.

2.2.2 The Semiconductor Tracker

The SCT is composed of silicon modules, arranged into four layers concentric with the beam axis in the barrel and nine disks perpendicular to the beam axis in each of the endcaps. Each silicon module contains two pairs of silicon wafers segmented into strips with a mean pitch of 80 μm. The pairs are positioned back to back with a stereo angle of 40 mrad. Space points are then constructed from coincident hits on each side of the pair of silicon sensors. In the barrel modules the strips of the silicon sensors are aligned parrallel to the beam axis. In the endcap modules the strips of the silicon sensors extend radially around the beam axis. Each of the silicon modules provide measurements of the $r-\phi$ and z/r coordinates with resolutions at normal incidence of 17 μm and 580 μm, respectively. The SCT is therefore expected to provide at least four position measurements in $r-\phi$ and z/r for each charged particle within its acceptance. In total, there are 4088 silicon modules in the SCT detector, providing approximately 6.3 million readout channels.

2.2.3 The Transition Radiation Tracker

The TRT is composed of gas-filled straw tubes, arranged into three rings concentric with the beam axis in the barrel and two sets of wheels perpendicular to the beam axis in each of the endcaps. It spans the pseudorapidity range $|\eta| < 2.0$ and thus provides a slightly reduced coverage compared to the two silicon-based detectors. Each barrel ring and endcap wheel consists of layers of straw tubes interleaved with polymer fibres (barrel) or foils (endcaps). Ultra-relativistic charged particles (electrons) traversing the fibres/foils produce X-ray transition radiation which contributes significantly to the signal amplitude. The TRT therefore operates with two signal thresholds. A nominal (low) threshold for detecting minimally ionising particles and a high threshold for detecting the presence of additional transition radiation. The observation of high threshold hits allows for additional particle discrimination since the amount of tran-

sition radiation produced is directly proportional to a particle's relativistic γ factor. This is of particular importance in the separation of electrons/positrons and pions. The straws in the barrel rings are arranged parallel to the beam axis and the straws in the endcap wheels are arranged radially around the beam axis. Each straw tube provides a measurement of the $r - \phi$ coordinate with a resolution of 130 μm. Across most of its acceptance the TRT is expected to provide, on average, 36 position measurements in $r - \phi$ for each charged particle. The straw tubes provide a total of approximately 351,000 readout channels.

2.3 The Electromagnetic Calorimeter

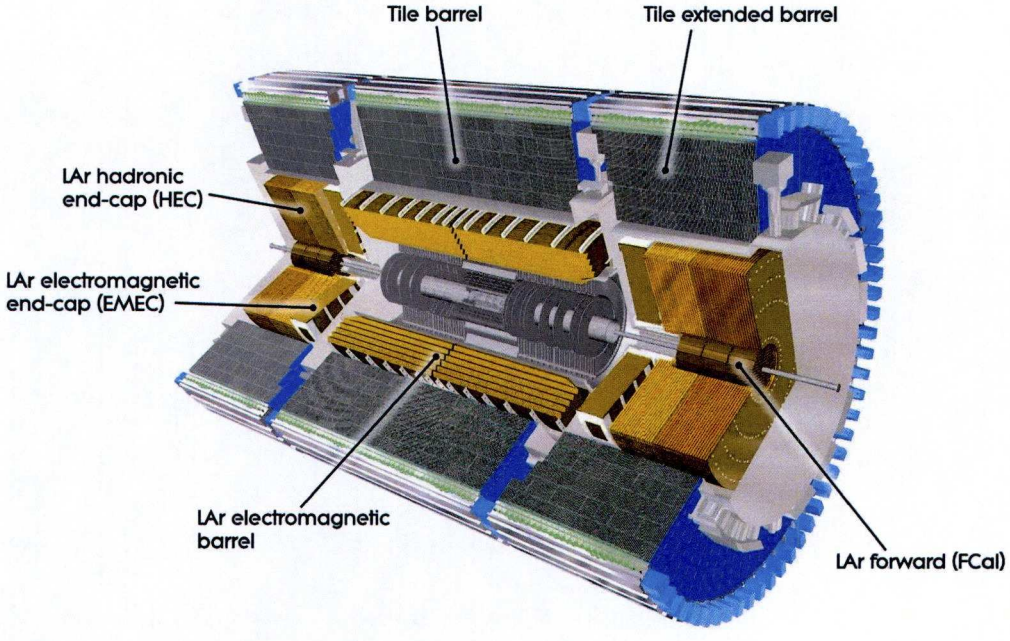

Figure 2.4: *A cut-away view of both the* EM *calorimeter and the hadronic calorimeters.*

The EM calorimeter [3, 11] is a lead/liquid argon (LAr) sampling calorimeter, spanning the pseudorapidity range $|\eta| < 3.2$. It is composed of a barrel section and two endcap sections, providing full coverage around the beam axis and full ϕ symmetry without discontinuity. The barrel section covers the pseudorapidity range $|\eta| < 1.475$ and consists of two identical half barrels separated by a small gap at $z = 0$. The endcap sections each consist of a pair of coaxial, inner and outer wheels, covering pseudorapid-

ity ranges of $2.5 < |\eta| < 3.2$ and $1.375 < |\eta| < 2.5$, respectively.

Each section of the EM calorimeter is instrumented with accordion-shaped layers of lead absorbers and copper-kapton readout electrodes (Figure 2.5). The readout electrodes and the LAr active medium occupy the spaces in-between successive absorber layers. The accordion geometry allows the EM calorimeter to achieve full azimuthal coverage with no crack regions. In the barrel section, the accordion shaped absorbers run parallel to the beam axis and are stacked along the ϕ direction. In the endcaps, the accordion waves are parallel to the radial direction and are stacked in $r - \phi$. The folding angles of the accordion waves and the thickness of the absorber plates are varied throughout the EM calorimeter to provide optimal/uniform performance in terms of linearity and energy resolution.

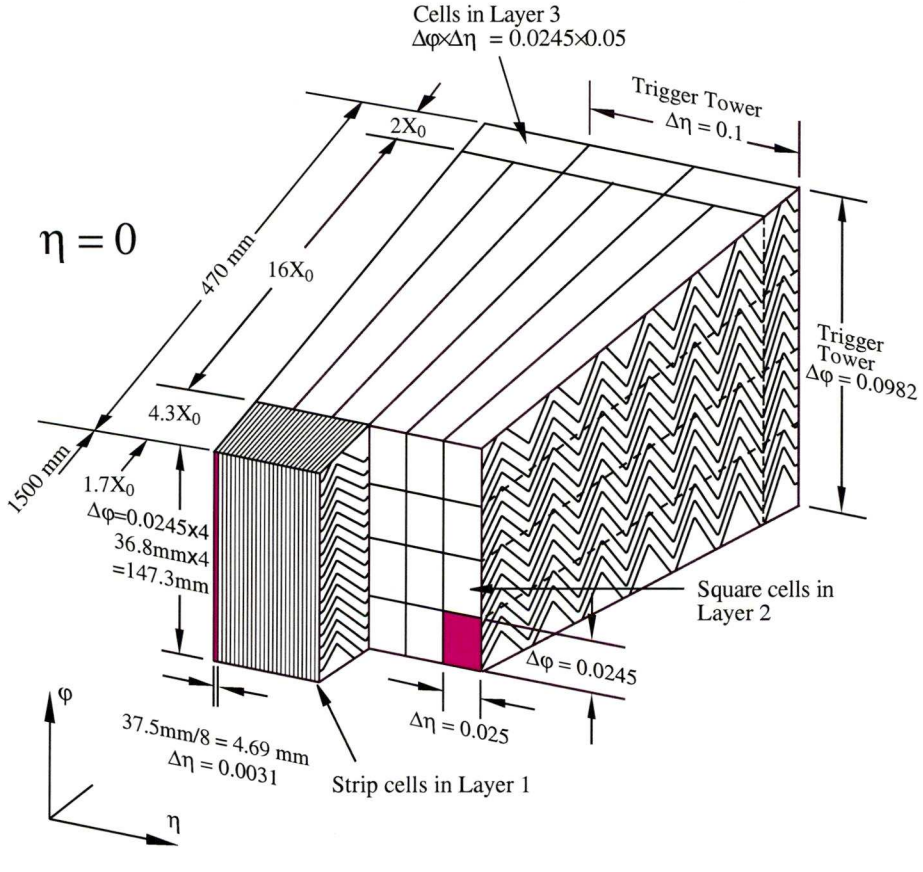

Figure 2.5: *A schematic view of part of the barrel section of the* EM *calorimeter, indicating the accordion structure and the granularity of the different layers.*

Across most of the pseudorapidity range $|\eta| < 2.5$, (corresponding to the inner detector acceptance), the EM calorimeter is segmented into three layers to allow mea-

surements of shower evolution as a function of depth. The innermost layer is finely segmented into strips in the η direction. These strips provide a measurement of the η coordinate of an EM shower. The middle layer is segmented into square cells. This is the thickest of the three layers and absorbs the largest fraction of the energy in an EM shower. The outermost layer is segmented into towers and provides estimates of possible energy leakage from the back of the EM calorimeter. This third and final layer only collects the tail of an EM shower and therefore has a coarser granularity than the previous two layers. Those areas within the pseudorapidity range $|\eta| < 2.5$, that are not segmented into three layers, are the outermost region of the barrel ($1.35 < |\eta| < 1.475$) and the outermost region of the endcaps ($1.375 < |\eta| < 1.5$). In these areas and in the pseudorapidity range $2.5 < |\eta| < 3.2$, the EM calorimeter is segmented into only two layers of a more coarse granularity. Across the whole EM calorimeter, the layers provide cumulative depths of > 22 radiation lengths (X_0) in the barrel and > 24 X_0 in the endcaps, which is expected to be sufficient to contain EM showers.

In the pseudorapidity range $|\eta| < 1.8$, a fourth LAr layer is installed in front of the EM calorimeter to provide shower sampling measurements. This additional presampler layer allows for corrections to be made for energy losses in the material upstream of the calorimeters.

2.4 The Hadronic Calorimeters

Hadronic calorimetry is provided by three independent calorimeters, collectively spanning the pseudorapidity range $\eta < 4.9$. Each calorimeter employs a different technology to satisfy the performance requirements in different regions of the ATLAS detector. As in the case of the EM calorimeter, the hadronic calorimeters are of a sampling design and provide full coverage around the beam axis and full ϕ symmetry without discontinuity. A scintillating tile calorimeter, (TileCal) [3, 12], is positioned directly outside the EM calorimeter envelope and provides the hadronic calorimeter coverage in the range $|\eta| < 1.7$. The TileCal consists of a barrel section covering the pseudorapidity range $|\eta| < 1.0$ and two extended barrel sections which extend the coverage to $|\eta| < 1.7$. All three sections are segmented into three layers. Within each layer, scintillating tiles provide the active medium whilst steel plates act as both absorber and return yoke for the solenoidal magnetic field of the inner detector. A schematic view of part of the

tile calorimeter is shown in Figure 2.6. The tiles are arranged radially and normal to the beam axis and achieve almost seamless azimuthal coverage. Wavelength shifting readout fibres on the scintillator tile edges are grouped together into readout photomultiplier tubes which have an approximately projective geometry in pseudorapidity. The gap regions between the barrel and the extended barrel sections are instrumented with steel-scintillator sandwiches and scintillator counters. These provide additional coverage to partially recover some of the energy that would otherwise be lost in these crack regions.

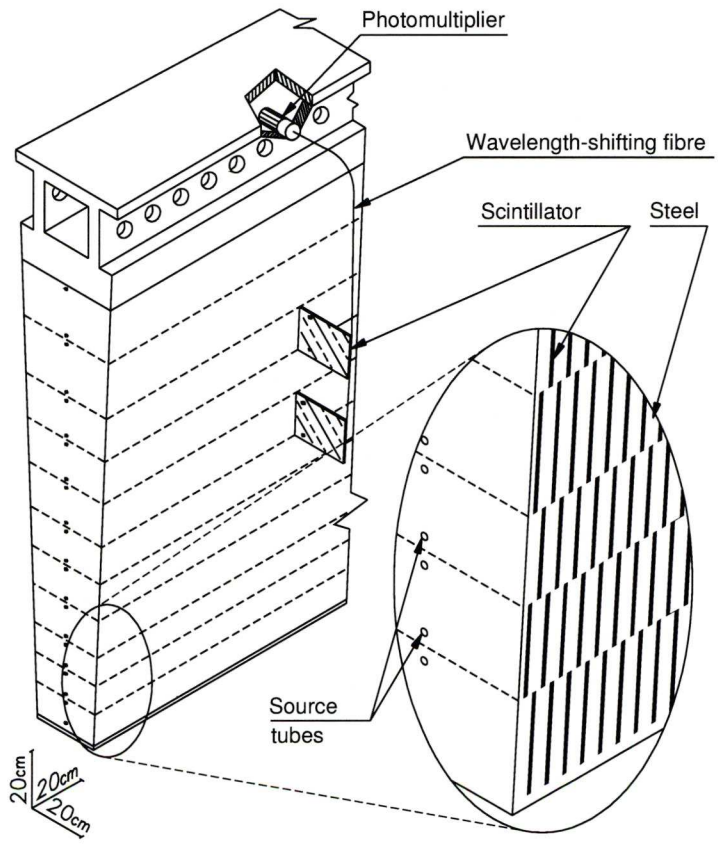

Figure 2.6: *A schematic view of part of the Tile Calorimeter, indicating the tiles, fibres and photomultipliers of the optical readout.*

Two additional LAr calorimeters, the Hadronic Endcap Calorimeter [3, 11] (HEC) and the Forward Calorimeter [3, 11] (FCal) are positioned directly behind the EM calorimeter endcap sections and further extend the hadronic calorimeter coverage to the pseudorapidity ranges $1.5 < |\eta| < 3.2$ and $3.1 < |\eta| < 4.9$, respectively. The HEC consists of two wheels of copper absorber plates interleaved with the LAr active medium.

The wheels are themselves segmented into 2 layers, providing a total of four calorimeter layers in each endcap. The FCal provides the hadronic calorimetry in the most forward regions of the detector. It is of a high density design and consists of three separate longitudinal sections in each of the endcaps. The innermost section is made of copper and provides extended EM calorimeter coverage. The middle and the outer sections are made of tungsten and complete the hadronic calorimeter coverage. In addition to providing measurements of both EM and hadronic interactions, the FCal also reduces background radiation levels in the muon spectrometer. The full depth of the hadronic calorimeters is $\sim$10 interaction lengths (λ), which has been shown to be sufficient to contain hadronic showers and limit punch through into the muon spectrometer.

2.5 The Muon Spectrometer

The muon spectrometer, shown in Figure 2.7, spans the pseudorapidity range $|\eta| < 2.7$ and is instrumented with both precision tracking chambers and trigger chambers. The chambers are arranged in three layers concentric with the beam axis in the barrel and three wheels perpendicular to the beam axis in each of the endcaps. The layers and wheels, both referred to as stations, are segmented in the $r - \phi$ plane forming eight small and eight large (alternating) projective sectors.

Three superconducting, air-core, toroid magnets provide the magnetic field to bend the paths of the charged particles traversing the muon spectrometer. Each of the toroid magnets consist of eight coils arranged radially and symmetrically around the beam axis. One of the toroid magnets occupies the barrel; this is the largest of the three. The other two smaller, endcap toroid magnets are inserted into each end of the large, barrel toroid magnet. The resulting toroidal magnetic field, of 0.5 T in the barrel and 1.0 T in the endcaps, is mostly perpendicular to the trajectories of the particles exiting the calorimeters.

The precision tracking chambers measure the position coordinates of the charged particles at each station. For most of the muon spectrometer's coverage the precision tracking chambers are Monitored Drift Tube (MDT) chambers. Each (regular) MDT chamber comprises a pair of drift tube multilayers, separated by a mechanical spacer. In the innermost stations, the multilayers consist of four monolayers; in the middle and outer stations they consist of three monolayers. For those detector regions with MDT

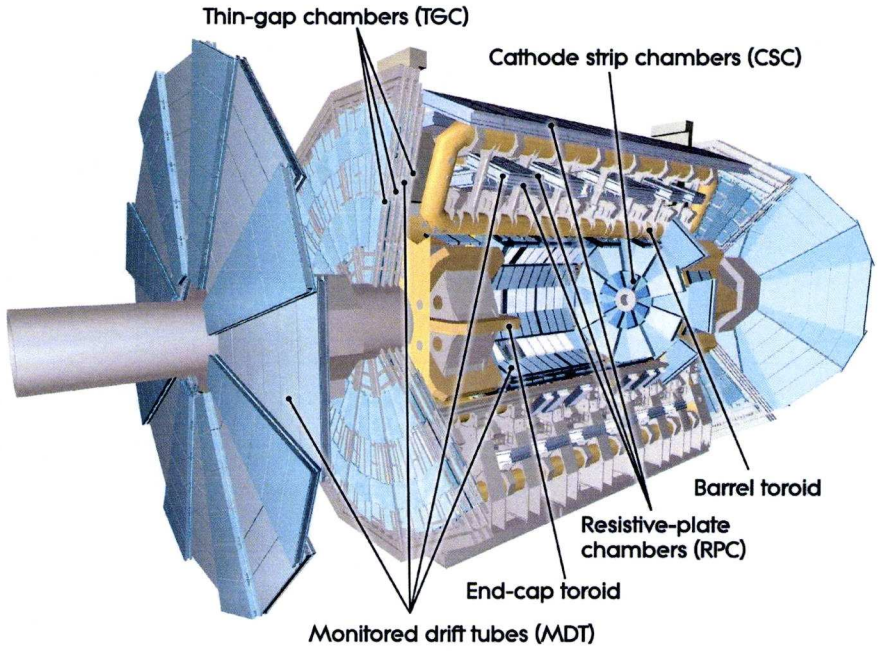

Figure 2.7: *A cut-away view of the ATLAS detector, indicating the positions of the precision tracking chambers and the trigger chambers of the muon spectrometer.*

coverage, 20 drift tube measurements are therefore expected for each charged particle track. The MDTs provide measurements of track position in z/r with resolutions of $\sim$80 μm per drift tube, or $\sim$35 μm per MDT. In total, there are 1150 MDT chambers in the muon spectrometer, providing 354,000 readout channels.

In the most forward regions ($2 < |\eta| < 2.7$) of the inner endcap stations the precision tracking chambers are Cathode Strip Chambers (CSCs). These are multiwire proportional chambers with two cathode planes oriented perpendicularly with respect to each other. They have greater granularity and higher rate capabilities than the MDTs, which makes them better suited for operation in these forward areas of the detector. In each of the endcaps, there are two adjoining disks of eight small CSCs and eight large CSCs, respectively, arranged in accordance with the $r-\phi$ segmentation of the muon spectrometer. Each CSC consists of four anode wire planes in which the wires extend radially around the beam axis, surrounded by cathode strip planes. The cathode strips that are perpendicular to the anode wires provide a measurement of the r coordinate with a resolution of 40 μm. The cathode strips that are parallel to the anode wires provide a measurement of the ϕ coordinate with a resolution of 5 mm. The CSCs are thus expected to provide four position measurements in r and ϕ for each

charged particle that traverses one of the CSC disks. In total, the 32 CSCs in the muon spectrometer provide 30,700 readout channels. The trigger chambers in the muon spectrometer cover the pseudorapidity range $|\eta| < 2.4$, corresponding approximately to the acceptance of the inner detector. In addition to contributing to the trigger decision, the trigger chambers also provide measurements of the position coordinate of charged particles in the non-bending plane, to complement the precision measurements of the position coordinate in the bending plane.

The trigger chambers in the barrel are Resistive Plate Chambers (RPCs). They are located on both sides of the middle station and on the inside (outside) of the outer station of the small (large) $r-\phi$ sectors. Each RPC comprises two contiguous detector units. Each detector unit is itself composed of two independent parallel electrode-plate detectors that are read out by orthogonal layers of pickup strips. The pickup strips that are parallel to the MDTs provide a measurement of the z coordinate. The pickup strips that are orthogonal to the MDTs provide a measurement of the ϕ coordinate. The measurements of both coordinates are made with space and time resolutions of 1 cm and 1 ns, respectively. The RPCs are therefore expected to provide 6 measurements for each charged particle that traverses the middle and outer barrel stations. In total, there are 606 RPCs in the muon spectrometer, providing 373,000 readout channels.

The trigger chambers in the endcaps are thin gap chambers (TGCs), which operate on the same principle as multiwire chambers. The chambers are grouped into either doublets or triplets to form TGC units. In each of the endcaps, there are four wheels of TGC units perpendicular to the beam axis: one wheel of doublets and three wheels of triplets. The doublet is positioned in front of the inner station, one of the triplets is positioned in front of the middle station and the remaining two triplets are positioned behind the middle station. Within each TGC unit, the anode wires are arranged parallel to the MDT wires and provide measurements of the r coordinate with space and time resolutions of $2-3$ mm and 4 ns, respectively. A set of readout strips orthogonal to the anode wires provide measurements of the ϕ coordinate with space and time resolutions of $3-7$ mm and 4 ns, respectively. The TGCs are therefore expected to provide 9 measurements for each charged particle track that passes through all four TGC wheels. In total there are 3588 TGCs in the muon spectrometer, providing 318,000 readout channels.

The precision tracking chambers, the trigger chambers and the front-end electronics

have all been designed to tolerate the radiation levels expected to be present in the muon spectrometer. For most of the muon spectrometer, the ionising radiation dose is expected to be less than 1 Gy/y; however, for the CSCs the dose is expected to be as high as 20 Gy/y. The effects of the background radiation on track finding efficiencies and (fake) trigger rates are expected to be more significant than the effects of radiation damage. Nevertheless, all components have been tested to withstand at least five times the radiation levels predicted by simulations.

The driving performance goal of the muon spectrometer is a standalone p_{T} resolution of approximately 10% for 1 TeV muons; this corresponds to a sagitta of $\sim$500 μm, measured with a precision of < 50 μm. In order to achieve this kind of resolution, the locations of the MDTs and the CSCs must be known to a precision of ≤ 30 μm. The positions and the internal deformations of the MDTs are therefore monitored by both an optical alignment system and a number of complementary track-based alignment procedures. In addition, the extraction of the momentum from the precision tracking measurements requires a precise knowledge of the toroidal magnetic field. The aim is to ensure that the uncertainty in the bending power of the magnetic field does not degrade the momentum resolution by more than $\sim$3%, anywhere in the muon spectrometer. A full mapping of the toroidal magnetic field, like that performed for the solenoidal magnetic field, was unfeasible; however, approximately 1800 Hall sensors have been mounted onto the MDTs and the two endcap cryostats to monitor the toroidal magnetic field during operation. Two nuclear magnetic resonance probes have also been positioned in the barrel to detect any long-term drift in the response of the Hall sensors.

2.6 The Trigger

The ATLAS trigger consists of three consecutive levels of online event selection: the Level-1 (L1) trigger, the Level-2 (L2) trigger and the event filter (EF). The L2 trigger and the EF are often referred to collectively as the high-level trigger (HLT). Each of the three trigger levels provide an increasingly refined event selection procedure.

The L1 trigger performs the first step in the event selection chain, reducing the event rate from 40 MHz to 75 kHz (upgradable to 100 kHz). It identifies potentially interesting events using reduced granularity information from fast, custom build hardware in the calorimeters and the muon spectrometer. In the calorimeters, the L1 trigger

searches for energy deposits summed in towers of (mostly) $\Delta\eta \times \Delta\phi = 0.1 \times 0.1$ and determines whether they are characteristic of electrons/photons, jets, hadronically decaying τ leptons, as well as identifying global signatures, such as large $\sum E_{\mathrm{T}}$ and large $\not{E}_{\mathrm{T}}$. In the muon spectrometer the L1 trigger searches for hit coincidences in the trigger chambers of different stations. A system of programmable hit coincidence logic allows for a coarse, preliminary determination of the p_{T} of each muon candidate. For each bunch crossing, the global signatures and the multiplicities of the identified trigger objects at different E_{T} and p_{T} thresholds are cross referenced against a trigger menu[3] of desirable signatures. The L1 trigger then selects those events that can satisfy one (or more) of the items listed in the trigger menu. In order to identify unambiguously each of the bunch crossings, the L1 trigger latency, defined as the time between the bunch-crossing and the delivery of the corresponding L1 trigger decision, must be less than 2.5 μs. In addition to the L1 trigger decision, for each event, the L1 trigger also identifies regions of interest (RoIs) in the detector. These RoIs are defined by the η and ϕ coordinates of the objects identified in the event, with each one representing about 2% of the full detector data. Upon an event being selected by the L1 trigger, information relating to each of the RoIs is made available to the HLT where further, software-based selection processes are implemented.

The L2 trigger further reduces the event rate to below 3.5 kHz, with an average event processing time of 40 ms. At this level (and the next), all of the detector data can be accessed at full granularity and full precision. To avoid unnecessary data transfers, the event selection is seeded by the RoIs identified at the L1 trigger. The selection process is then performed in a series of steps as more data are introduced from the different detectors. In particular, information from the inner detector is now available which allows for improved particle identification and, specifically, the separation of electrons and photons. Feature extraction algorithms attempt to identify objects such as tracks and calorimeter clusters within the data. Any identified objects are then scrutinised by hypothesis algorithms to determine whether or not they meet the criteria required to satisfy a given signature. If an event is selected by the L2 trigger, the event information

[3]Trigger menus are implemented at each of the three trigger levels. They each contain a list of items that specify trigger object multiplicities and/or global signatures with specific thresholds, that can be combined either in coincidence or in veto. The trigger menus are flexible and are designed to address physics analysis requirements.

from the full detector is assembled into a single data structure, in a process known as event building. The entire event is then passed to the Event Filter (EF) for further processing.

The EF performs the final step in the event selection chain, reducing the event rate to ~200 Hz, (corresponding to ~300 Mbyte s^{-1}). The most complex selection criteria are applied at this level, with an average event processing time of 4 s. The event selection process is steered in the same way as at L2, except that the algorithms involved are now based on the standard offline reconstruction and analysis algorithms, having been adapted for operation in the online environment. The events that pass all three trigger levels are categorised into inclusive physics or trigger streams before being written to permanent storage. A subset of the selected events are also written to calibration streams and express streams for fast detector calibration and monitoring, respectively.

Chapter 3

The Annealing of SCT Silicon Microstrip Sensors

In the harsh experimental environment of the LHCthe inner detector will be subjected to extreme levels of radiation. The dominant source of this radiation will be the proton-proton collisions at the interaction point, with additional contributions coming from beam halo particles and beam gas interactions. Exposure to such high levels of radiation can cause significant damage to the silicon sensors (and front-end electronics) and subsequently alter their electrical properties. Since access to the SCT will be limited, it is important to ensure that the radiation induced changes in sensor peformance are tolerable so that the detector components can operate stably and reliably throughout the lifetime of the ATLAS detector. In the ATLAS TDR [4] a series of predictions were made to determine the expected performance of the SCT silicon sensors over the full 10 year lifetime of the ATLAS experiment. These predictions were based on a number of assumptions with regards to the operational scenario of the LHC and the ATLAS detector which have since changed and, as such, the predictions were revised [16]. In addition, an alternative radiation damage parameterisations has since been developed which shows significant variation with respect to the parameterisation that was used in the TDR predictions. Further experimental data corresponding to high doses and long annealing times were therefore required to determine which of the two radiation damage parameterisations provides the best description, in order to be able to make accurate predictions for the long-term SCT sensor performance using the most up-to-date operational information.

3.1 The SCT Silicon Microstrip Sensors

Silicon sensors are integral to most modern high energy physics experiments as their excellent performance in terms of spatial resolution, rate capability and radiation hardness make them ideal for use in tracking and vertexing detectors.

The silicon sensors in the SCT are single sided microstrip sensors consisting of p-type strips on high resistivity n-type bulk. 92.2% [17] of the silicon sensors were manufactured by Hamamatsu Photonics [18], whilst the remaining 7.8% [17] were manufactured by CiS [19]. All strips on the silicon sensors are AC coupled to six 128-channel ABCD3TA readout chips [20], providing 768 (1536) readout channels per sensor (module). The nominal signal threshold required to generate a hit in the sensor is 1 fC [17].

The operation of the silicon sensors is based on the properties of the p-n junction. At the junction between the p-type doped silicon and the n-type doped silicon the electrons (holes) diffuse from the n-type (p-type) side and recombine with holes (electrons) on the p-type (n-type) side. The diffusion of the electrons (holes) leaves behind ionised donor (acceptor) atoms and an electric field develops across the junction which inhibits further diffusion until equilibrium is reached. The space charge region formed around the junction is now devoid of mobile charge carriers and is referred to as the depletion region. The potential difference that now exists between the p-type and n-type sides of the junction is known as the built in voltage V_{bi}. Applying an external reverse bias (V) to the p-n junction draws electrons (holes) away from the n-type (p-type) side and increases both the depletion region width (ω_d) and the electric field across the junction. The maximum bias voltage applicable to the sensors is limited by the high voltage power supply to approximately 450 V. The relationship between the reverse bias voltage and the width of the depletion region is given by [21],

$$\omega_d = \sqrt{\frac{2\epsilon(V_{bi} + V)}{Ne}} \tag{3.1}$$

where ϵ is the dielectric constant of the silicon, N is the dopant concentration in the bulk of the sensor and e is the magnitude of the electron charge. The built in potential V_{bi} can ususally be neglected since it typically has a value of only 0.5 V in detector diodes. When the depletion width is less than the thickness of the sensor (d), the sensor is described as being partially depleted. Alternatively, when the depletion region spans the full thickness of the sensor, the sensor is described as being fully depleted. The

reverse bias voltage required to fully deplete the silicon sensor is referred to as the depletion voltage (V_{dep}) and is given by [21],

$$V_{dep} = \frac{Ned^2}{2\epsilon} \tag{3.2}$$

The thickness of the silicon sensors in the SCT is 285 μm. This value was chosen as a compromise between thinner sensors which have lower operating voltages and thicker sensors which have larger signal to noise ratios (S/N). The thickness also had to adhere to the strict material budget of the SCT and, at 285 μm, represents 0.16% of a radiation length to particles at normal incidence.

Ionising particles traversing the sensor create electron-hole pairs in the depletion region, which are swept to the electrodes by the electric field and induce an electrical current in the external circuitry. In this manner, the silicon sensor essentially behaves like a solid state ionisation chamber. In silicon microstrip sensors, like those in the SCT, one (or both) of the electrodes are segmented in order to provide position measurements. The silicon microstrip sensors in the SCT are p-in-n sensors, and the sensor readout is at the side of the segmented p-type strips. A schematic cross sectional view of a silicon microstrip sensor of the SCT, indicating the main features of the sensor and the nature of the charge collection, is shown in Figure 3.1

Since the depletion region is devoid of mobile charge carriers it behaves as an insulator, bounded by the conducting p-type and n-type silicon layers above and below. Consequently, the silicon sensor can be considered to behave approximately as a parallel plate capacitor, with capacitance given by [21],

$$C = \epsilon \frac{A}{\omega_d} = A\sqrt{\frac{\epsilon e N}{2V}}. \tag{3.3}$$

The capacitance of the silicon sensor decreases as the applied bias voltages increases, until full depletion is reached at which point the capacitance remains constant. The full depletion voltage of the sensor can therefore be determined by identifying the applied bias voltage at which the capacitance of the sensor reaches saturation.

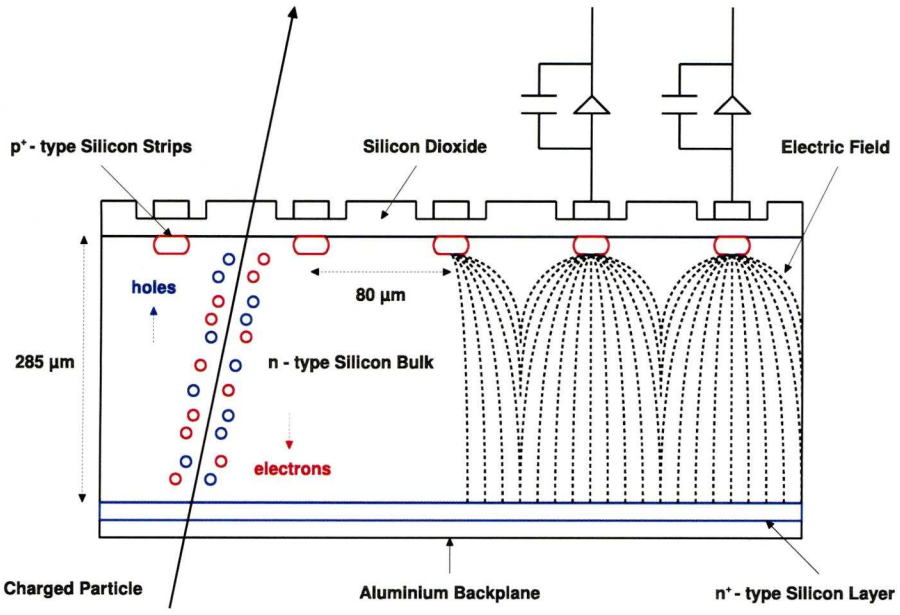

Figure 3.1: *A schematic cross sectional view of a silicon microstrip sensor of the SCT in operation.*

3.2 Radiation Damage in Silicon Sensors

Radiation damage in silicon sensors occurs via two mechanisms: ionisation damage and displacement damage. Ionising radiation passing through a silicon sensor, ionises the atoms and produces a number of electron-hole pairs, many of which will quickly recombine. Under the influence of an applied bias voltage, some of the electron-hole pairs will be swept towards the positive and negative electrodes respectively. In the bulk, charge flows through the external circuitry to restore equilibrium and thus the ionisation does not lead to any lasting damage. However, in the silicon oxide layer at the surface of the silicon sensor, the holes drift towards their respective electrode with a lower mobility than that of the electrons and hence can become trapped in the oxide layer. Holes reaching the interface between the silicon oxide layer and the silicon bulk may recombine with electrons from the bulk or become trapped by impurities or defects at the lattice boundary, leading to the accumulation of unintended charge concentrations and subsequent parasitic electric fields. Such fields can lead to an increase in the required bias voltage and the charge build up can form conducting channels between the strips, leading to a degradation in resolution. These so-called surface effects are relatively small and are therefore considered to be less significant that the effects of

displacement damage. Furthermore, the damage introduced by the ionising radiation can be identified relatively quickly such that appropriate modifications to the sensor design can be made before the detector is built. A more limiting factor in the sensor performance is the radiation induced displacement damage in the bulk of the sensor. Since the characteristics of sensor depletion regions depend primarily on the bulk properties of the sensor, lattice defects in the bulk can have a significant impact on the sensor performance, while displacement in the silicon surface can usually be neglected.

3.2.1 Displacement Damage

Displacement damage occurs when the radiation incident on a silicon sensor has sufficient energy to knock a silicon atom from its lattice site. The displaced atom is known as a Primary Knock on Atom (PKA) and, together with the resulting lattice vacancy, forms what is referred to as a Frenkel pair. After the initial displacement, the PKA may quickly recombine with the vacancy leaving no lasting damage, or depending upon its recoil energy, the PKA may continue to impart further damage to the lattice. For the lower recoil energies (ie. just above the displacement threshold), the PKA may simply form a point defect in the lattice. For higher recoil energies the PKA may continue to move through the lattice depositing its energy by the ionisation and displacement of further silicon atoms. As mentioned, the ionisation of silicon atoms in the bulk does not result in any long-term damage to the lattice but as the PKA continues to lose energy, the displacement of further silicon atoms becomes the more dominant energy loss mechanism and a cascade of further PKAs develops. As a result, a dense agglomeration of lattice defects, known as a defect cluster, is formed at the end of the PKAs track through the silicon, as shown in Figure 3.2. Following the formation of these initial lattice defects, the resulting lattice vacancies and interstitial silicon atoms can migrate through the lattice combining with each other, or with the dopants and impurities present in the lattice, to form more complex defects with a variety of electrical characteristics. The time evolution of the radiation induced defects is known as annealing and is strongly dependent upon the temperature of the silicon sensor. The annealing of the silicon is effectively suppressed below 0 °C; however, above this temperature, annealing will continue even after irradiation has ceased. Since the defects themselves originate from Non-ionising Energy Loss (NIEL) in which energy and momentum are transferred to the lattice atoms, the initial damage induced is specific to a

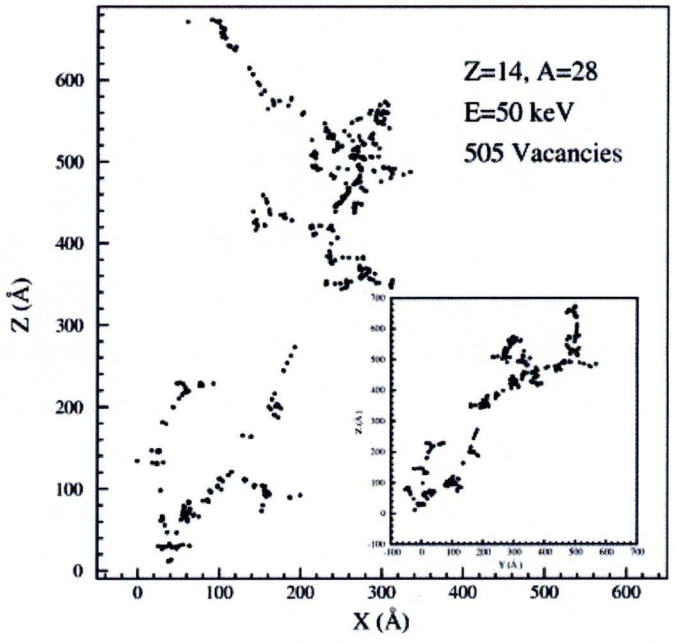

Figure 3.2: *A simulation of the subsequent displacement damage caused by a displaced silicon atom with a recoil energy of 50* keV*, which is the average recoil energy produced by 1* MeV *neutrons [22]. The point defects and the dense cluster defects can clearly be distinguished. The insert shows the transverse projection.*

particular incident particle with a given energy. However, by assuming that the degree of induced displacement damage is proportional to the NIEL of the incident radiation, comparisons can be made between the relative effects of different incident particles with different energy spectra.

3.2.2 The NIEL Scaling Hypothesis

The assumption that the radiation induced displacement damage in the bulk is proportional to the Non-Ionising Energy Loss (NIEL) of the incident radiation is the basis of the NIEL scaling hypothesis, which allows for comparisons to be made between the relative effects of different radiation environments[4].

For an incident particle with an energy E, a displacement damage cross section $D(E)$ can be defined as an equivalent expression of the NIEL value.

[4]There is some experimental evidence to suggest that there are some limitations in the application of the NIEL scaling hypothesis [23]. Nevertheless, it is generally applied as a first order approximation.

$$D(E) = \sum_i \sigma_i(E) \int f_i(E, E_R)\ P(E_R)\ dE_R. \tag{3.4}$$

The sum is performed over all possible interactions between the incident particle and the lattice. The function f_i describes the probability that the incident particle with energy E produces a PKA with a recoil energy E_R through the interaction i with a cross section σ_i. The Lindhard partition function, $P(E_R)$, describes the proportion of the PKA recoil energy that is deposited in the displacement of lattice atoms. The displacement damage cross section is typically quoted in units of MeV mb, indicating that each interaction has a particular cross section and contributes a certain amount of energy to the displaced lattice atom. The energy transferred to the displaced lattice atoms can therefore be determined by multiplying the displacement damage cross section by the incident fluence and the number of irradiated lattice atoms.

From the displacement damage cross sections, a hardness factor κ is defined to describe the relative damage efficiencies of different incident particles with given energy spectra $\phi(E)$, with the standard value of 95 MeV mb [24] for the displacement damage cross section of 1 MeV neutrons most commonly used as the reference. This is shown in Figure 3.3.

$$\kappa = \frac{\int D(E)\ \phi(E)\ dE}{D(1\ MeV)\ \int \phi(E)\ d(E)} \tag{3.5}$$

Subsequently, the radiation damage resulting from an arbitrary particle beam with an energy spectrum $\phi(E)$ and a fluence Φ can be related to an equivalent fluence Φ_{eq} of 1 MeV neutrons that would result in the same degree of radiation damage.

$$\Phi_{eq} = \kappa\ \Phi \tag{3.6}$$

Normalising particle fluences in this manner allows for direct comparisons to be made between the effects of different radiation fields, by describing the damage that they induce in terms of a common quantity.

3.3 The Effects of Radiation Damage in Silicon Sensors

The lattice defects from radiation induced displacement damage can behave as both donors and acceptors and lead to the development of additional energy levels in the

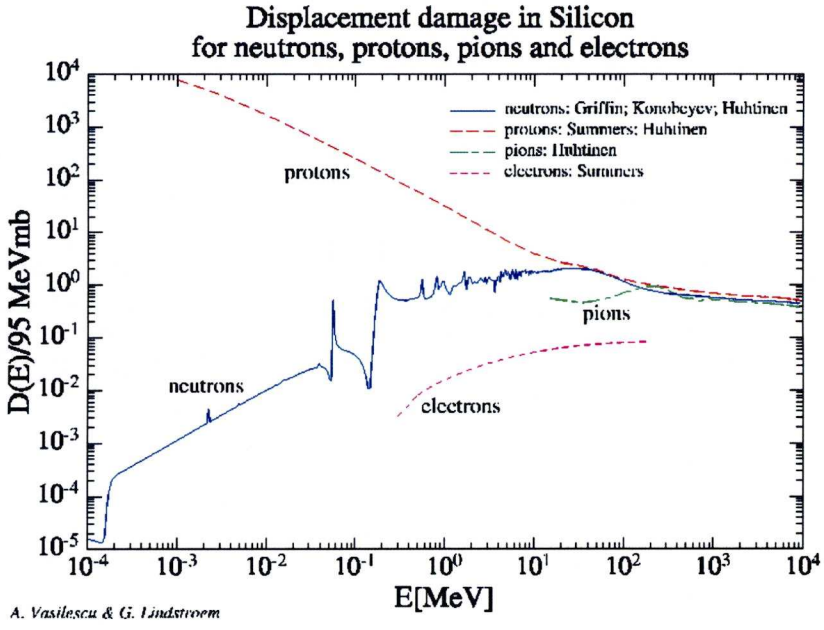

Figure 3.3: *The displacement damage cross sections for different particles incident on silicon, relative to the displacement damage cross section for 1* MeV *neutrons [25]. Although not all of the data has been verified experimentally, the curves can still be used to estimate relative effects.*

silicon band gap. These changes to the silicon band structure can result in changes to the silicon sensors macroscopic electrical properties. The probabilities for transitions between the energy levels are exponential functions of the energy difference between the levels and so the introduction of deep mid-gap states can facilitate transitions that would otherwise be highly improbable, by acting as intermediate, stepping-stone states. In a depletion region (under reverse bias), the conduction band is under populated and so electrons are promoted from the valence band to the conduction band resulting in a reverse bias or leakage current. The most significant worry about the leakage current in silicon sensors is that it shows a strong temperature dependence and if the operational temperature is not sufficienctly low, it is possibile that an increase in the operational temperature may lead to an increase in leakage current and subsequent thermal runaway through self-heating of the silicon sensor. In addition, if the leakage current exceeds the point of stable operation the sensor can be permanently damaged. However, low temperature operation can suppress these leakage currents and after the initial defect formation the leakage current decreases with annealing time. In addition to the leakage current, the charge collection efficiency is also an important factor in

determining whether or not a silicon sensors can still maintain an adequate S/N after irradiation and annealing. The trapping of signal charge by radiation induced trapping centres and radiation induced changes to the effective doping concentration both have an impact on the charge collection efficiency.

3.3.1 Signal Charge Trapping

Radiation damage to the bulk of the silicon sensor can introduce defect states close to the band edges in the band gap. These shallow defect states can trap charge as it traverses the depletion region. Since holes are less mobile than electrons they have a greater collection time and, as such, are more sensitive to trapping effects and recombination. Trapped charge is retained for a certain time before it is released again and if this trapping time is longer than the shaping time of the electronic readout, the measured signal charge will be reduced. However, the introduction of trapping centres is not generally considered to be one of the main limiting factors in the sensor performance since the effects of trapping may often be overcome by an increase in the bias voltage.

3.3.2 Effective Doping Concentration

Radiation induced changes to the effective doping concentration have a more significant effect on the performance of the silicon sensors. Prior to irradiation, the depletion region of the silicon sensor exhibits a space charge originating from the ionised dopant host atoms. For the p-in-n silicon microstrip sensors of the SCT, this is a positive space charge. The reverse bias voltage applied to the sensor is required not only to create a region devoid of charge carriers but also to collect mobile charges against the electric field of the space charge. Experimental observations suggest that the radiation induced lattice defects behave as acceptor like states which, through thermal excitation, are populated by electrons from the silicon bulk leading to the creation of a negative space charge. With increasing fluence, the initial positive space charge of the ionised donor atoms is neutralised by the increasing negative space charge from the occupied, radiation induced acceptor defects. At some point, the positive and negative space charges cancel and the net space charge becomes zero. Beyond this fluence, type inversion occurs and the depletion region which was initially n-type now appears p-type. However, since the radiation induced lattice defects do not lead to the creation

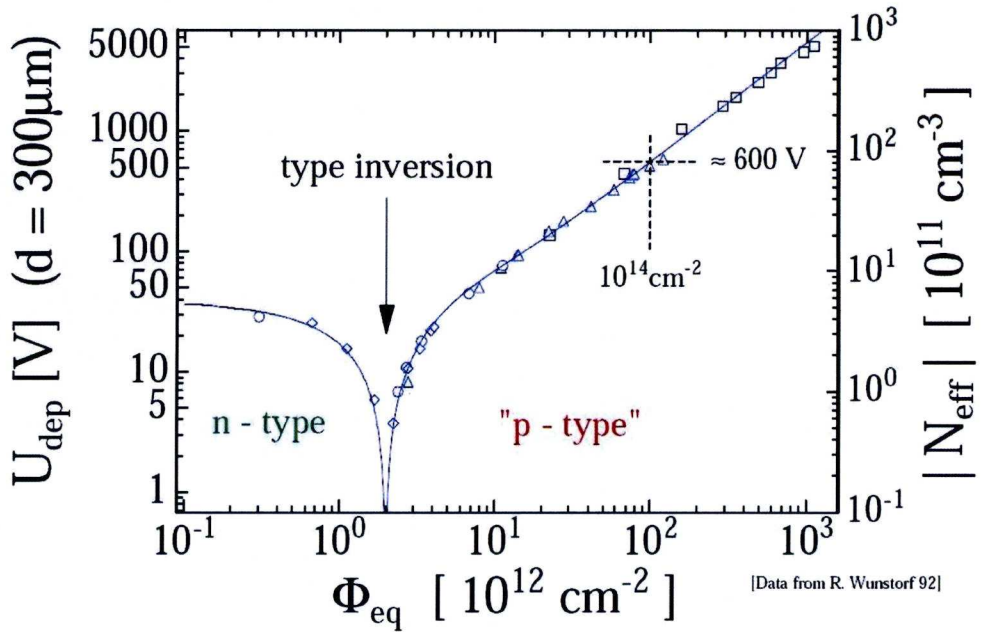

Figure 3.4: *The change in the effective doping concentration and the consequential change in the depletion voltage in irradiated silicon.*

of mobile holes, the depletion region does not constitute conventional p-type material. Operationally, this change in the net space charge requires a subsequent change in the applied bias voltage to maintain the effect of full depletion. In this respect the change in the net space charge is equivalent to a change in the doping concentration and for this reason the change in the net space charge is often referred to as a change in the effective doping concentration (N_{eff}). The change in the effective doping concentration with fluence is shown in Figure 3.4 for a typical p-in-n silicon sensor. As the depletion voltage increases with increasing fluence, it is possible that it may eventually exceed the point where, from an operational point of view, full depletion is not possible. If the sensor cannot be fully depleted, the signal charge will need to pass through a layer of undepleted silicon which can lead to reduced, broader signals. This is of particular importance to p-in-n sensors like those in the SCT as the depletion voltage grows from the backside of the sensor, meaning that any undepleted region will be positioned at the p-implant side where most of the charge is collected.

3.4 Review of Radiation Damage Parameterisations

As discussed in Section 3.2.1, due to annealing, radiation induced changes to the electrical properties of silicon sensors are not only dependent upon the fluence but also on the temperature and time spent after irradiation. Annealing can be supressed below 0 °C but at higher temperatures the electrical properties of the silicon sensors can change significantly over time. The observed changes in the electrical properties can result from of a number of underlying complex processes, which makes it difficult to develop a theoretical description of such changes from first principles. However, simple parameterisations have been developed from data which allow for predictions of how the macroscopic properties of the silicon sensors will evolve in a particular environment and, in particular, how they will evolve over the lifetime of an experiment. The changes in the effective doping concentration due to radiation damage and annealing is one of the limiting factors in determining the lifetimes of silicon sensors as this has the most significant impact on the charge collection efficiency and the achievable S/N. The parameterisation that is used to describe the evolution of the effective doping concentration with annealing is outlined below.

The effective doping concentration can be determined from both the initial doping concentration ($N_{eff,0}$) before irradiation and the radiation induced change in the effective doping concentration ($\Delta\ N_{eff}$) [21].

$$N_{eff} = N_{eff,0} - \Delta N_{eff} \tag{3.7}$$

The change in the effective doping concentration ΔN_{eff} after irradiation and annealing has three different contributing terms: a stable damage term $N_c(\Phi)$, a beneficial annealing term $N_a(\Phi, T, t)$ and a reverse annealing term $N_y(\Phi, T, t)$ [21].

$$\Delta N_{eff}(\Phi, T, t) = N_c(\Phi) - N_a(\Phi, T, t) - N_y(\Phi, T, t) \tag{3.8}$$

The first term is referred to as stable since it describes time-independent changes in the effective donor and acceptor concentrations. The latter two terms account for the annealing of the effective doping concentration after irradiation. These two terms describe changes which are dependent upon the dynamics of the radiation induced defect states and show a significant temperature dependence.

3.4.1 Stable Damage

The parameterisation of the stable damage contribution is shown in Equation 3.9 [21]. The first term describes the removal of donors, where N_{c_0} is the concentration of removable donors and is related to the initial doping concentration, whilst the second term describes the radiation induced creation of acceptors. The two parameters, c and g_c, are determined experimentally from a fit to data.

$$N_c(\Phi) = N_{c_0}\left(1 - \exp(-c\Phi)\right) + g_c\Phi \tag{3.9}$$

3.4.2 Beneficial Annealing

The parameterisation of the benefical annealing contribution is shown in Equation 3.10 [21]. This term represents the experimental observation that $|N_{eff}|$ initially decreases with annealing. Operationally, the decrease in $|N_{eff}|$ leads to a decrease in the depletion voltage and it is for this reason that this contribution is referred to as beneficial.

$$N_a(\Phi) = g_a\Phi \ \exp\left(\frac{-\Theta(T)t}{\tau_a}\right) \tag{3.10}$$

The time dependence is introduced through the time constant τ_a, which is defined as shown in Equation 3.11 [21]. The other parameter g_a is determined experimentally from a fit to data. For instances where the temperature remains constant, the scaling factor $\Theta(T)$ can be omitted.

$$\frac{1}{\tau_a} = k_a \exp\left(\frac{-E_a}{k_B T}\right) \tag{3.11}$$

For instances where the temperature changes during annealing, the appropriate treatment is to use the factor Θ(T) to scale the annealing time accordingly. This factor is defined by a standard Arrhenius relationship, as shown in Equation 3.12, relating the annealing at one temperature T to that at another reference temperature T_R [16].

$$\Theta(T) = \exp\left(\frac{E_a}{k_B}\left(\frac{1}{T_R} - \frac{1}{T}\right)\right) \tag{3.12}$$

In both cases, k_B is the Boltzmann constant and the activation energy E_a (and the constant k_a) are determined experimentally from an Arrhenius plot of the measured current as a function of temperature.

3.4.3 Reverse Annealing

Following the initial period of beneficial annealing, $|N_{eff}|$ is observed to increase again. This process is referred to as reverse annealing. A number of parameterisations have been suggested to describe this process, based on different assumptions with regards to the underlying behaviour of the lattice defects. A natural explanation for the observation of reverse annealing is that radiation induced lattice defects are initially electrically inactive and transform into active defects over a given time period. Two such mechanisms have been suggested through which such a process may occur: a first order description and a second order description. Each of these assumed mechanisms by which the radiation induced defects can slowly become active, lead to different parameterisations for the evolution of the effective doping concentration with annealing.

First Order Parameterisation

In the first order description it is assumed that the primary defect x that is responsible for the reverse annealing contribution is initially inactive before it decays to become an active defect y. Assuming that the decay rate is proportional to the defect concentration, the decay rate can be expressed as [26],

$$\frac{dN_y}{dt} = -\frac{dN_x}{dt} = k(T)N_x \tag{3.13}$$

where $k(T)$ is a temperature dependent decay constant. The solution of this equation describes the evolution of the concentration of the active defect y and defines the first order reverse annealing parameterisation [26]:

$$N_y(t) = N_{x_0}(1 - \exp(-t/\tau_y)) \tag{3.14}$$

where N_{x_0} is the initial concentration of inactive defects and the time constant $\tau_y = 1/k(T)$.

Second Order Parameterisation

In the second order description, it is assumed that two electrically inactive defects x_1 and x_2 are created which interact with each other to form an electrically active defect

y. Assuming that the decay interaction rate is now proportional to the product of the defect concentrations, the interaction rate can be expressed as [26],

$$\frac{dN_y}{dt} = -\frac{dN_{x_1}}{dt} = -\frac{dN_{x_2}}{dt} = k(T)N_{x_1}N_{x_2} \tag{3.15}$$

where $k(T)$ is a temperature dependent decay constant. If the concentration of one of the two electrically inactive defects dominates, then the description would lead back to the first order description. As a result, it is assumed that $N_{x_1,0} = N_{x_2,0} = N_{x,0}$, from which the solution describes the evolution of the concentration of the active defect y and defines the second order reverse annealing parameterisation [26]:

$$N_y(\Phi, t) = N_{x_0}\left(1 - \frac{1}{1 + kN_{x_0}t}\right) \tag{3.16}$$

Although both parameterisations lead to the same saturation value for the active y defect concentration, the evolutions of the concentrations in reaching this saturation value are different. In particular, the second order description suggests that the evolution is dependent upon the initial concentration of the inactive defects N_{x_0} which is itself dependent upon the fluence. Although early experimental evidence supported the second order approach, further experimental evidence was found to be inconsistent with the notion that the time evolution of the concentration was dependent upon the fluence. In order to account for this discrepancy, a more pragmatic parameterisation was developed by the Hamburg group which is based on a first order description of the defect reactions but modified to allow for a better fit to experimental data. From here onwards, this modified first order parameterisation will be referred to as the Hamburg parameterisation.

Hamburg Parameterisation

The Hamburg parameterisation of the reverse annealing contribution is shown in Equation 3.17 [27]. This alternative parameterisation is based on the assumption that the underlying reaction dynamics may be dominated by a first order process but with an additional contribution from another superimposed, unknown annealing process.

$$N_y(\Phi, t) = N_{x_0}\left(1 - \frac{1}{1 + t/\tau_y}\right) \tag{3.17}$$

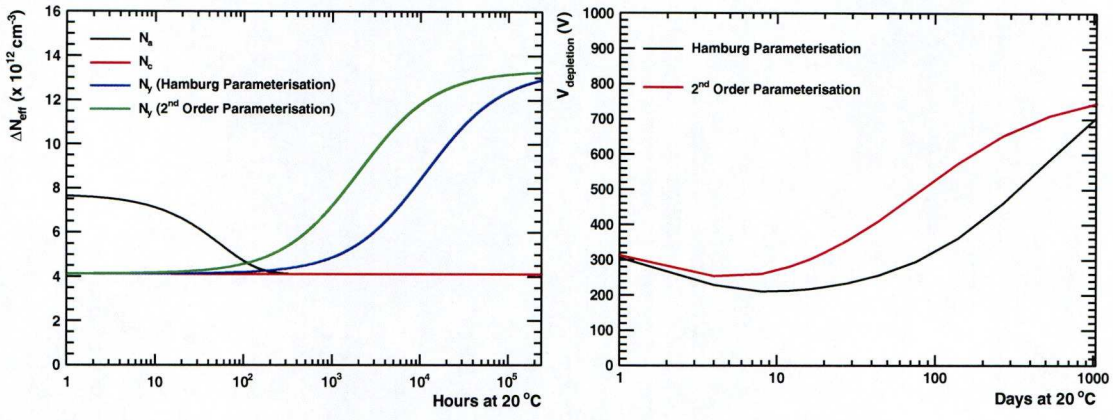

Figure 3.5: *The contributions to the typical evolution of the effective doping concentration in an irradiated silicon sensor are shown on the left. The impact of the two different parameterisations of the reverse annealing term on the depletion voltage is shown on the right.*

where $1/\tau = k(T)$. For short reverse annealing times (i.e. $t \ll \tau$), this parameterisation reduces to the first order parameterisation as is shown below [27].

$$\left(1 - \frac{1}{1 + t/\tau_Y}\right) \approx 1 - (1 - t/\tau_Y) = t/\tau_Y \tag{3.18}$$

$$1 - \exp(-t/\tau_Y) \approx 1 - (1 - t/\tau_Y) = t/\tau_Y \tag{3.19}$$

The full description of the parameterisation, including all three contributions, has been fitted to a broad range of experimental data using different materials, fluences and temperatures. From these data, average parameter values have been extracted and the results have been shown to be consistent and more or less independent of the irradiated sensor type. The resulting behaviour of the effective doping concentration with annealing is shown in figure Figure 3.5 for a typical annealing scenario. The parameterisation assumes that the annealing begins immediately after the irradiation, although in reality, in the context of a high energy physics experiment, the irradiation and the annealing occur concurrently. Nevertheless, the curve illustrates the importance of operating the detector at low temperature in order to supress the long-term effects of reverse annealing.

3.5 Predicted Evolution of Sensor Properties

The radiation damage parameterisations described in Section 3.4 allow us to predict how the effective doping concentration and thus the depletion voltage of the SCT silicon sensors will evolve over the full 10 year lifetime of the ATLAS detector. In order to make such predictions, the operational scenario of both the LHC and the ATLAS detector must be known. Specifically, knowledge of the particle fluences expected in the SCT (which are themselves dependent upon the expected luminosity profile) and the lengths of time that the SCT silicon sensors will spend at different temperatures are required.

A set of predictions were made in 1997 for the ATLAS TDR which assumed particular operational scenarios for the LHC and the ATLAS detector in terms of the sustained fluence and the temperature profile over time. The outcome of some of those predictions guided the design of the SCT silicon sensors and the associated cooling infra-structure. The parameterisation for the beneficial annealing contribution $\Delta Na(\Phi, t)$, as shown in Equation 3.10, was not included in the predictions as it represents a short term annealing effect and was therefore not considered to be significant over the full 10 year lifetime of the ATLAS detector. In addition, the reverse annealing contribution was described using the second order parameterisation, as shown in Equation 3.16. The prediction was that the evolution of the depletion voltage over the lifetime of the ATLAS experiment would lead to a maximum depletion voltage value of 218 V after 10 years of operation. Since the TDR predictions were made, both the LHC operational scenario and the ATLAS access and maintenance periods have been revised and it was therefore important that a new set of predictions were made in order to confirm that the silicon sensors can perform well over the full lifetime of the ATLAS experiment [16]. A continuously updating luminosity profile makes it difficult to determine the particle fluences that the SCT sensors will be exposed to over any given time period. More importantly, the lengths of the ATLAS access and maintenance periods are subject to change and it is possible that the length of time the sensors will stay above 0 °C each year will be longer than was assumed in the TDR predictions. In particular, it is now expected that the SCT may spend a period of up to 12 months warm during the installation of the pixel detector's insertable B-layer. In addition to the possibility of longer warm periods, it is also now believed that the SCTcooling system may not reach its design coolant temperature of -25 °C across the whole SCT, which may lead to an in-

crease in the temperature of the silicon sensors [16]. The possibility of increased sensor temperartures, coupled with longer warm periods leads to more significant annealing. With the new updated LHC operating scenario and an estimate of the expected annual ATLAS access and maintenance periods, the Hamburg parameterisation predicts a depletion voltage of 146 V after 10 years of operation, whereas the second order parameterisation predicts a depletion voltage of 181 V [28] over the same period. In the event that operations are extended beyond the 10 year lifetime, the predictions of the two parameterisations deviate more significantly. After 12 years of operation, the Hamburg parameterisation predicts a depletion voltage of 276 V but the second order parameterisation predicts a deletion voltage of 447 V [28]. This difference between the predictions of the two radiation damage parameterisations provides the motivation to perform detailed measurements of the performance of SCT silicon sensors after long periods of annealing. These measurements are also of importance in understanding how the sensors would perform if they were to be operated partially depleted and, in addition, they will allow us to predict the expected performance if the fluence, the temperature or the annealing time were to increase beyond our expectations.

3.6 Measured Evolution of Sensor Properties

A series of accelerated annealing measurements were performed on a pair of silicon microstrip sensors in order to study the evolution of the depletion voltage and determine whether the evolution is best described by the second order parameterisation or the Hamburg parameterisation of the reverse annealing process. The pair of silicon microstrip sensors used for the measurements were ATLAS mini (1cm x 1cm) Hamamatsu Photonics Ltd. sensors, identical in technology to those that are present in the SCT. The procedure involved irradiating the two silicon sensors (together) with neutrons to a 1 MeV neutron equivalent fluence of 2×10^{14} cm^{-2} at the 250 kW TRIGA Mark II research reactor in Ljubljana[5]. The irradiated sensors were then subjected to a programme of accelerated annealing, up to a maximum of 1000 days at 20 °C, as outlined in Table 3.1. At each step in the programme the sensors were exposed to extended

[5]This 1 MeV neutron equivalent fluence is 1.5 times the most up-to-date estimate of the maximum expected 1 MeV neutron equivalent fluence that the SCT is expected to experience over the lifetime of the ATLAS detector.

periods of high temperature which represented a given number of days at 20 °C. Then, after each period of annealing, a series of measurements were performed on the sensors. For one of the sensors the depletion voltage was determined through measurements of the sensors capacitance-voltage (C-V) characteristics. This is the most traditional way of measuring the depletion voltage but is considered less reliable when applied to irradiated sensors since it is more difficult to make comparisons with the parallel plate capacitor following radiation damage. The method is nevertheless considered sufficient to provide an accurate estimate of the depletion voltage of the sensor. To account for the fact that there is some uncertainty in how well the depletion voltage determined from C-V measurements relates to the voltage required for full efficiency, the second sensor was mounted on a copper chuck with a single wire bond and the charge collection was measured as a function of the applied bias voltage. These measurements provide a cross check of the effects of the annealing and are of particular importance since, in practice, it is ultimately the charge collection efficiency that limits the sensor performance. The experimental setups for both sets of measurements were designed to represent, as closely as possible, the expected environmental conditions of the SCT during operation. Throughout the data taking process and in between annealing periods, the silicon sensors were kept in a freezer maintained at a temperature of -10 °C and were continuously flushed with Nitrogen.

3.6.1 Depletion Voltage

The C-V characteristics of the sensor were measured by a Wayne Kerr 6430B LCR meter operating in parallel mode, with a Keithly 2410 source meter providing the bias voltage. The amplitude and frequency of the AC signal applied to the sensor were set to 1 V and 1 kHz respectively. The (reverse) bias voltage was increased in intervals of 10 V from -10 V to -600 V and at each interval dedicated software recorded both the bias voltage and the average of 10 sampling capacitance measurements. Two straight lines were fitted to each of the resulting $(1/C^2) - V$ profiles, one before and one after the point at which the capacitance saturates, as shown in Figure 3.6. The bias voltage at the intercept of the two straight lines was then identified as the depletion voltage of the sensor. The uncertainty on the measured depletion voltage is dominated by the uncertainty introduced through the fitting procedure. Contributions from the uncertainties in the measurements of the capacitance and voltage are negligible in

Annealing Program			Equivalent Days at 20 °C
Step	Temperature (°C)	Time (hours)	
1	50	0.74	4
2	50	0.74	8
3	50	0.74	12
4	50	0.74	16
5	50	0.74	20
6	50	1.48	28
7	60	0.71	44
8	60	1.42	76
9	70	0.75	140
10	70	1.50	268
11	80	0.79	523
12	80	1.59	1036

Table 3.1: *The accelerated annealing programme, indicating the time that the sensors spent at different temperatures and the equivalent degree of annealing expressed in days at 20* °C. *The annealing time at each annealing step is scaled according to a standard Arrhenius relationship, like that shown in Equation 3.12, in order to determine the equivalent number of days at 20* °C. *In this manner, high temperatures can be used to quickly achieve the effects of long-term room temperature annealing. The activation energy used in the Arrhenius scaling is 1.33 eV, which is considered the standard value. Although this method of scaling is currently the standard method for accelerated annealing studies, its validity is now being investigated within the RD50 Collaboration.*

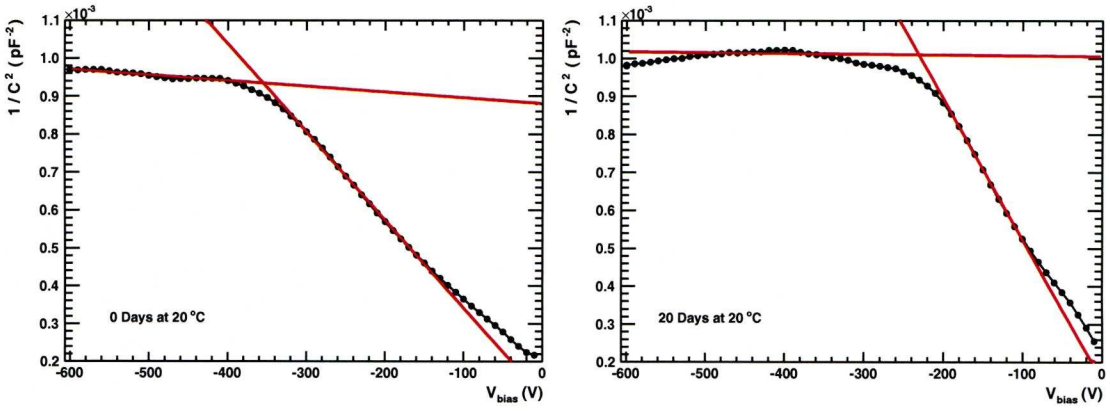

Figure 3.6: *The measured* $(1/C^2) - V$ *profile of the irradiated silicon microstrip sensor prior to annealing (left) and after a period of 20 days at 20* °C *(right). The black dots represent the data whilst the red lines show the applied straight line fits and the resulting intercept that indentifies the depletion voltage of the sensor.*

comparison. The uncertainty on the depletion voltage was estimated to be ±15 V. This value was obtained by varying the fitting ranges and observing the resulting effect on the value of the depletion voltage.

The measured evolution of the depletion voltage and the predictions of the radiation damage parameterisations are shown in Table 3.2. The initial depletion voltage measured prior to annealing was found to be 355 V which is within 0.5% (1.2%) of the value predicted when using the second order (Hamburg) reverse annealing parameterisation. Over the period corresponding to ∼20 days at 20 °C, the beneficial annealing process reduces the depletion voltage to a minimum value of ∼230 V. The minimum in the predicted depletion voltage occurs after ∼4 days (∼8 days) at 20 °C for the second order (Hamburg) parameterisation and although the positions of the minima are quite different, the measured and predicted values at these minima are quite similar. The reverse annealing process then begins to dominate and the depletion voltage starts to increase. After a period of 1036 days at 20 °C, the depletion voltage increased to a value of 408 V. The predicted depletion volatge at this point is 54.8% (58.0%) greater than the measured value for the second order (Hamburg) parameterisation. The measured evolution of the depletion voltage and the predictions of the radiation damage parameterisations are also shown in Figure 3.7. The measurements suggest that the effect of annealing on the depletion voltage is slower than that predicted by both of the

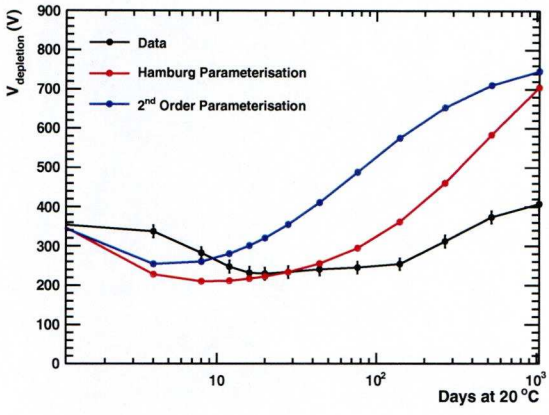

Figure 3.7: *The predicted and measured evolutions of the depletion voltage with annealing time. The black line represents the data and whilst the blue (red) line represents the prediction of the radiation damage parameterisation, described in Section 3.4, when using the second order (Hamburg) description of the reverse annealing process.*

two parameterisations and, in general, the data appears to be more consistent with the predictions of the Hamburg parameterisation.

3.6.2 Charge Collection Efficiency

To measure the charge collection the sensor was wire-bonded to a (non-irradiated) SCT128A analogue readout chip [29] clocked at LHC speed (40 MHz clock and 25 ns shaping time). A Strontium-90 electron source positioned above the sensor generated the signal whilst a scintillator placed beneath the sensor triggered the readout. The system was then calibrated to the Most Probable Value (MPV) of the energy loss for a minimum ionising particle in a non-irradiated, 300 μm thick silicon sensor. For each triggered event, clusters are formed from the strip with the largest S/N and its neighbouring strips. If the S/N of the cluster seed strip and its neighbouring strips exceed the threshold values of 3.0 and 1.8 respectively, their collected charge is summed and the corresponding cluster charge in that event is recorded. The resulting distribution of the cluster charge from all triggered events, as shown in Figure 3.8, is fitted with a convolution of Landau and Gaussian distributions and the MPV is recorded. To obtain a clean distribution of the cluster charge, noisy channels and channels with low hit frequencies are masked out such that they cannot contribute to the cluster formation. The (reverse) bias voltage was increased in intervals of 100 V from -200 V to -900 V

Days at 20 °C	Measured Depletion Voltage (V)	Predicted Depletion Voltage (V)	
		Second Order	Hamburg
0	355 ± 15	353.6	359.6
4	338 ± 15	254.3	228.3
8	283 ± 15	260.3	210.5
12	248 ± 15	280.4	212.3
16	232 ± 15	301.0	217.4
20	230 ± 15	320.3	223.1
28	234 ± 15	354.8	234.4
44	241 ± 15	410.4	255.9
76	246 ± 15	487.5	295.3
140	254 ± 15	574.4	361.9
268	313 ± 15	652.5	461.0
523	374 ± 15	709.5	583.3
1036	408 ± 15	745.0	704.0

Table 3.2: *The predicted and measured values of the depletion voltage after each step in the annealing programme.*

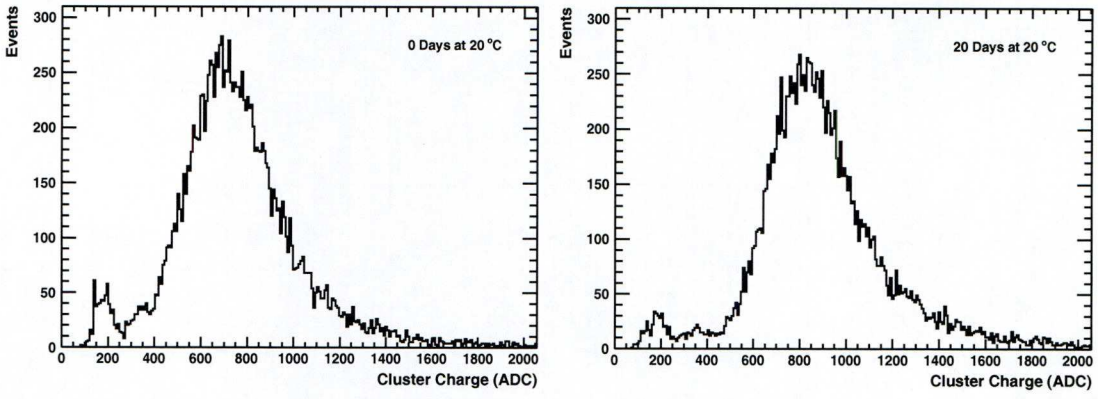

Figure 3.8: *The cluster charge distributions for events at a reverse bias voltage of 400 V prior to annealing (left) and after a period of 20 days at 20 °C. The calibration of the system is such that 1 ADC represents a charge equivalent to 22.40 electrons.*

and at each interval the MPV was measured. The uncertainty in the measured charge collection includes an uncertainty of ±4 ADC (Analogue to Digital Converter) counts on the MPV of the cluster charge distribution and as well as a 5% calibration uncertainty in the relationship between the ADC count and the corresponding number of electrons.

The measured evolution of the charge collection with annealing is shown in Figure 3.9. The measurements show a short term improvement followed by a gradual decrease in the charge collected by the sensor with annealing time. At the lowest bias voltages there is a smooth fall off in the collected charge, which begins after approximately 100 days at 20 °C. This decrease can be attributed to the fact that the depletion voltage of the sensor is beginning to increase more steeply as the reverse annealing process becomes more dominant. This can be seen more clearly if the measured evolution of the charge collection is compared to the measured evolution of the depletion voltage shown in Figure 3.7. In addition, the effect of radiation induced trapping centres in the sensor bulk become more significant with annealing and can also lead to a reduction in the collected charge. At higher bias voltages more charge is collected as the sensor becomes more over-depleted and the increasing electric field across the depletion region begins to mitigate the effects of the radiation induced trapping centres. The ratio of the charge collection measured after each period of annealing to the charge collection measured prior to annealing, is shown in Figure 3.10. The most significant increase in the charge collection occurs at the lower reverse bias voltages, whereas at the higher

bias voltages the charge collection effectively remains constant. This is expected because at the lower bias voltages, the sensor is more sensitive to the evolution of the depletion voltage with annealing than at the higher bias voltages were the sensor remains in a constant state of over-depletion. For instance, at the reverse bias voltage of 300 V, where the largest increase in the charge collection is observed, the sensor is initially under-depleted prior to annealing. As the depletion voltage decreases with annealing the sensor becomes more depleted, eventually becoming over-depleted and the charge collection responding accordingly. Furthermore, a direct comparison of the two independent measurements of the evolution of the depletion voltage and the charge collection are shown in Figure 3.11. The data show strong correlations between the measured depletion voltage and the measured charge collection in the two sensors and thus the independent measurements appear to be consistent.

3.7 Implications for the Long-Term Operation of the SCT

The relatively slow evolution observed in the measured depletion voltage with annealing suggests that predictions for the long-term performance of the SCT based on the radiation damage parameterisations described in Section 3.4 would be overly pessimistic. However, as previously mentioned, the validity of the scaling factors used to relate the period of annealing to an equivalent number of days at 20 °C are are currently under scrutiny within the RD50 Collaboration. More important conclusions can be obtained from the charge collection measurements since it is ultimately the charge collection efficiency that limits the sensor performance. In particular, the data show that when the applied bias voltage is significantly higher than the full depletion voltage the collected charge increases significantly. This effect is shown more clearly in Figure 3.12. This is consistent with an observation made during the original research and development program for the SCT which showed that the collected signal on an irradiated silicon sensor saturated at a bias voltage of $\sim$100 V higher than the depletion voltage. It had not been previously confirmed whether or not this behaviour would still be observed after long-term annealing.

The most significant implication for the long-term operation of the SCT is that the data suggest that the sensors should be able to operate sufficiently for the full lifetime of the ATLAS experiment. The sensors in these measurements have been exposed to a

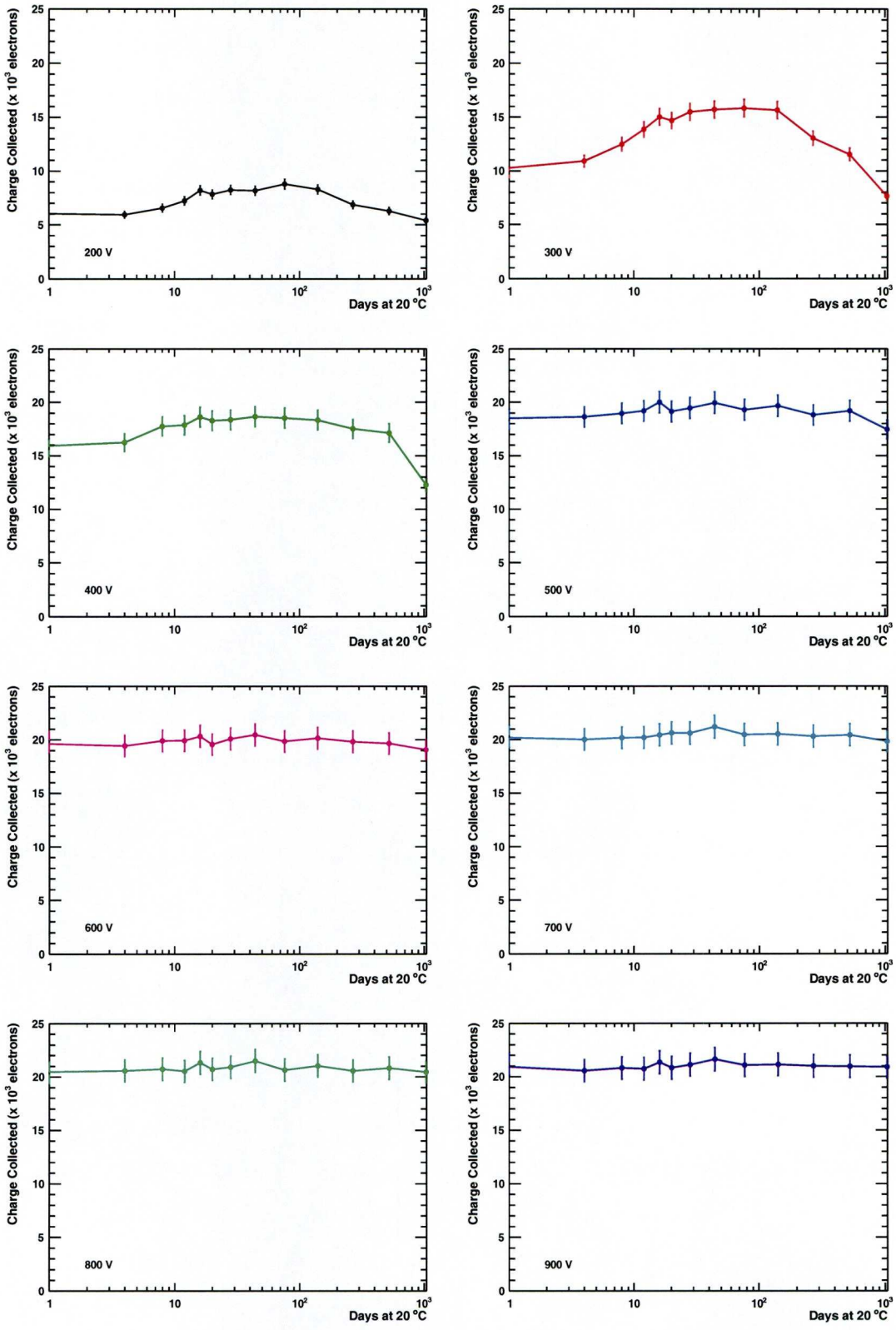

Figure 3.9: *The charge collected by the irradiated silicon microstrip sensor as a function of the annealing time for a number of different bias voltages.*

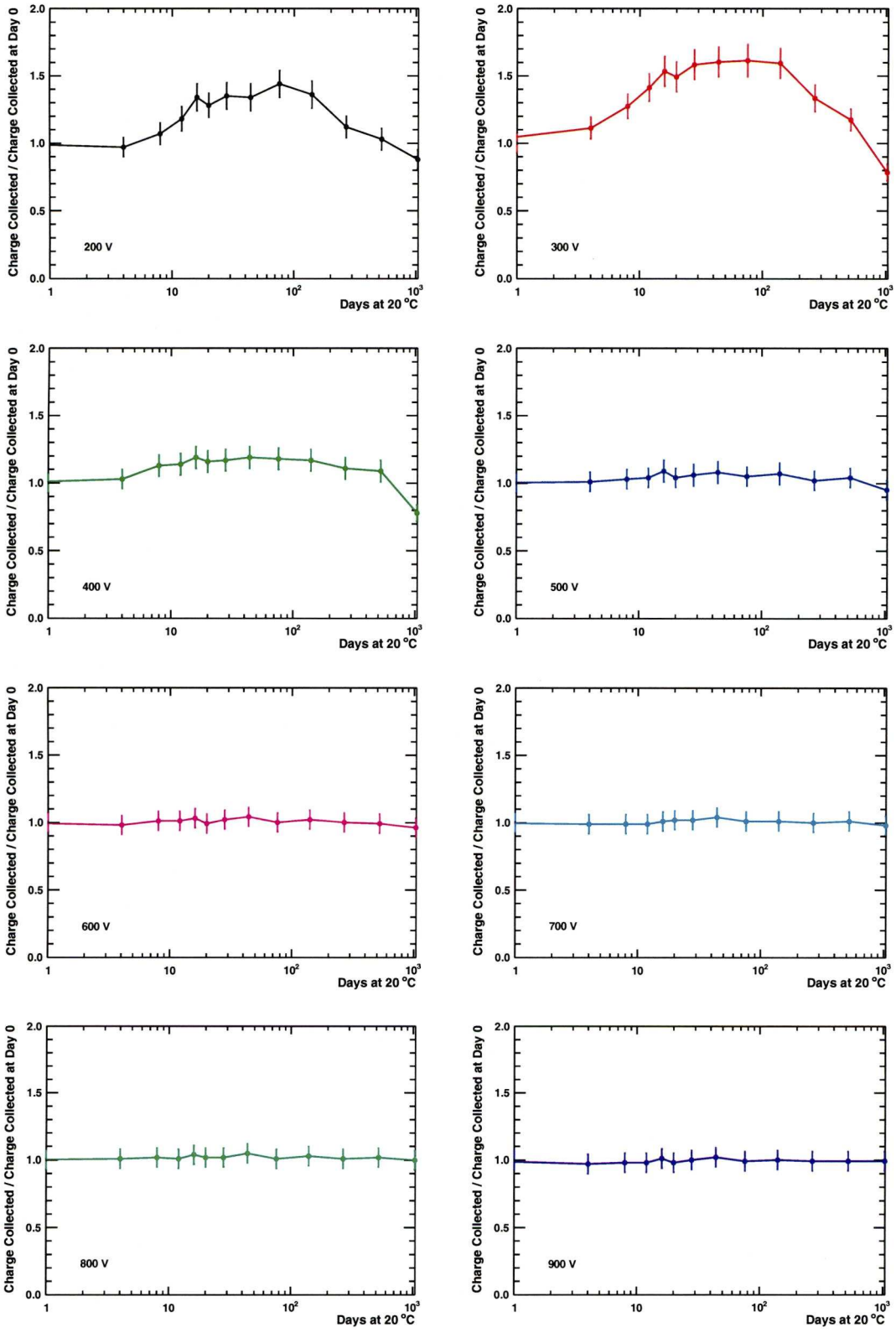

Figure 3.10: *The ratio of the charge collected by the irradiated silicon microstrip sensor to the charge collected prior to annealing as a function of annealing time for a number of different bias voltages.*

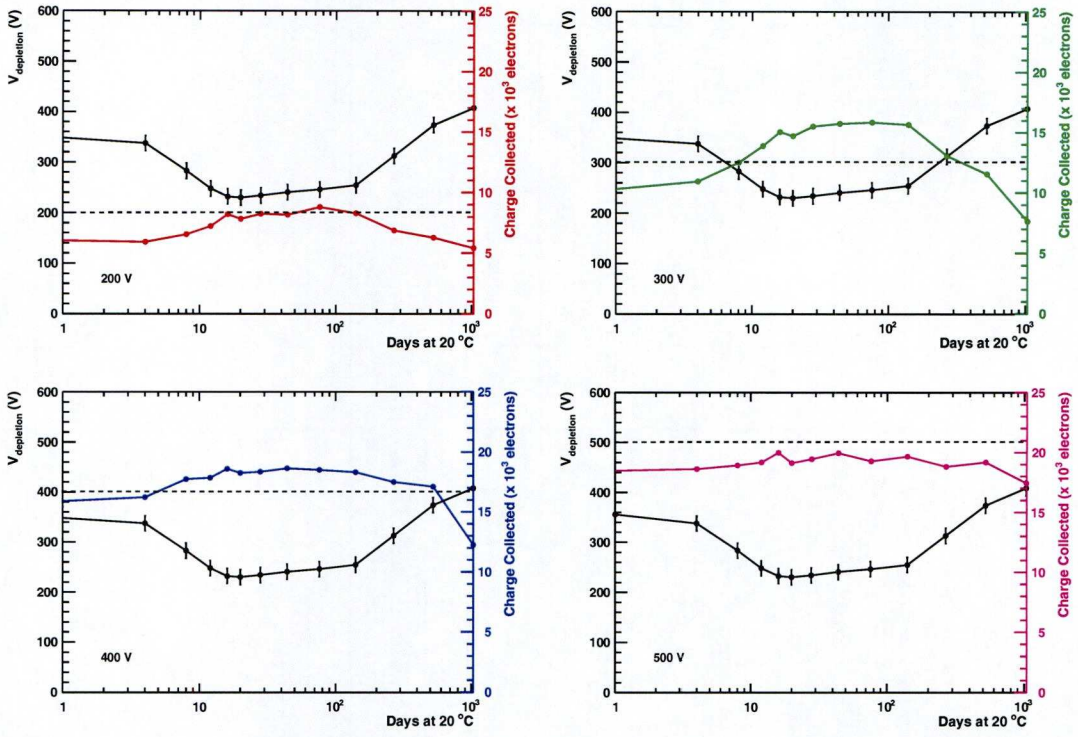

Figure 3.11: *The measured evolution of the depletion voltage and the measured charge collection at 200* V *(top left), 300* V *(top right), 400* V *(bottom left) and 500* V *(bottom right) as a function of the annealing time.*

fluence that is approximatley 50% greater than the expected maximum fluence in the SCT over its 10 year lifetime and they have been annealed to an equivalent of over 1000 days at 20 °C, which is much longer than what is expected. Nevertheless, even after this high fluence and long annealing period the sensor still exhibits significant charge collection capabilities. This can be seen most clearly in Figure 3.11, which shows that at a reverse bias voltage of 400 V (which is expected to be achievable), the sensor still collects approximately 12,300 electrons. This value is almost twice the nominal SCT binary readout threshold of 1 fC, which corresponds to ~6200 electrons.

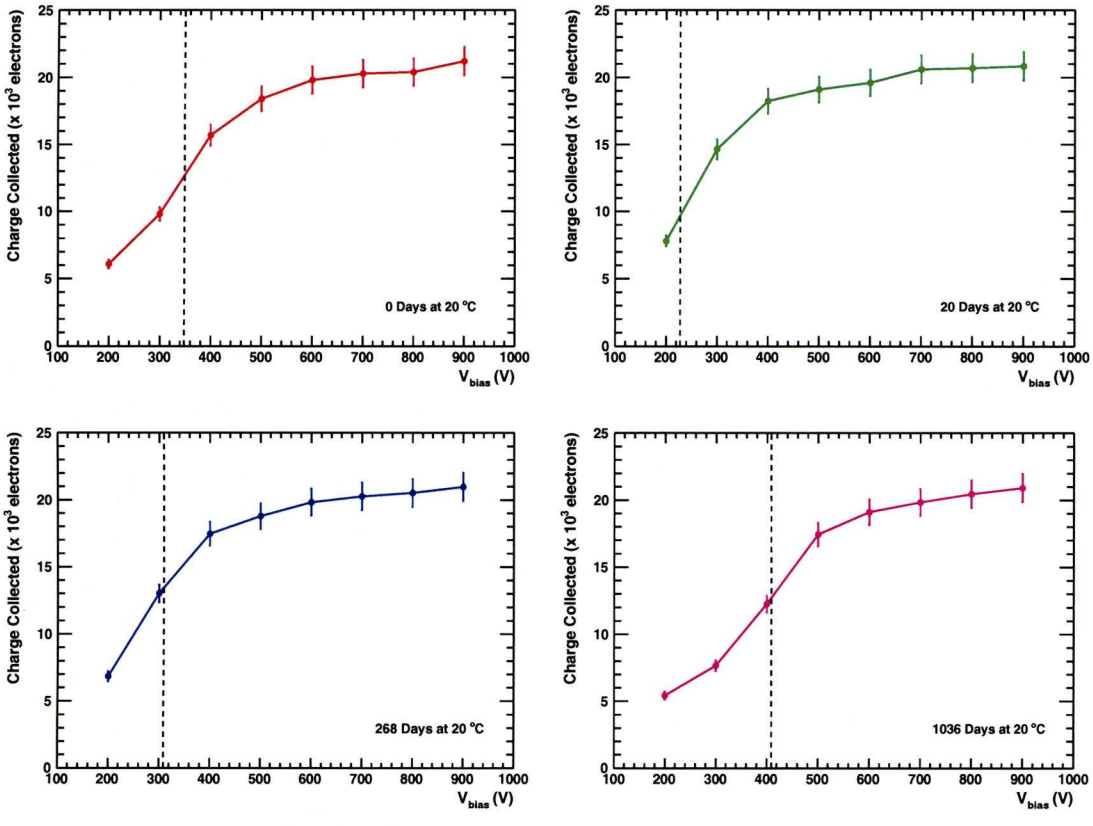

Figure 3.12: *The charge collected by the irradiated silicon microstrip sensor as a function of the reverse bias voltage for different periods of annealing. The dotted lines indicate the depletion voltages as determined from the corresponding C-V measurements.*

Chapter 4

The Standard Model Higgs Boson

The Standard Model of particle physics is a theoretical model describing the fundamental constituents of matter and the interactions between them. The theory has proved to be extremely successful as almost all experimental observations in particle physics have been consistent with its predictions[6]. The model comprises a small number of elementary point like particles of two distinct families: half-integer spin fermions and integer spin bosons. The fermions make up the matter and anti-matter of the universe whilst the bosons mediate the interactions between them. The particle content of the Standard Model is summarised in Table 4. Of the four known fundamental interactions, only three are described within the Standard Model: the electromagnetic and the weak interactions, which are manifestations of a unified electroweak force and the strong interaction. The electromagnetic interaction is mediated by the photon (γ), the weak interaction is mediated by the W^+, W^- and Z bosons and the strong interaction is mediated by the gluon (g). A description of gravitational interactions has not yet been accommodated within the Standard Model.

The fermions are classified into three generations, the first of which contains the particles that make up conventional matter. Within each generation the particles are

[6]The Standard Model assumption that neutrinos are massless is inconsistent with experimental observations of neutrino flavour oscillation which imply non-zero neutrino masses [30]. In addition, precision measurements of the anomalous magnetic moment of the muon indicate a discrepancy from the Standard Model prediction at the $\sim 3\sigma$ level [31].

	Fermions			Bosons
	I	II	III	
Quarks	u	c	t	γ
	d	s	b	g
Leptons	ν_e	ν_μ	ν_τ	Z
	e	μ	τ	W

Table 4.1: *The particle content of the Standard Model. Each fermion in the table also has a corresponding anti-fermion with opposite electric charge.*

further classified into quarks and leptons. Both the quarks and leptons can interact via the electromagnetic interaction[7] and the parity violating weak interaction but only the quarks can interact via the strong interaction. Furthermore, unlike the leptons the quarks do not appear free in nature as they are confined in bound states of either three quarks or quark anti-quark pairs. These compound states are known as baryons and mesons respectively and are referred to collectively as hadrons.

The fermions and bosons are derived concepts originating from the quantisation of associated fields. The nature of the interactions between fermions can be inferred by imposing particular forms of local gauge invariance upon the Lagrangians that describe the dynamics of the fermion fields. As such, each of the fundamental interactions described within the Standard Model are subsequently associated with an invariance under the action of a particular transformation group. Enforcing each of these symmetries requires the introduction of a number of additional massless vector gauge fields which, upon quantisation, can be associated with the (gauge) bosons that mediate the corresponding interaction. The details of all the interactions within the Standard Model can be inferred by requiring that the complete Standard Model Lagrangian is invariant under $\mathrm{SU}(3)\times\mathrm{SU}(2)_L\times\mathrm{U}(1)_Y$ transformations. The SU(3) symmetry leads to a theoretical description of strong interactions, known as Quantum ChromoDynamics (QCD), in which 8 massless gauge fields are introduced that are directly related to the

[7]Only the charged leptons interact via the electromagnetic interaction.

8 massless gluons that mediate the strong interaction. The non abelian nature of the SU(3) group leads to self-coupling of the gauge fields and subsequently to a rich and complex phenomenology. The $\mathrm{SU}(2)_L \times \mathrm{U}(1)_Y$ symmetry leads to a theoretical description of electroweak interactions, where the subscript L denotes the fact that only the left handed component of the fermion fields are involved and the subscript Y indicates that the generator of the U(1) symmetry is the weak hypercharge Y, distinguishing it from the more familar $\mathrm{U}(1)_{EM}$ symmetry which leads to a theoretical description of electromagnetic interactions, known as Quantum ElectroDynamics (QED). However, the unified electroweak theory requires the introduction of four massless gauge fields which is inconsistent with the experimental observation that the three bosons mediating the weak interaction are massive. Explicitly adding the required mass terms to the electroweak Lagrangian would break the gauge invariance and so the gauge bosons instead obtain their masses by the phenomena of electroweak symmetry breaking in what is known as the Higgs mechanism [32, 33, 34]. Through the Higgs mechanism, the $\mathrm{SU}(2)_L \times \mathrm{U}(1)_Y$ symmetry of the electroweak interactions is broken leaving only a U(1) symmetry, which is identified with the $\mathrm{U}(1)_{EM}$ symmetry of electromagnetism. The breaking of the symmetry generates masses for the two charged bosons and the neutral boson of the weak interaction whilst ensuring that the photon of the electromagnetic interaction remains massless.

Despite the success of the Standard Model there are a number of reasons to believe that it is only an effective theory; a low energy approximation of a more fundamental theory. In particular, the Standard Model does not yet provide any description of gravitational interactions and in its current state has a total of 19 free parameters which must be determined experimentally. In addition, in the unified electroweak sector of the Standard Model, the $\mathrm{SU}(2)_L \times \mathrm{U}(1)_Y$ symmetry describes an invariance under the action of the product of two disconnected sets of transformations which provide a pair of independent coupling constants. For the electroweak theory to be defined by a single coupling constant, the $\mathrm{SU}(2)_L \times \mathrm{U}(1)_Y$ symmetry must be embedded within a larger group of transformations G and if this were to be the case, then it would be natural to assume that there is a group which can also include the SU(3) symmetry, such that,

$$G \subset \mathrm{SU}(3) \times \mathrm{SU}(2)_L \times \mathrm{U}(1)_Y. \tag{4.1}$$

Enforcing an invariance under such a grand unified gauge group G would then allow the three Standard Model interactions to be unified such that they are all described by a single coupling constant. The running of the coupling constants to high energies suggests that they do approach each other at an energy of about 10^{16} GeV. A number of theories which go beyond the Standard Model attempt to address the problems of the current model whilst ensuring that the coupling constants converge at this grand unification scale.

4.1 The Electroweak Theory and the Higgs Mechanism

In the Standard Model the Lagrangian for the electroweak interaction of fermions (neglecting fermion masses) is given by [35, 36],

$$\mathcal{L}_{\mathrm{EW}} = \mathrm{i}\Psi_L^\dagger \gamma^\mu D_{L\mu} \Psi_L + \mathrm{i}\psi_{\mathrm{R}}^\dagger \gamma^\mu D_{R\mu} \psi_{\mathrm{R}} - \frac{1}{4}\boldsymbol{W}_{\mu\nu} \cdot \boldsymbol{W}^{\mu\nu} - \frac{1}{4} B_{\mu\nu} B^{\mu\nu} \tag{4.2}$$

where the left handed fermion field, Ψ_L is a weak isospin doublet and the right handed fermion field, ψ_{R} is a weak isospin singlet. The covariant derivatives are given by,

$$D_{L\mu} = \partial_\mu + \mathrm{i}\frac{g'}{2} Y_L B_\mu + \mathrm{i}\frac{g}{2} \boldsymbol{I} \cdot \boldsymbol{W}_\mu \tag{4.3}$$

$$D_{R\mu} = \partial_\mu + \mathrm{i}\frac{g'}{2} Y_R B_\mu \tag{4.4}$$

where g' and g are the coupling constants, Y_L and Y_R are the weak hypercharges and $\boldsymbol{I}$ is the weak isospin. The components of $\boldsymbol{I}$ are non-commuting, thus making the electroweak theory a non-abelian theory. The last two terms, which describe the kinetics of the gauge fields, are given by,

$$\boldsymbol{W}_{\mu\nu} = \partial_\mu \boldsymbol{W}_\nu - \partial_\nu \boldsymbol{W}_\mu - g \boldsymbol{W}_\mu \times \boldsymbol{W}_\nu \tag{4.5}$$

$$B_{\mu\nu} = \partial_\mu B_\nu - \partial_\nu B_\mu \tag{4.6}$$

The cross product term in $\boldsymbol{W}_{\mu\nu}$ describes the self-couplings of the $\boldsymbol{W}_\mu$ gauge fields and is representative of the non-abelian nature of the theory.

As previously mentioned, the gauge fields $\boldsymbol{W}_\mu$ and B_μ are massless fields and therefore cannot directly represent the massive gauge bosons observed to mediate the weak interaction. The massive weak bosons can be accounted for in the theory through the the Higgs mechanism, which involves the introduction of an isospin doublet of complex scalar fields with weak hypercharge $Y = 1$,

$$\phi(x) = \begin{pmatrix} \phi^+(x) \\ \phi^0(x) \end{pmatrix} = \frac{1}{\sqrt{2}} \begin{pmatrix} \phi_1(x) + \mathrm{i}\phi_2(x) \\ \phi_3(x) + \mathrm{i}\phi_4(x) \end{pmatrix} \tag{4.7}$$

The dynamics of this isospin doublet are described by the $\mathrm{SU}(2)_L \times \mathrm{U}(1)_Y$ gauge invariant Lagrangain,

$$\mathcal{L}_\mathrm{H} = D_{L\mu}\phi^\dagger D_L^\mu \phi - V(\phi) \tag{4.8}$$

where the potential $V(\phi)$ is of the form,

$$V(\phi) = \mu^2 \phi^\dagger \phi + \lambda(\phi^\dagger \phi)^2. \tag{4.9}$$

For the conditions $\mu < 0$ and $\lambda > 0$, the potential has minima at a finite value of $\phi^\dagger\phi$ rather than at ϕ=0 which is given by,

$$\phi^\dagger \phi = \frac{1}{2}(\phi_1^2 + \phi_2^2 + \phi_3^2 + \phi_4^2) = \frac{-\mu^2}{2\lambda}. \tag{4.10}$$

The vacuum state is not unique and an arbitrary choice of one of the degenerate ground states will hide the $\mathrm{SU}(2)_L \times \mathrm{U}(1)_Y$ symmetry. Without loss of generality the ground state can be chosen as,

$$\phi(x)_0 = \frac{1}{\sqrt{2}} \begin{pmatrix} 0 \\ v \end{pmatrix} \tag{4.11}$$

where v is the vacuum expectation value given by $v = \sqrt{-\mu^2/2\lambda}$. The original choice of the field $\phi(x)$ with weak hypercharge $Y = \frac{1}{2}$, ensures that whilst both the $\mathrm{SU}(2)_L$ and $\mathrm{U}(1)_Y$ symmetries are broken the $\mathrm{U}(1)_{EM}$ symmetry remains unbroken, such that the vacuum remains invariant under $\mathrm{U}(1)_{EM}$ transformations and the photon remains massless.

Perturbative calculations involve expansions around the classical minimum, in which fluctuations of the field ϕ from the vacuum state ϕ_0 can be parameterised in terms of four real scalar fields. However, through the gauge invariance of $\mathcal{L}_{\mathrm{H}}$ a particular gauge, known as the unitarity gauge, can be found in which three of the four fields are gauged away to leave just one real scalar field $H(x)$. The field ϕ can therefore be parameterised as,

$$\phi(x) = \frac{1}{\sqrt{2}} \begin{pmatrix} 0 \\ v + H(x) \end{pmatrix} \tag{4.12}$$

By subtituting this field $\phi(x)$ into $\mathcal{L}_{\mathrm{H}}$, the gauge bosons of the weak and the electromagnetic interactions can then be identified with the following normalised combinations of the gauge fields:

$$W_\mu^+ = \frac{W_\mu^1 - \mathrm{i}W_\mu^2}{\sqrt{2}} \tag{4.13}$$

$$Z_\mu = \frac{gW_\mu^3 - g'B_\mu}{\sqrt{g^2 + g'^2}} \tag{4.14}$$

$$W_\mu^- = \frac{W_\mu^1 + \mathrm{i}W_\mu^2}{\sqrt{2}} \tag{4.15}$$

$$A_\mu = \frac{g'W_\mu^3 + gB_\mu}{\sqrt{g^2 + g'^2}} \tag{4.16}$$

which have associated tree level masses of:

$$M_W = \frac{1}{2}vg \tag{4.17}$$

$$M_Z = \frac{1}{2}v\sqrt{g^2 + g'^2} \tag{4.18}$$

$$M_A = 0 \tag{4.19}$$

In spontaneously breaking the $\mathrm{SU}(2)_L \times \mathrm{U}(1)_Y$ symmetry, the three degrees of freedom corresponding to the three real scalar fields that were gauged away have been taken up by the gauge fields and are manifest as the longitudinal polarisations of the massive vector bosons of the weak interaction. The $\mathrm{SU}(2)_L \times \mathrm{U}(1)_Y$ symmetry is still present but is now hidden and the required mass terms have been generated without destroying the gauge invariance.

The normalised combinations of the gauge fields can also be written in terms of the Weinberg angle θ_W which represents the degree mixing between the gauge fields, such that,

$$Z_\mu = \cos\theta_W W_\mu^3 - \sin\theta_W B_\mu \tag{4.20}$$

$$A_\mu = \sin\theta_W W_\mu^3 + \cos\theta_W B_\mu. \tag{4.21}$$

The relationship between the masses of the $W_\mu^\pm$ and Z_μ fields can now be expressed as,

$$\frac{M_W}{M_Z} = \cos\theta_W. \tag{4.22}$$

This relationship between the masses of the $W^\pm$ and Z bosons is a prediction of the Standard Model with its implementation of the Higgs mechanism. However, the most significant predcition of the Higgs mechanism is the existence of a massive scalar spin-0 particle which comes from the quantisation of the one remaining real scalar field that was not gauged away. This particle is known as the Higgs boson and its mass (m_H) is given by,

$$m_H = \sqrt{-\mu^2} = \sqrt{2\lambda}v. \tag{4.23}$$

The vacuum expectation value v can be directly related to the Fermi coupling constant G_F describing weak interactions at low energy. The experimental determination of G_F leads to a vacuum expectation value of $v = (\sqrt{2}G_F)^{-1/2} = 246$ GeV [35]. The only remaining parameter in the Higgs mechanism, the quartic self coupling term λ remains unknown and, as a result, the mass of the Higgs boson cannot be predicted.

4.2 Constraints on the Standard Model Higgs Boson Mass

The mass of the Higgs boson is a free parameter in the Standard Model and at the present time remains largely unconstrained. However, direct searches for the Standard Model Higgs boson in previous experiments have constrained production cross sections and in doing so have excluded a significant range of masses to provide a lower limit on the value of m_H. In addition, a number of theoretical constraints can be derived from assumptions on the energy range beyond which the Standard Model fails and new physics phenomena emerges. These theoretical constraints, along with indirect experimental constraints together provide a plausible upper limit on the value of m_H.

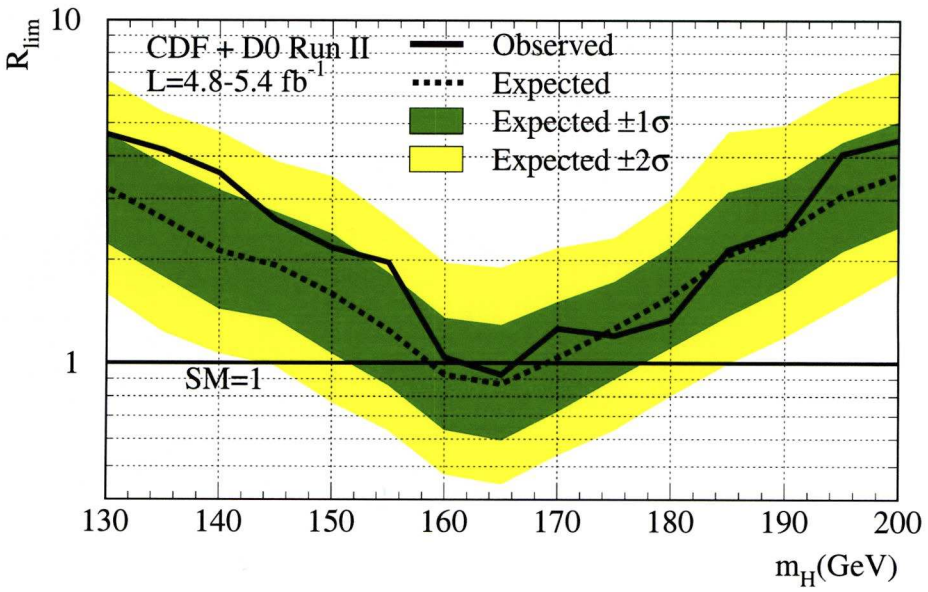

Figure 4.1: *The observed and the median expected (for the background only hypothesis) upper limits on Standard Model Higgs boson production at the Tevatron at 95% confidence level. These results are presented in terms of R_{lim}, the ratio of the observed/expected upper limit to the rate predicted by the Standard Model, as a function of m_H. A value of R_{lim} less than or equal to one excludes the Standard Model Higgs boson at 95% confidence level. The shaded bands indicate the 68% and 95% probabililty regions in which the expected R_{lim} is expected to fluctuate. A value of the observed R_{lim}, well above the upper 2σ region would indicate the existence of additional physics beyond that which is expected from background [38].*

Experimental Constraints

Direct searches at the LEP collider have set a lower limit on m_H of 114.4 GeV at 95% confidence level (CL) [37]. In addition, on-going searches at the Tevatron have now also excluded the range $162 < m_H < 166$ GeV at 95% CL [38] as shown in Figure 4.1.

Within the Standard Model framework, precision electroweak data used to test the validity of the Standard Model can also be used to infer information about the models fundamental parameters. Indirect constraints can be placed on m_H due to the sensitivity of Standard Model parameters to m_H through loop corrections. Unfortunately, the parameters have only a logarithmic dependence on m_H and hence these constraints are relatively weak. Assuming the overall validity of the Standard Model, a global fit

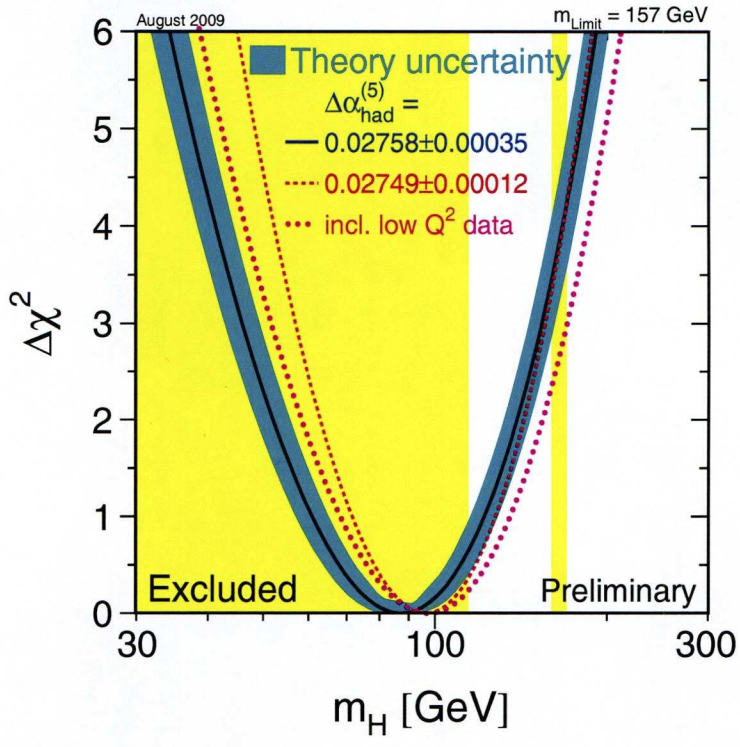

Figure 4.2: *The value of* $\Delta\chi^2 = \chi^2 - \chi^2_{min}$ *observed for a global fit to all measured electroweak parameters as a function of* m_H*. The blue band represents an estimate of the theoretical uncertainty due to missing higher order corrections and the yellow bands indicate the regions excluded at 95% confidence level by direct searches [39].*

to precision electroweak data from LEP, the Stanford Linear Collider, LEP-II and the Tevatron provides an indirect upper limit on m_H of 157 GeV at 95% CL [39], taking the theoretical uncertainty from missing higher order diagrams into account. This is shown in Figure 4.2. If the direct search limit from LEP-II is also taken into account in the fit, this indirect upper limit on m_H increases to 186 GeV at 95% CL [39].

Theoretical Constraints

Scattering processes involving longitudinally polarised bosons of the weak interaction can provide some insight to the electroweak theory since the the longitudinal polarisation states have their origins in the Higgs mechanism through which the bosons obtain their masses. The amplititudes of such scattering processes at high energies are propor-

tional to the coupling constant, λ. By requiring that the scattering amplitudes respect unitarity, a limit can be derived for the value of λ. From Equation 4.23, this in turn leads to a limit on the m_H, which at tree level is given by [40],

$$m_H < \sqrt{\frac{8\pi\sqrt{2}}{3G_F}} \approx 1 \text{ TeV}. \tag{4.24}$$

This means that if the Standard Model Higgs boson exists and is more massive than this limit, then some other new physics beyond the Standard Model must be present at the TeV scale to restore unitarity in the scattering of longitudinally polarised gauge bosons.

Another independent theoretical argument considering the running of the quartic self coupling provides a similar upper limit. The variation of the coupling with the energy scale E is described by the Renormalisation Group Equation. Considering only one loop corrections the solution to this equation is [40],

$$\lambda(E) = \lambda(v)\left(1 - \frac{3\lambda(v)}{4\pi^2}\log\left(\frac{E}{v}\right)\right) \tag{4.25}$$

where the electroweak symmetry breaking scale v has been chosen as the natural reference energy point. At energies much larger than the electroweak symmetry breaking scale $E \gg v$, the quartic coupling grows and eventually becomes infinite at a point called the Landau pole, at the energy scale,

$$E = v\exp\left(\frac{4\pi^2}{3\lambda(v)}\right) \tag{4.26}$$

From the relationship between the coupling λ and m_H, as shown in Equation 4.23, it is possible to establish the energy domain in which the Standard Model is still valid, i.e. the energy cut off below which the coupling remains finite. The above expression can then be turned into a limit on m_H. At an energy scale of 10^{16} GeV one would require a light Higgs boson below about 200 GeV [40]. At an energy scale of 1 TeV the Higgs boson mass would be approximately 1 TeV [40].

4.3 The Standard Model Higgs Boson at the LHC

For any given value of m_H, the Standard Model Higgs boson production cross sections and the decay rates in different channels can be calculated. The mechanisms for

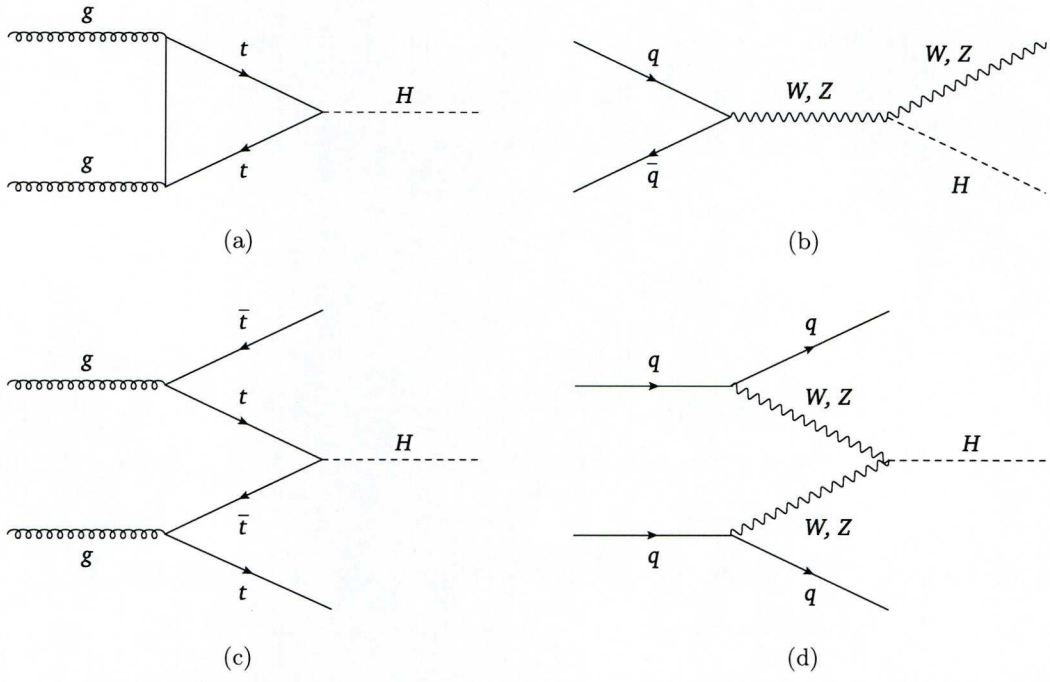

Figure 4.3: The dominant processes in the production of the Standard Model Higgs boson at the LHC: (a) gluon-gluon fusion, (b) associated vector boson production, (c) associated $t\bar{t}$ production and (d) vector boson fusion.

Standard Model Higgs boson production in proton-proton collisions at the LHC and a number of the most important decay channels are described below for a broad range of possible masses.

4.3.1 Production Mechanisms

The dominant processes in Standard Model Higgs boson production at the LHC are shown in Figure 4.3 and their cross sections as a function of m_H are shown in Figure 4.4. Across the full range of masses considered, the dominant production mechanism at the LHC is gluon-gluon fusion which proceeds almost exclusively via a top quark loop. The second largest production cross section at the LHC is that of vector boson fusion. The cross sections for Standard Model Higgs boson production in association with $t\bar{t}$ pairs or vector bosons (Higgstrahlung) are much smaller. However, although they have lower cross sections, both the vector boson fusion process and the associated production mechanisms provide specific signatures that can be exploited in the triggering and identification of candidate events. This is particularly significant for decay channels in which some additional handle is required in the final state in order to distinguish

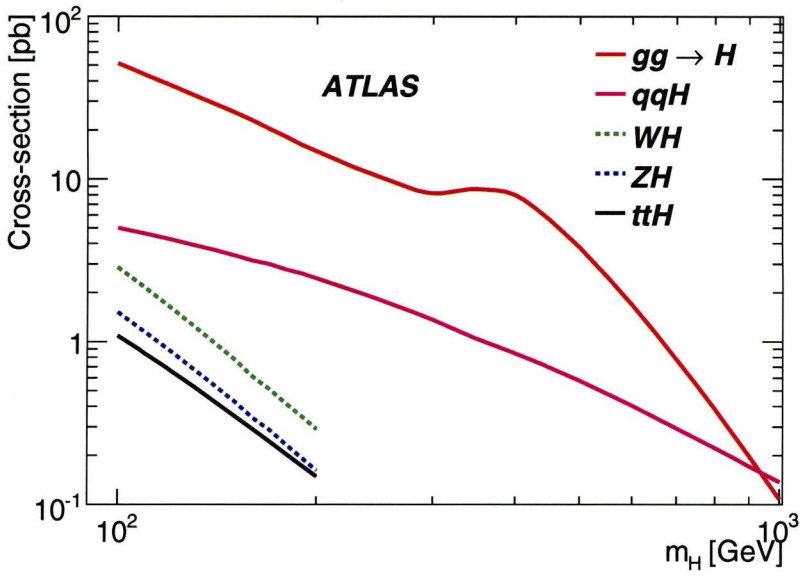

Figure 4.4: *The cross sections for Standard Model Higgs boson production at the LHC as a function of m_H, at $\sqrt{s} = 14$ TeV [41].*

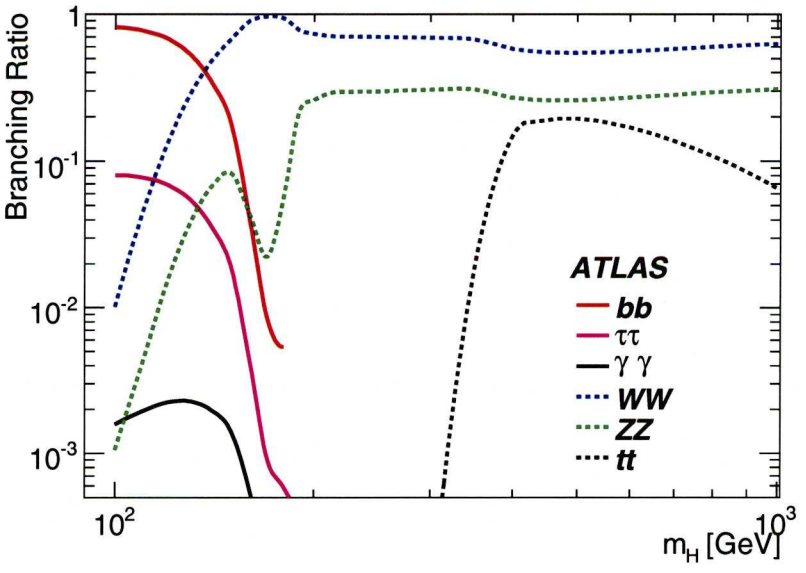

Figure 4.5: *The branching ratios for the most important Standard Model Higgs boson decay channels as a function of m_H [41].*

the signal events from the large numbers of background events expected from QCD processes.

4.3.2 Decay Channels

The branching ratios for a number of Standard Model Higgs boson decay channels as a function of m_H are shown in Figure 4.5. For $m_H < 140$ GeV, decays to fermion anti-fermion pairs dominate and for $m_H > 140$ GeV, decays into two vector bosons dominate. A summary of the most promising search channels considered in the ATLAS experiment are discussed below.

$H \rightarrow b\bar{b}$

In the low mass region, $m_H < 140$ GeV, the $H \rightarrow b\bar{b}$ has the largest branching ratio since the b quarks are the most massive fermions that are kinematically accesible in this region. Due to the large backgrounds from QCD processes, the channel is only considered in the context of associated production. The fully hadronic final state has the largest branching ratio but such events are difficult to trigger on and distinguish from the large number of background events.

$H \rightarrow \gamma\gamma$

Another important channel in the low mass region is the $H \rightarrow \gamma\gamma$ channel which proceeds through a heavy quark loop. This process has a very small branching ratio, spanning the region $110 < m_H < 140$ GeV. Nevertheless, the events have a clear signature and thus provide one of the most promising channels in the low mass region. Inclusive searches and searches in association high p_T jets are currently being considered.

$H \rightarrow \tau^+\tau^-$

In addition, there is significant potential for discovery in the mass range $m_H < 130$ GeV from the $H \rightarrow \tau^+\tau^-$ channel in association with high p_{T} jets. Due to the large backgrounds from QCD processes only the fully leptonic and semi-leptonic final states are considered in this channel. Feasibility studies have also been performed for the fully hadronic final state but as with the fully hadronic final state in the $H \rightarrow b\bar{b}$ channel, it is difficult to trigger on such events and distinguish them from the large number of background events.

$H \rightarrow ZZ^{(*)}$

In the high mass range, the $H \rightarrow ZZ^{(*)}$ channel provides one of the most promising channels since the fully leptonic (e, μ) final state provide one of the cleanest experimental signatures. The channel is sensitive over a broad range of masses with the most challenging region being 120 - 150 GeV, where one of the Z bosons is produced off-shell. Similarly, there is a dip in sensitivity at 160 GeV where the branching ratio for $H \rightarrow ZZ^*$ decays is suppressed due to the opening of the phase space for the decay into two on-shell W bosons. To complement the e and μ decay modes, the $l^+l^-\nu\overline{\nu}$ and $l^+l^-b\overline{b}$ final states are now also being considered.

$H \rightarrow W^+W^-$

Another important channel in the high mass range is the $H \rightarrow W^+W^-$ channel. It has a larger branching ratio than the $H \rightarrow ZZ^{(*)}$ channel but the presence of neutrinos in the final state means that the events cannot be fully reconstructed and no signal resonance is observed. The signal in the $H \rightarrow W^+W^-$ channel is therefore identified as an excess of events and thus knowledge of the total background is crucial. Three decay modes are currently being considered in this channel: the fully leptonic final state in association with 0 jets, the fully leptonic final state in association with 2 jets and the semi leptonic final state in association with 2 jets.

4.4 ATLAS Sensitivity to the Standard Model Higgs Boson

Searches for the Standard Model Higgs boson in the ATLAS experiment will combine information from a number of statistically independent decay channels to provide a single measure of the significance of a discovery or an exclusion limit. Four of the most promising decay channels described above have been used to determine the combined sensitivity of the ATLAS detector to a Standard Model Higgs boson across a broad range of possible values of m_H. The expected discovery significances as a function of m_H, for an integrated luminosity of 10 fb^{-1} at $\sqrt{s} = 14$ TeV are shown in Figure 4.6. The expected discovery significance as a function of both m_H and the integrated luminosity at $\sqrt{s} = 14$ TeV are shown in Figure 4.7.

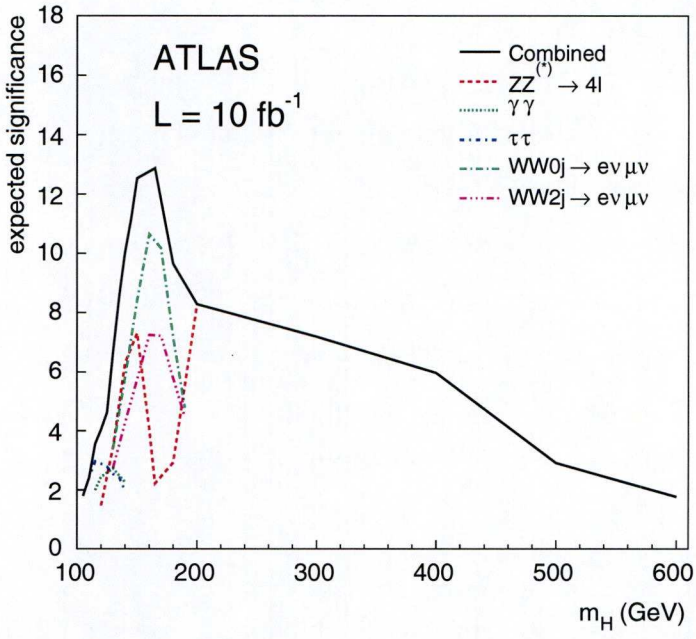

Figure 4.6: *The expected discovery significances in various decay channels as a function of m_H for an integrated luminosity of 10* fb^{-1} *at* $\sqrt{s} = 14$ TeV *[41].*

With an integrated luminosity of 2 fb^{-1}, the expected sensitivity of the ATLAS detector to the discovery of the Standard Model Higgs boson is at the 5σ level or greater in the mass range $143 < m_H < 179$ GeV [41]. With an integrated luminosity of 10 fb^{-1}, the expected sensitivity of the ATLAS detector to the discovery of the Standard Model Higgs boson is at the 5σ level or greater in the mass range $130 < m_H < 430$ GeV [41]. The sharp increase in the required luminosity at low m_H reflects the fact that the decay channels considered are less sensitive to a Standard Model Higgs boson in this mass region. Further improvements in the analyses of these decay channels, as well as the introduction of additional channels such as $t\bar{t}H$; W, H and Z, H production with $H \rightarrow b\bar{b}$ will increase the sensitivity in this region.

With first data, searches for the Standard Model Higgs boson in the ATLAS experiment will be primarily aimed at determining exclusion limits at the 95% confidence level. The expected exclusion limits for an integrated luminosity of 2 fb^{-1} at $\sqrt{s} = 14$ TeV are shown in Figure 4.8 and the exclusion limit as a function of both m_H and the integrated luminosity are shown in Figure 4.9. With an integrated luminosity of 2 fb^{-1}, the ATLAS detector has the expected combined sensitivity to exclude the

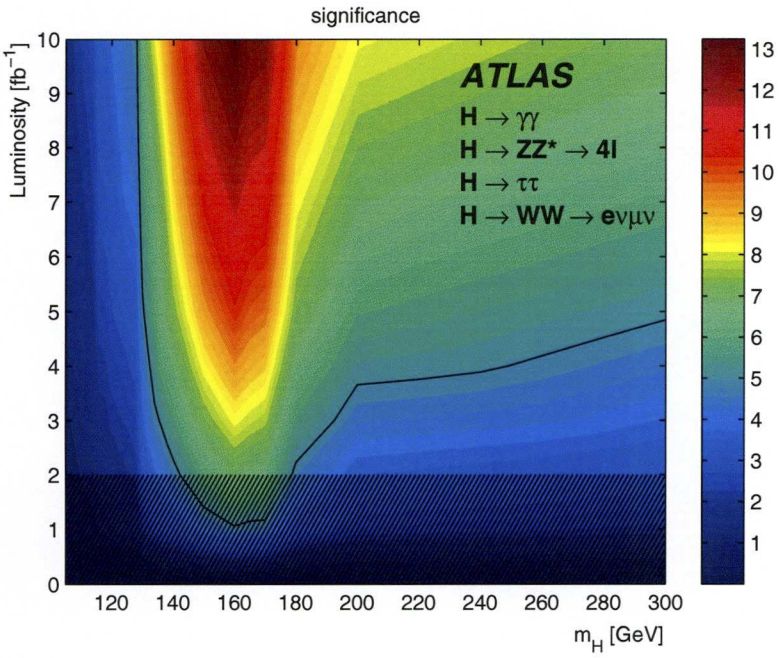

Figure 4.7: *The expected discovery significance contours for various integrated luminosities as a function of* m_H *at* $\sqrt{s} = 14$ TeV. *Here the black line represents the* 5σ *discovery contour. The shaded area marks the region in which the statistical combination procedure is no longer accurate, although estimates are still expected to be conservative [41].*

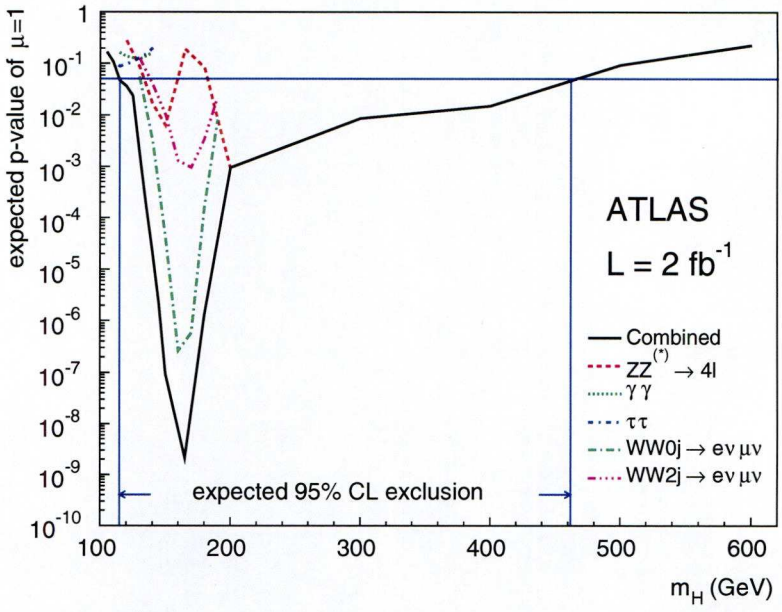

Figure 4.8: *The expected exclusion limits as a function of the m_H mass for an integrated luminosity of 2* fb^{-1} *at* $\sqrt{s} = 14$ TeV *[41].*

Standard Model Higgs boson in the mass range $115 > m_H > 460$ GeV at 95% CL [41].

The decay channels considered in the determination of the combined sensitivity are by no means comprehensive. In particular, only the electron and muon final states of the $H \rightarrow W^+W^-$ and $H \rightarrow ZZ^{(*)}$ channels are considered and it is expected that the inclusion of additional decay modes will further increase the sensitivity. In addition, a further increase in the sensitivity can be achieved through the combination of the results from both the ATLAS experiment and the CMS experiment.

From the relative sensitivites of decay channels considered, it is clear that the $H \rightarrow ZZ^{(*)} \rightarrow 4l$ $(l = e, \mu)$ channel will play a key role in the discovery or exclusion of the Standard Model Higgs boson, in particular in the mass range $m_H > 200$ GeV.

The latest LHC schedule suggests that the operations at $\sqrt{s} = 7$ TeV will continue at least until the end of 2011 [42], before the centre of mass energy is increased again towards the design value of 14 TeV. However, at $\sqrt{s} = 7$ TeV the cross section for Standard Model Higgs boson production falls significantly across the full range of possible m_H values, as shown in Figure 4.10. In addition, the cross sections for background processes will also vary. At the reduced centre-of-mass energy of 7 TeV, the ATLAS

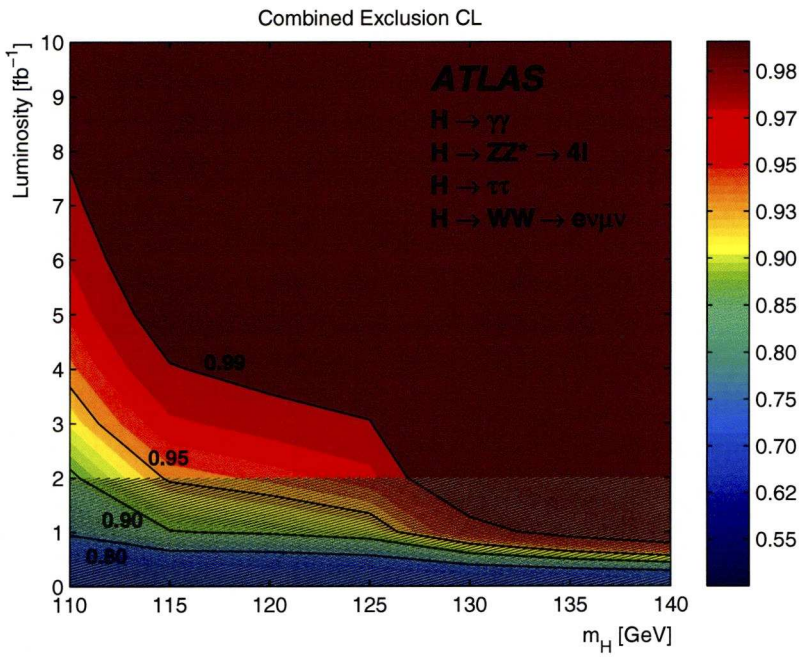

Figure 4.9: *The expected exclusion limit contours for various integrated luminosities as a function of* m_H *at* $\sqrt{s} = 14$ TeV. *Here the shaded area marks the region in which the statistical combination procedure is no longer accurate, although estimates are still expected to be conservative [41].*

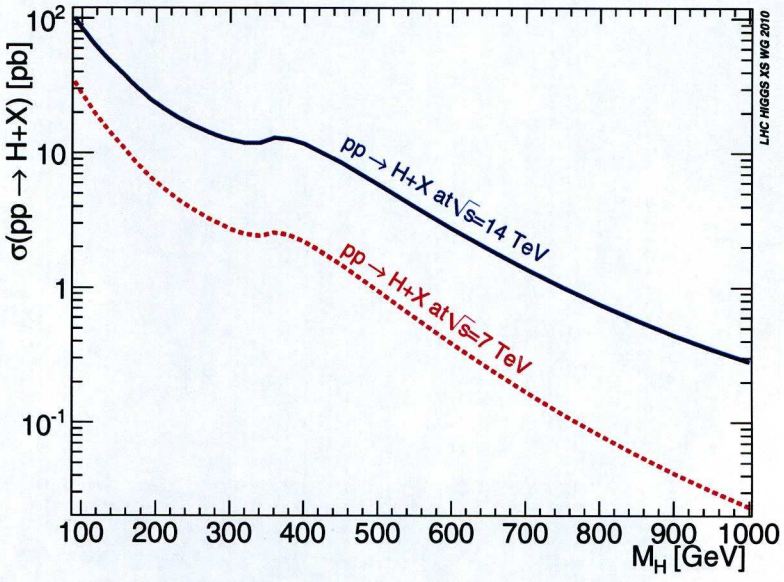

Figure 4.10: *The total cross section for Standard Model Higgs boson production at the LHC, at* $\sqrt{s} = 7$ *TeV and 14 TeV* [43].

experiment will therefore be more concerned with determining exclusion limits rather than determining discovery significances.

Chapter 5

Muon Identification and Reconstruction

Muon identification and reconstruction in the ATLAS experiment exploits the fact that muons leave signatures in all three of the major sub-detectors. The identification of muon candidates primarily begins with the reconstruction of tracks in the muon spectrometer, with supporting information coming from tracks reconstructed in the inner detector. Each of the two track collections provide independent measurements of the origin, direction and momentum of the muon candidates. The calorimeters situated between the two tracking detectors effectively behave as a muon filter, absorbing hadronic activity and ensuring high purity in the muon spectrometer for muons with $p_{\mathrm{T}} > 3$ GeV [41]. However, such muons will have traversed over 100 radiation lengths [41] before reaching the muon spectrometer and so multiple Coulomb scattering and upstream energy losses must be taken into account. As such, the measurements of the energy deposition in the calorimeters can therefore be used to correct the momentum measurements made in the muon spectrometer.

In order to achieve the physics potential of the ATLAS experiment the muon identification and reconstruction procedures must be accurate and robust for a broad spectrum of physics processes, in which the muon momenta can range from a few GeV to the TeV scale. The expected p_{T} and η distributions of the final state muons in $H \rightarrow ZZ^* \rightarrow 4\mu$ events with $m_H = 130$ GeV are shown in Figure 5.1.

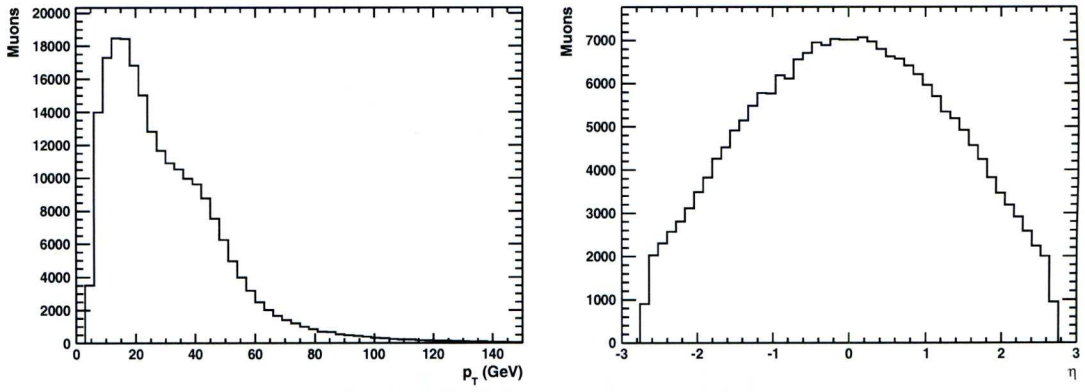

Figure 5.1: *The p_T (left) and η (right) distributions for the final state muons in 60,000 $H \rightarrow ZZ^* \rightarrow 4\mu$ events with $m_H = 130$ GeV at generator level. The muons are required to have $p_T > 5$ GeV and $|\eta| < 2.7$.*

5.1 Muon Identification

The strategies for identifying muons in the ATLAS detector are based on the different ways in which the muon signatures measured in each of the sub-detectors can be combined. The muons can therefore be classified into four exclusive and complementary categories [41] according to how each of the sub-detectors contributed to their identification. These four muon categories are described below.

5.1.1 Combined Muons

Muons that are identified by a muon spectrometer track that can be matched to an inner detector track are referred to as combined muons and can be represented by a single combined muon track. The purpose of combining the two tracks is to be able to identify muons at their production vertex with optimal parameter resolution. In addition, combined reconstruction also allows for the identification of muons inside jets and the rejection of muons from the secondary interactions and the pion and kaon decays that constitute a background in most physics analyses.

5.1.2 Tagged Muons

Muons that cannot be identified by a full muon spectrometer track can still be identified by matching inner detector tracks to muon spectrometer track segments. In this instance the muon spectrometer activity is only used for the purpose of tagging and

therefore the kinematics of the reconstructed muons are evaluated from the inner detector tracks alone. These particular tagged muons are referred to as low-p_{T} muons although they are not exclusively of low p_{T}. There are regions within the muon spectrometer, at $\eta = 0$ and $\eta = 1.2$ and at ϕ = -0.9 and ϕ -2.2, in which the geometrical acceptance is significantly reduced due to the presence of service passages or structural features, as shown in Figure 5.2 and Figure 5.3, respectively. The identification of low-p_{T} muons allows for the recovery of muons passing through these regions where the reconstruction of full muon spectrometer tracks is not possible.

In addition to tagging inner detector tracks with muon spectrometer track segments, the inner detector tracks can also be tagged with energy deposits in the calorimeters that are consistent with a muon's minimally ionising signature. This allows for the additional recovery of those muons that do not provide any muon spectrometer activity at all, either due to the reduced geometrical acceptance of the muon spectrometer or the fact that they are of too low a p_{T} to exit the calorimeters. These calorimeter tagged muons are not currently included in the standard muon identification procedures and are expected to have a greater muon fake rate that of the other identification strategies. As such, these muons will not be considered any further.

5.1.3 Standalone Muons

Muons that are identified by a muon spectrometer track that cannot be matched to an inner detector track are referred to as standalone muons. Since the muon spectrometer has an extended geometrical acceptance with respect to the inner detector most standalone muons are reconstructed in the region $2.5 < |\eta| < 2.7$, where the identification of combined muons and low-p_{T} muons is not possible. Although the inclusion of standalone muons can increase the muon identification efficiency by supplementing the combined muons and the low-p_{T} muons it may come at the expense of a significant increase in the muon fake rate, especially in the presence of beam and cavern backgrounds.

5.2 Muon Reconstruction

The reconstruction of muons in the ATLAS detector is performed by two independent families of algorithms: the STACO family [44] and the MuID family [45]. Each has

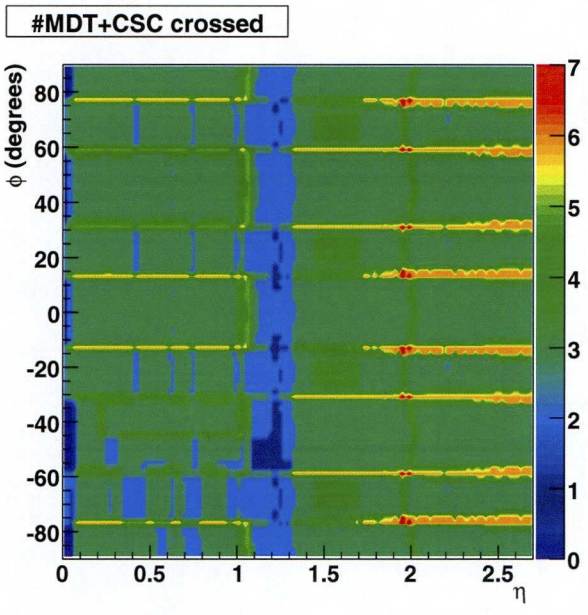

Figure 5.2: *The number of MDT + CSC layers traversed by muons as they pass through the muon spectrometer as a function of* $|\eta|$ *and* ϕ [41].

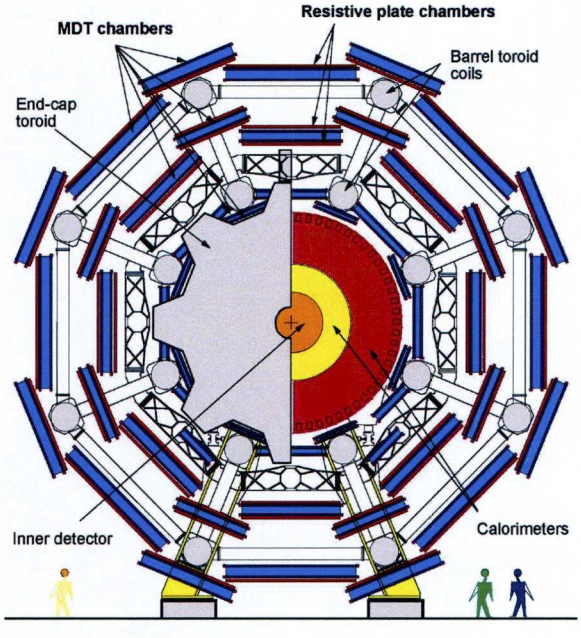

Figure 5.3: *A view of the* ATLAS *detector in the* $x - y$ *plane. The 16* ϕ *sectors of the muon spectrometer can be seen, each of which contains three stations of MDT chambers and RPCs. The structural feet of the detector can be seen at the bottom of the picture* [13].

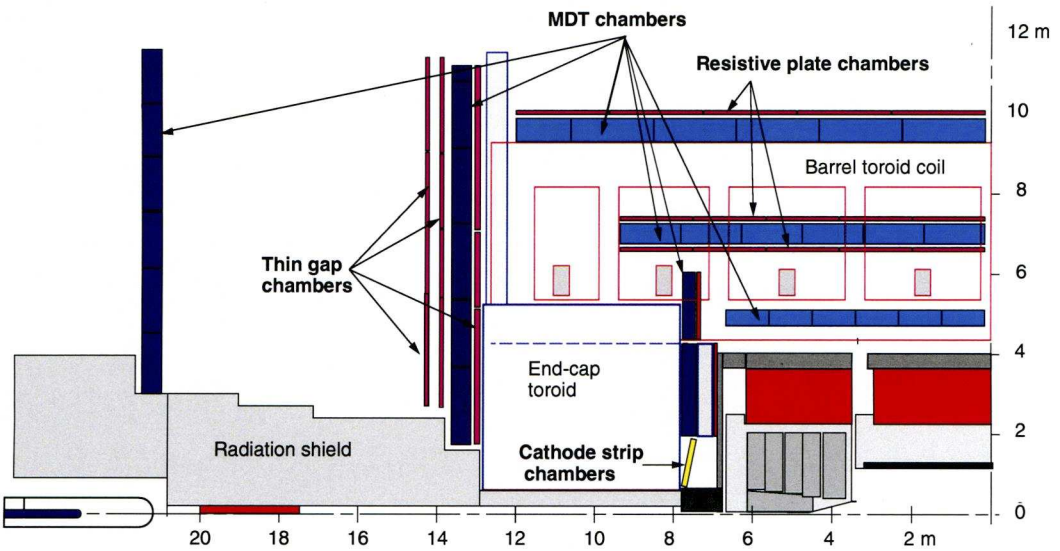

Figure 5.4: *A view of the* ATLAS *detector in the $x - y$ plane. The position of the endcap toroid magnet is indicated in the middle of the picture* [41].

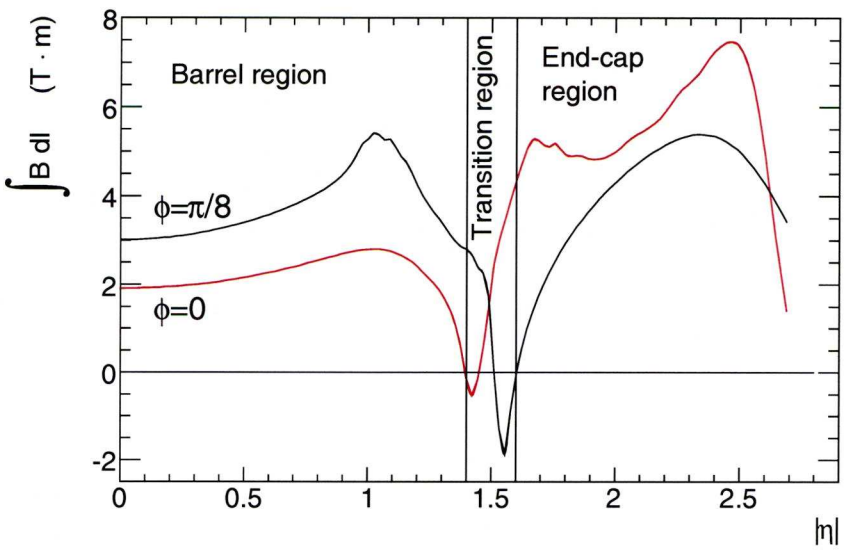

Figure 5.5: *The magnetic field integral experienced by muons originating from the interaction point and propagating in a straight line through the muon spectrometer as a function of* $|\eta|$ [41].

its own algorithms for reconstructing each of the aforementioned muon categories and takes its name from the name of the algorithm that is responsible for the reconstruction of combined muons. For each reconstructed event, the two different chains of algorithms therefore provide two independent muon collections with which users can perform their analyses. The top-level algorithms that comprise the two different reconstruction chains are described in the following sections. Where a muon can be reconstructed by two or more algorithms in the chain, only a single muon will appear in the muon collection under just one of the muon categories. More specifically, standalone muons that can be matched to an inner detector track are recorded as combined muons but not as standalone muons. When a standalone muon can be matched to more than one inner detector track, the combined muon with the best matching pair of tracks is flagged as the best match. In addition, when necessary a single combined muon can be created from a muon spectrometer tagged muon and a combined muon that share the same inner detector track.

At the present time the STACO muon collection has been chosed by the ATLAS collaboration to be the default muon collection for physics analyses; although it is intended that the muons from each family of algorithms will eventually be merged.

5.2.1 Inner Detector Tracks

The reconstruction of inner detector tracks is performed by a collection of tools and algorithms [46] primarily following an inside-out pattern recognition procedure. The search for track candidates is seeded by three dimensional space points in the silicon detectors, requiring at least three points with each being in a different silicon layer. For each seed a region is defined around the space points in which the algorithms search for additional hits that may be associated to the track candidate. The reconstruction follows the seed trajectory through this region and, accounting for multiple Coulomb scattering, includes successive hits in a track fit. The track information is progressively updated such that a prediction of the track representation on the next detector element can be made and thus the most likely extension of the track trajectory can be determined. The silicon seeded track search provides a very large number of track candidates that have to be resolved by a stringent ambiguity processor before they can be extended to the TRT. The track candidates are thefore ranked according to the probability that they describe the trajectory of particle from a physics event. This

ranking is based on a so-called track scoring strategy that considers multiple measures of track quality [47]. Only those track candidates that satisfy the track scoring system are retained and used to find compatible TRT track segments. Once identified, the compatible TRT hits are then associated to the silicon tracks as track extensions. Each extended track is evaluated with respect to the silicon track by comparing the original track score to that after a refit of the extended track. In the case that the original score is higher the TRT hits are instead identified as associated outlier measurements.

The inside-out pattern recognition process relies on a track seed being found in the silicon layers and, as such, not all inner detector tracks can be identfied by this method. For instance tracks from secondary displaced decay vertices or from photon conversions may have insufficient silicon hits to constitute a seed. A second track reconstruction sequence is therefore performed following an outside-in pattern recognition procedure that is designed to complement the initial inside-out procedure and optimise the re-contruction efficiency. Those track segments in the TRT that have been missed in the initial inside-out reconstruction are identified and extrapolated back into the silicon detectors in order to associate them with silicon track segments that may also have been missed. The resulting collection of inner detector tracks serves as input to the reconstruction of combined muons and low-p_{T} muons.

5.2.2 Muon Spectrometer Tracks

The reconstruction of tracks in the muon spectrometer begins by identifying regions of activity, which are defined by the presence of hits in the trigger chambers. Pattern recognition algorithms then reconstruct straight line track segments in the stations corresponding to these regions of interest. Candidate tracks are subsequently reconstructed by the Muonboy [44] (STACO) and MOORE [48] (MuID) algorithms which perform a global track fit to track segments in three different muon stations, taking into account the magnetic field strength in the muon spectrometer volume. The track parameters are then determined at the inner station of the muon spectrometer before the track is extrapolated back to the beam line such that the track parameters can also be determined at the interaction point. The extrapolation requires an accurate knowledge of the amount of material traversed in order to account for multiple Coulomb scattering and energy losses upstream of the muon spectrometer. The Muonboy algorithm performs this extrapolation to the beam line itself whereas the MuID reconstruction

chain employs an additional algorithm, MuID-Standalone [45], to extrapolate the muon spectrometer tracks reconstructed by the MOORE algorithm. Another important difference between the two reconstruction chains is in the treatment of the energy loss upstream of the muon spectrometer. Both algorithms account for these energy losses through an energy loss parameterisation and knowledge of how much material the track trajectory has traversed. However, by default the MOORE algorithm will also make use of the calorimeter measurements if they are observed to be significantly higher than the expected energy loss and if the muon appears to be isolated. The resulting collections of Muonboy and MOORE extrapolated muon spectrometer tracks form the basis upon which the standalone muons are reconstructed and serve as input to the reconstruction of combined muons.

5.2.3 Combined Muon Tracks

The aforementioned inner detector tracks and extrapolated muon spectrometer tracks are matched and combined by the STACO and MuID algorithms to reconstruct combined muon tracks. For both algorithms the matching of the tracks is based on the calculated match chi-square (χ^2_{match}), defined as the difference between the two track vectors weighted by their combined covariance matrix [41]:

$$\chi^2_{match} = (\mathbf{T}_{MS} - \mathbf{T}_{ID})^T (\mathbf{C}_{ID} + \mathbf{C}_{MS})^{-1} (\mathbf{T}_{MS} - \mathbf{T}_{ID}). \tag{5.1}$$

Here $\mathbf{T}$ denotes a vector of five track parameters[8] expressed at the point of closest approach to the beam line and $\mathbf{C}$ denotes its corresponding covariance matrix. The match chi-square distributions for the combined muons from the two reconstruction chains are shown in Figure 5.6. If the match chi-square is less than some configurable threshold value the tracks are considered to be matched and the extrapolated muon spectrometer track is no longer considered in the search for further possible combinations. This ensures that by construction the resulting track collection will not contain any combined muon tracks that share an extrapolated muon spectrometer track.

The main difference between the two reconstruction chains is the manner in which they combine the matching pairs of inner detector and muon spectrometer tracks to

[8]The parameterisation of a charged particle track in a magnetic field with respect to a given surface requires a minimal set of five parameters.

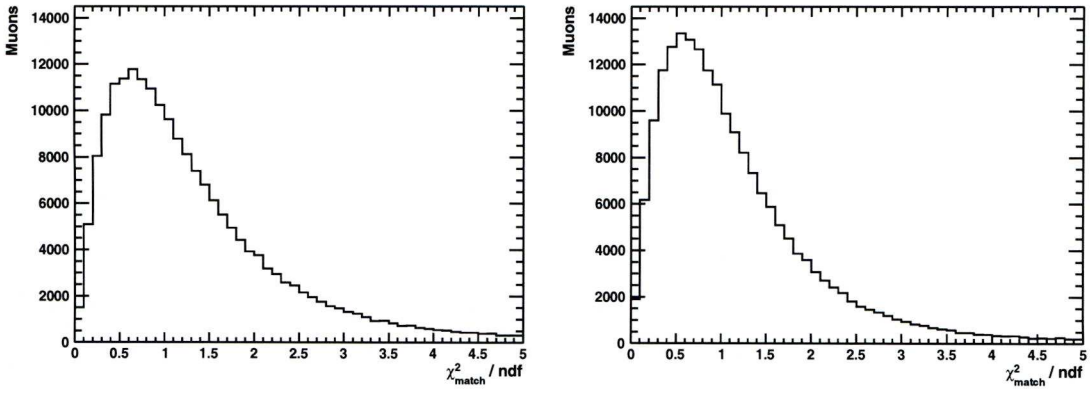

Figure 5.6: *The match chi-square distributions for the combined muons in 60,000 $H \rightarrow ZZ^* \rightarrow 4\mu$ events with $m_H = 130$* GeV *from the* STACO *(left) and* MuID *(right) muon collections. The muons are required to have $p_T > 5$ GeV and $|\eta| < 2.7$ at the generator level.*

form a single combined muon track. The STACO algorithm performs a statistical combination of the two independently reconstructed track parameters and their covariance matrices to obtain a combined muon track parameter vector **T** given by [41]:

$$\mathbf{T} = (\mathbf{C}_{ID}^{-1} + \mathbf{C}_{MS}^{-1})^{-1}(\mathbf{C}_{ID}^{-1}\,\mathbf{T}_{ID} + \mathbf{C}_{MS}^{-1}\,\mathbf{T}_{MS}). \tag{5.2}$$

The MuID algorithm performs a partial refit of the two matched tracks, taking the reconstructed inner detector tracks and incorporating the additional hits from the muon spectrometer, re-calculating the effects of multiple Coulomb scattering and energy loss in the material traversed by the track.

5.2.4 Tagged Inner Detector Tracks

The tagging of inner detector tracks with muon spectrometer track segments is performed by the MuTag [44] (STACO) and the MuGirl [49] (MuID) algorithms. These algorithms extrapolate inner detector tracks to the inner station of the muon spectrometer where they search for a corresponding muon spectrometer track segment. Both algorithms are currently being developed to allow the extrapolation of inner detector tracks to multiple muon spectrometer stations and the possibility of including the associated track segments in a refitting of the track. The MuTag algorithm identities muon candidates based on a tagging chi-square determined from the differences between the

muon spectrometer track segments and the predictions from the extrapolation of the inner detector tracks. The MuGirl algorithm identifies muon candidates by employing an artificial neural network to define a discriminant. In either case, if the track segment is determined to be sufficiently close to the predicted position then the inner detector track is tagged as a muon candidate. There is an additional important difference in the way in which these tagging algorithms operate within the two different reconstruction chains. The MuGirl algorithm considers all inner detector tracks whereas the MuTag algorithm only considers those inner detector tracks that have not already been used in the reconstruction of a combined muon track. In this respect the MuGirl algorithm has the ability to operate as a standalone muon reconstruction algorithm whilst the MuTag algorithm serves only to supplement the STACO algorithm.

5.3 Muon Identification and Reconstruction Performance

The performance of the STACO and MuID reconstruction chains, in terms of the identification efficiency, the $1/p_{\mathrm{T}}$ scale and the fractional $1/p_{\mathrm{T}}$ resolution has been determined using 60,000 $H \rightarrow ZZ^* \rightarrow 4\mu$ events with $m_H = 130$ GeV, in which the muons are required to have $p_{\mathrm{T}} > 5$ GeV and $|\eta| < 2.7$[9].

For each event the reconstructed muon best matching each generator level muon in $\eta - \phi$ space is found. The ΔR distributions of the best matching pairs from each of the two muon collections are shown in Figure 5.7. If a pair satisfies $\Delta R < 0.005$ then the reconstructed muon and the generator level muon are considered to be matched. The identification efficiency is then defined as the fraction of generator level muons that could be sucessfully matched to a reconstructed muon. The $1/p_{\mathrm{T}}$ scale and the fractional $1/p_{\mathrm{T}}$ resolution are defined as the mean and the standard deviation of a gaussian fit to the distribution [41]:

$$\Delta(1/p_{\mathrm{T}})\ p_{\mathrm{T}} = ((1/p_{\mathrm{T}\,reco}) \ - \ (1/p_{\mathrm{T}\,true})) \ / \ (1/p_{\mathrm{T}\,true}), \tag{5.3}$$

where $p_{\mathrm{T}\,reco}$ and $p_{\mathrm{T}\,true}$ are the p_{T} of the reconstructed muon and the generator level muon in each of the successfully matched muon pairs, respectively. In evaluating the

[9] In these events approximatelty 95% of the muons in the two muon collections are combined muons, with approximately equal numbers of low-pt muons and standalone muons making up the remainder.

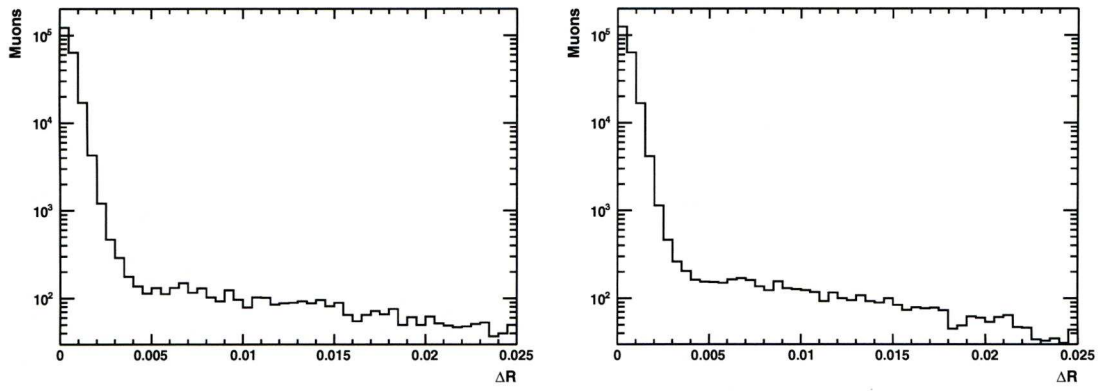

Figure 5.7: *The ΔR distributions for the best matching reconstructed muons in 60,000 $H \rightarrow ZZ^* \rightarrow 4\mu$ events with m_H = 130* GeV *from the STACO (left) and MuID (right) muon collections. The muons are required to have $p_T > 5$* GeV *and $|\eta| < 2.7$ at the generator level.*

$1/p_T$ scale and the fractional $1/p_T$ resolution only combined muons are considered since they each have an associated inner detector track, muon spectrometer track and combined muon track for which the reconstruction performance can be determined.

The muon identification and reconstruction performance presented in this section is based solely on simulated $H \rightarrow ZZ^* \rightarrow 4\mu$ events with $m_H = 130$ GeV[10]. The performance will ultimately be determined from data and additional factors such as event pileup and cavern backgrounds will need to be considered.

5.3.1 Identification Efficiency

The identification efficiency is shown in Figure 5.8 as a function of p_T, η and ϕ and is ~95% when considering all muon categories. The efficiency for reconstructing combined muons dips at $\eta = 0$ and $\eta = 1.2$ and at ϕ = -0.9 and ϕ -2.2 due to the reduced geometrical acceptance of the muon spectrometer in these regions, as is shown in Figure 5.2, Figure 5.3 and Figure 5.4. The identification efficiency in these regions increases with the inclusion of low-p_T muons, which recover some of the muons that could not be reconstructed as combined muons. Similarly, the identification efficiency beyond $|\eta| = 2.5$ increases with the inclusion of standalone muons since this region is outside the geometrical acceptance of the inner detector where muons cannot be reconstructed

[10]Reconstructed with Athena software release 14.2.25.3

as combined muons or low-p_{T} muons.

5.3.2 $1/p_{\mathrm{T}}$ Scale

The $1/p_{\mathrm{T}}$ scales of the inner detector, extrapolated muon spectrometer and combined muon tracks are shown in Figure 5.9 as a function of p_{T}, η and ϕ. For all three of the muon tracks the $1/p_{\mathrm{T}}$ scale is within ~1% of the generator level $1/p_{\mathrm{T}}$. The inner detector tracks provide the best performance, for which the $1/p_{\mathrm{T}}$ scale shows only very little variation. At approximately ~100 GeV the $1/p_{\mathrm{T}}$ scale of the extrapolated muon spectrometer tracks becomes comparable with that of the inner detector tracks. Below ~100 GeV the $1/p_{\mathrm{T}}$ scale of the extrapolated muon tracks becomes increasingly over-estimated at lower p_{T}. However, even at the lowest p_{T}, the $1/p_{\mathrm{T}}$ scale is still within ~2% of the generator level $1/p_{\mathrm{T}}$. The extrapolated muon spectrometer tracks also show a slight shift in the $1/p_{\mathrm{T}}$ scale at ϕ =-0.9 and ϕ =-2.2, which is not observed for the inner detector tracks and can be attributed to the reduced geometrical acceptance of the muon spectrometer due to the structural supports of the detector as shown in Figure 5.3.

5.3.3 $1/p_{\mathrm{T}}$ Resolution

The fractional $1/p_{\mathrm{T}}$ resolutions of the inner detector, extrapolated muon spectrometer and combined muon tracks are shown in Figure 5.10. The combined muon tracks provide the best performance, with a fractional $1/p_{\mathrm{T}}$ resolution of 2-3% for muon tracks with $p_{\mathrm{T}} < 100$ GeV. The performance of the inner detector dominates that of the muon spectrometer up to ~100 GeV, at which point the fractional $1/p_{\mathrm{T}}$ resolution of the two tracks becomes comparable at a value of ~4%. The inner detector tracks show a gradual increase in the fractional $1/p_{\mathrm{T}}$ resolution as the p_{T} or $|\eta|$ of the muons increases. This can be attributed to the fact that at higher p_{T} the tracks become straighter while at higher $|\eta|$ they have a shorter lever arm, which in both cases makes the determination of the track curvature and thus the muon momentum more difficult. The muon spectrometer tracks show a significant degradation in the fractional $1/p_{\mathrm{T}}$ resolution at $|\eta|$ ~1.5. This is not only due to the reduced geometrical acceptance of the muon spectrometer, as shown in Figure 5.3 and Figure 5.4, but also the fact that there is a significant drop in the integrated magnetic field strength for muons in the transition region ($1.4 < |\eta| < 1.6$) between the barrel and the endcaps, as shown in Figure 5.5.

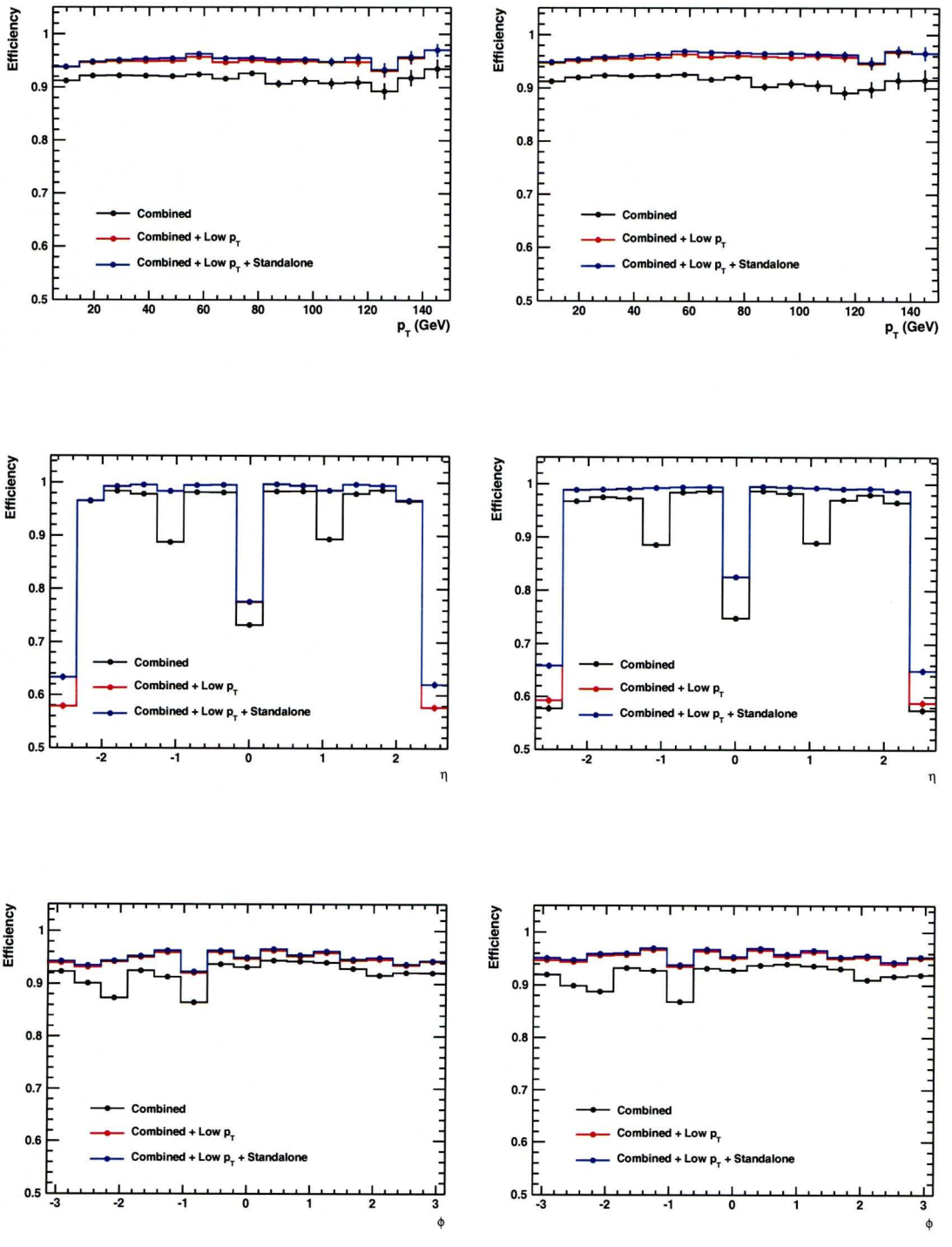

Figure 5.8: *The muon identification efficiencies for each of the three muon categories from the STACO (left) and MuID (right) muon collections as a function of* p_{T} *(top),* η *(middle) and* ϕ *(bottom). The muons are required to have* $p_{\mathrm{T}} > 5$ GeV *and* $|\eta| < 2.7$ *at the generator level.*

This degradation in the fractional $1/p_{\mathrm{T}}$ resolution can also be attributed to the fact that the muons pass through the material of the toroid magnets that are located in the endcap regions, as shown in Figure 5.4. Furthermore, the muon spectrometer tracks show an additional, smaller degradation in the fractional $1/p_{\mathrm{T}}$ resolution at ϕ =-0.9 and ϕ =-2.2 where the geometrical acceptance of the muon spectrometer is reduced due to the structural supports of the detector, as shown in Figure 5.3.

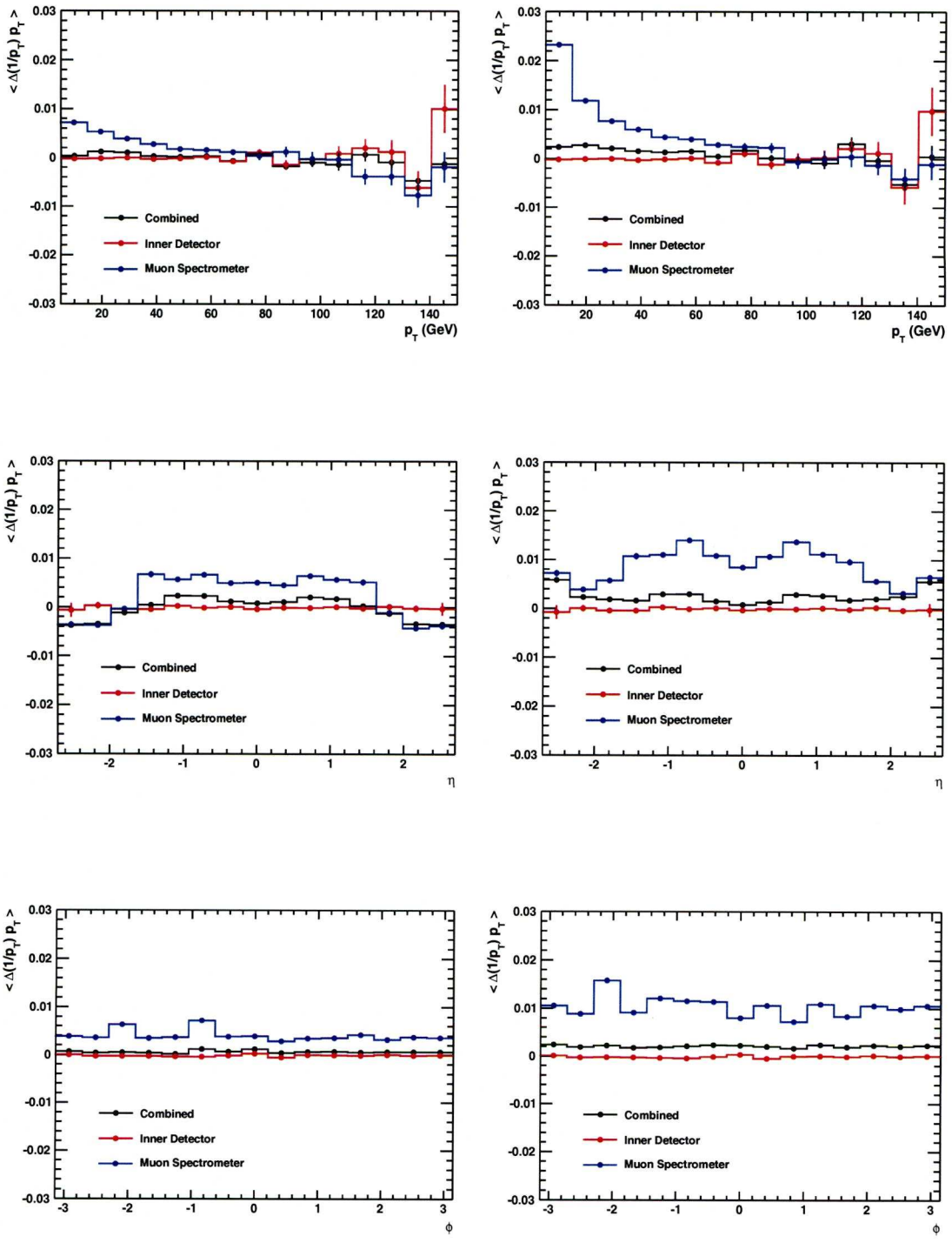

Figure 5.9: *The $1/p_{\mathrm{T}}$ scale for each of the three tracks of the combined muons from the STACO (left) and MuID (right) muon collections as a function of p_{T} (top), η (middle) and ϕ (bottom). The muons are required to have $p_{\mathrm{T}} > 5$ GeV and $|\eta| < 2.7$ at the generator level.*

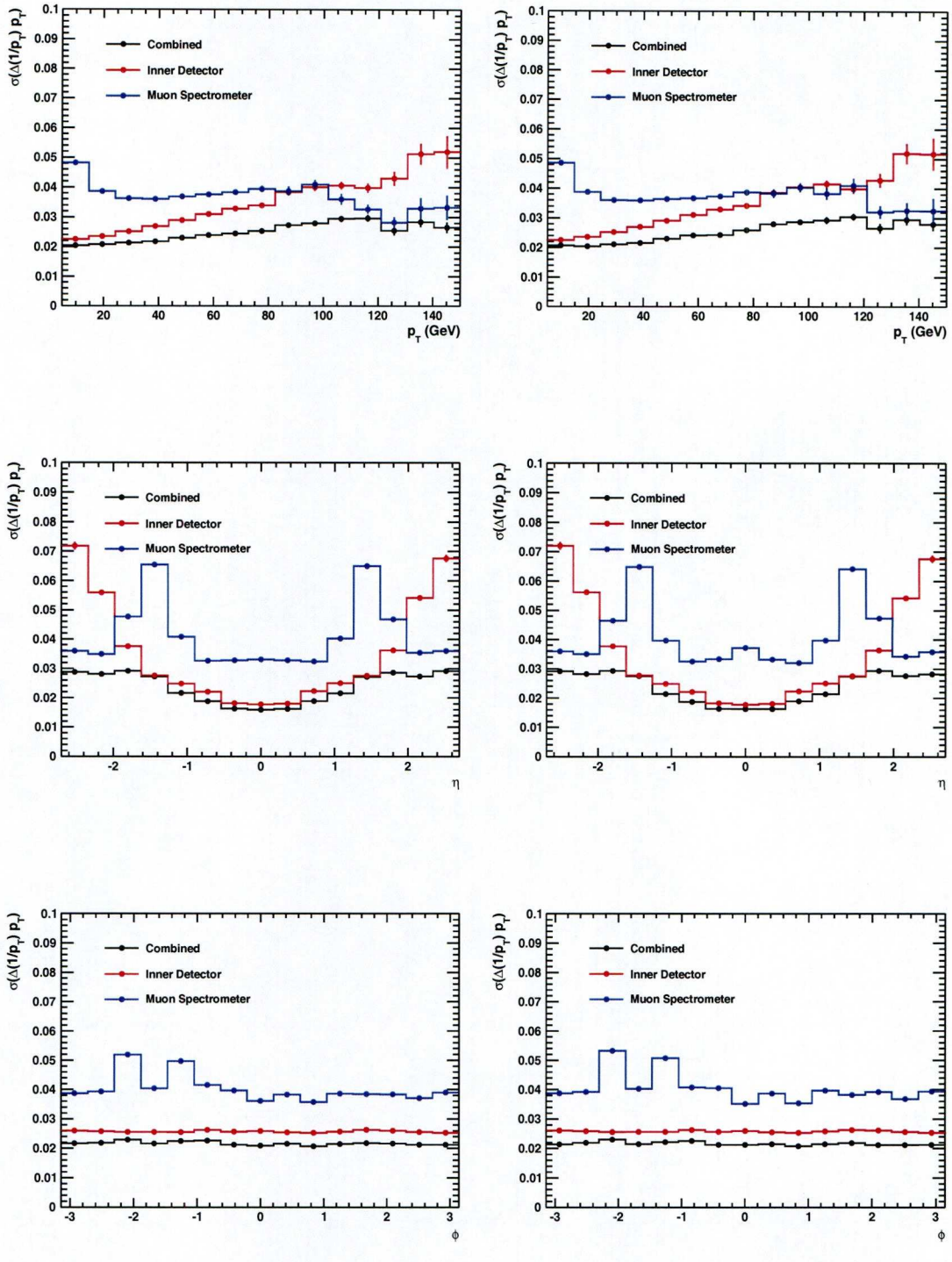

Figure 5.10: *The fractional $1/p_{\mathrm{T}}$ resolution for each of the three tracks of the combined muons from the STACO (left) and MuID (right) muon collections as a function of p_{T} (top), η (middle) and ϕ (bottom). The muons are required to have $p_{\mathrm{T}} > 5$ GeV and $|\eta| < 2.7$ at the generator level.*

Chapter 6

Sensitivity to $H \rightarrow ZZ^{(*)} \rightarrow 4\mu$ at $\sqrt{s} = 7$ TeV

As was shown in Chapter 4, the four lepton final state is expected to play a key role in the search for the Standard Model Higgs boson in the ATLAS experiment as it provides one of the cleanest experimental signatures. This is particularly true for the four muon final state as the high purity and excellent momentum resolution of the muons, as shown in Chapter 5, leads to a narrow invariant mass peak. There are however a number of background processes with similar four muon final state signatures. For a broad range of possible m_H values, the major component of this background is expected to consist of the $pp \rightarrow ZZ^{(*)}$ continuum. In the low mass region $m_H < 180$ GeV, where one of the Z bosons in the signal channel is off-shell, backgrounds from inclusive Z production and $pp \rightarrow t\bar{t}$ processes are also expected to contribute. The dominant background processes to the four muon final state are shown in Figure 6.1.

The analysis strategy for identifying Standard Model Higgs bosons in the four muon final state is described below[11]. The analysis mostly follows the baseline analysis strategy that was originally developed to determine the sensitivity of the ATLAS detector to a Standard Model Higgs boson in the four lepton final state at $\sqrt{s} = 14$ TeV [41], the results of which were shown in Chapter 4. Where the analysis deviates from this baseline selection, it shall be explicitly stated.

[11] Only the reconstructed muons from the STACO collection are considered in this analysis since this is currently the default muon collection in the ATLAS experiment [41].

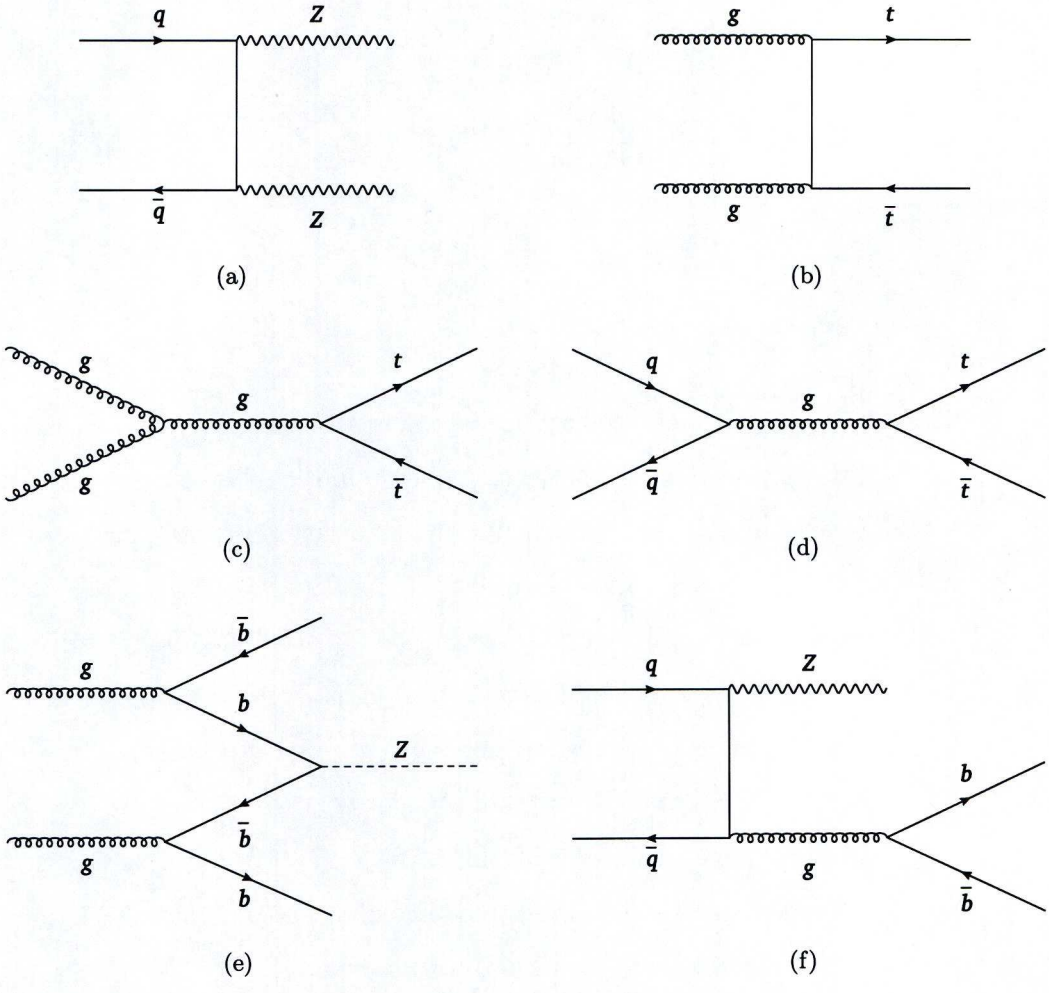

Figure 6.1: The dominant background processes to the production of the Standard Model Higgs boson in the four muon final state at the LHC: (a) $q\bar{q}\rightarrow ZZ$, (b) and (c) $gg\rightarrow t\bar{t}$, (d) $q\bar{q}\rightarrow t\bar{t}$, (e) $gg\rightarrow Zb\bar{b}$, (f) $q\bar{q}\rightarrow Zb\bar{b}$.

6.1 Monte Carlo Samples

The Monte Carlo samples used in this analysis include a full simulation of the ATLAS detector response to proton-proton collisions at $\sqrt{s} = 7$ TeV. Leading order (LO) cross sections have been scaled to next-to-leading order (NLO) and, where possible, to next-to-next-to-leading order (NNLO). It has been assumed that relevant differential distributions are not affected by the higher order corrections. The details of the samples considered, including the event generators and the scaling of the cross sections to higher orders are described below. A summary of the cross sections for each of the samples, including branching ratios and generator level filter efficiencies is given in Table 6.1, along with the number of events available and the corresponding integrated luminosities.

6.1.1 Signals

Samples of $H \rightarrow ZZ^{(*)} \rightarrow 4l$ events with m_H ranging from 130 GeV to 600 GeV have been considered, where $l = e, \mu$ for $m_H < 200$ GeV and $l = e, \mu, \tau$ for $m_H \geq 200$ GeV. All of these signal samples have been generated using the PYTHIA [50] event generator. The generator incorporates both the gluon-gluon fusion and the vector boson fusion production mechanisms, the cross sections for which have been scaled to NNLO and NLO estimates [51, 52], respectively.

6.1.2 Backgrounds

Samples of $ZZ^{(*)} \rightarrow 4l$ where $l = e, \mu, \tau$, inclusive $Z \rightarrow \mu^+\mu^-$ and $t\bar{t}$ background events have been considered in this analysis. In addition, dedicated samples of $Zb\bar{b}$ events were also considered in which the Z boson, decaying into two muons, is accompanied by a $b\bar{b}$ pair and p additional partons, where $p = 0, 1, 2$ or 3. These particular samples are discussed further in Section 6.4.

The $ZZ^{(*)} \rightarrow 4l$ sample has been generated using the PYTHIA [50] event generator and includes both on-shell and off-shell Z bosons or photons. The LO cross section is scaled to a NLO estimate by the application of K factors. These K factors [42] are dependent upon the invariant mass of the di-boson pair (m_{ZZ}) and range from 1.17 at $m_{ZZ} = 130$ GeV to 1.47 at $m_{ZZ} = 600$. In addition, an extra correction of +16% [53] has been applied to the scaled cross section to account for the contribution from the gluon induced quark box diagram which is not incorporated in either the generator or

		σ (fb)	Events	$\int$L (fb^{-1})
Signal Samples				
m_H (GeV)	130	2.780	99935	35948
	140	4.117	29995	7286
	150	4.273	29994	7019
	160	1.855	29991	16168
	170	0.915	29842	32614
	180	2.044	29991	14673
	190	6.228	29996	4816
	200	15.235	49937	3278
	300	8.444	49933	5913
	400	5.964	49982	8381
	500	2.535	49977	19714
	600	1.085	49981	46065
Background Samples				
$ZZ^{(*)} \rightarrow 4l$		75.03	99976	1332.48
$Z \rightarrow \mu^+\mu^-$		900405	4968412	5.55
$t\bar{t}$		156879	773167	8.86

Table 6.1: *The cross sections, the number of events available and the corresponding integrated luminosities for each of the signal and background samples considered in the analysis.*

the NLO cross section prediction.

The inclusive $Z \rightarrow \mu^+\mu^-$ sample has also been generated using the PYTHIA [50] event generator and includes the Drell-Yan γ component and the Z/γ interference term. The samples have been filtered at the generator level, requiring a minimum Z/γ mass of 60 GeV. The LO cross section for Z boson production is scaled to a NLO estimate [54] and includes the branching ratio [55].

The $t\bar{t}$ sample has been generated at NLO using the MC@NLO [56] event generator. The samples have been filtered at the generator level, requiring that at least one of the W bosons decays leptonically to produce a lepton (e, μ, τ) with $p_T > 1$ GeV. The filter therefore explicitly excludes events in which both W bosons decay hadronically. The NLO cross section is taken from [54] and branching ratios are from [55].

6.2 Triggering

The Monte Carlo samples used in this analysis include a full simulation of the trigger chain, with an appropriate trigger menu for the initial phase of LHC operation at an instantaneous luminosity of 10^{31} cm^{-2}s^{-1}. In this analysis, events will be required to pass the MU10 trigger, a single muon trigger with a p_T threshold of 10 GeV. The efficiency of the MU10 trigger in selecting $H \rightarrow ZZ^{(*)} \rightarrow 4\mu$ events both prior to, and after the application of the full offline event selection criteria are shown in Table 6.2. The MU10 trigger selects candidate $H \rightarrow ZZ^{(*)} \rightarrow 4\mu$ events with an efficiency $\geq 99.69\%$ for all of the signal samples considered. Previous studies [42] have shown that in case of a future need to prescale the single lepton triggers, it is still possible to maintain high triggering efficiencies when using double lepton triggers.

6.3 Event Selection

Following the online event selection, the offline event selection proceeds in three stages. First, events in which there are at least four muons present are preselected according to the basic kinematic properties and the categories of the reconstructed muons in the event. Following preselection, the invariant masses of the di-muon pairs in the event are subject to m_H dependent selection criteria, aimed at identifying the best four-muon combination and reconstructing a H boson candidate in the event. Finally, additional

m_H (GeV)	Trigger Efficiency (%)	
	Before Event Selection	After Event Selection
130	98.32	99.73
140	98.74	99.69
150	99.07	99.89
160	99.26	99.72
170	99.34	99.79
180	99.27	99.91
190	99.26	99.77
200	99.35	99.96
300	99.61	99.91
400	99.64	99.85
500	99.56	99.89
600	99.54	99.69

Table 6.2: *The efficiency of the MU10 trigger in selecting* $H \rightarrow ZZ^{(*)} \rightarrow 4\mu$ *events, both prior to and after the application of the offline event selection.*

constraints are applied to the four muons of the reconstructed H boson candidate in order to reject events from background processes.

6.3.1 Preselection

Event preselection initially requires that all muons must be either combined muons or low-pt muons and must have $p_{\mathrm{T}} > 5$ GeV and $|\eta| < 2.5$. If there are less than four such muons in the event, the event is rejected. The event is then required to have at least four muons with $p_{\mathrm{T}} > 7$ GeV, of which at least two must have $p_{\mathrm{T}} > 20$ GeV, that can be combined into at least two oppositely charged pairs. The events that satisfy this initial preselection stage are identified as $H \to ZZ^{(*)} \to 4\mu$ candidates.

6.3.2 Kinematic Reconstruction

In each candidate event, the leading muon pair is defined as the oppositely charged pair of muons whose invariant mass is closest to the Z boson mass (m_Z). The secondary muon pair is then defined as the muon pair from the remaining oppositely charged muon pairs that has the largest invariant mass. The invariant mass distributions for the leading di-muon pairs, the secondary di-muon pairs and all four muons in candidate $H \to ZZ^{(*)} \to 4\mu$ events with $m_H = 130$ GeV and $m_H = 300$ GeV are shown in Figure 6.2.

For $H \to ZZ^{(*)} \to 4\mu$ events with $m_H < 180$ GeV, where one of the Z bosons in the signal channel is off-shell, there is no resonance in the invariant mass distribution of the secondary di-muon pairs. The distinctive shape of the invariant mass distribution for the secondary di-muon pairs in $H \to ZZ^{(*)} \to 4\mu$ events with $m_H > 180$ GeV, is due to the fact that that the leading di-muon pair has already been removed from the possible combinations of di-muon pairs.

In each candidate event, the invariant masses of the leading di-muon pair and the secondary di-muon pair (m_{12} and m_{12}, respectively) in candidate events are then required to satisfy the m_H dependent invariant mass windows shown in Table 6.3 [42].

6.3.3 Background Rejection

Although the $ZZ^{(*)}$ process is expected to provide the largest contribution to the background for a broad range of m_H values, the similarity of the final state topology to that of the signal events means that the process is largely irreducible. The inclusive

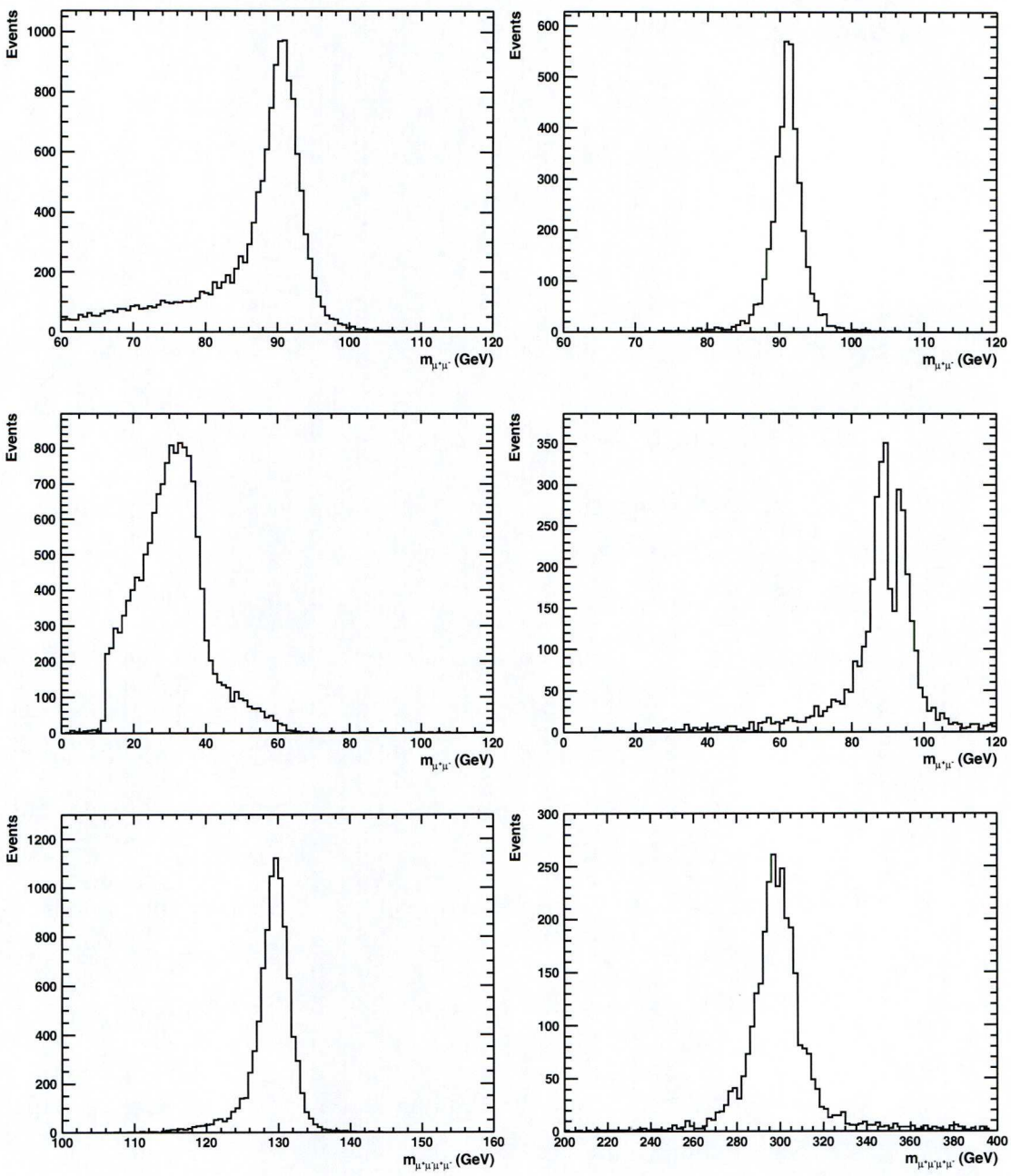

Figure 6.2: *The invariant mass distributions for the leading di-muon pairs (top), secondary di-muon pairs (middle) and all four muons (bottom) in candidate $H \to ZZ^{(*)} \to 4\mu$ events with $m_H = 130$ GeV (left) and $m_H = 300$ GeV (right).*

m_H (GeV)	$\lvert m_{12} - m_Z \rvert$ (GeV)	m_{34} (GeV)
130	$\pm$ 15	$>$ 20
140	$\pm$ 15	$>$ 25
150	$\pm$ 15	$>$ 30
160	$\pm$ 15	$>$ 30
170	$\pm$ 15	$>$ 35
180	$\pm$ 12	$>$ 40
190	$\pm$ 12	$>$ 50
200	$\pm$ 12	$>$ 60
300	$\pm$ 12	$\pm$ 15
400	$\pm$ 12	$\pm$ 15
500	$\pm$ 12	$\pm$ 15
600	$\pm$ 12	$\pm$ 15

Table 6.3: *The mass windows applied to the invariant mass of the leading di-muon pair (m_{12}) and the invariant mass of the secondary di-muon pair (m_{34}) in candidate $H \rightarrow ZZ^{(*)} \rightarrow 4\mu$ events. For 300* GeV *and above, the m_{34} invariant mass windows represent the limit on $\lvert m_{34} - m_Z \rvert$.*

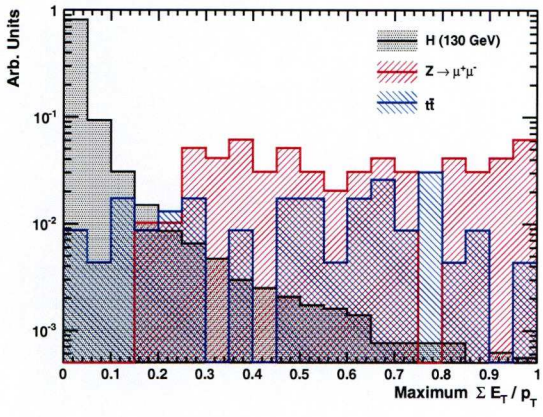

Figure 6.3: *The maximum normalised calorimetric isolation of the four selected muons in both signal and background events passing the preselection and kinematic reconstruction stages of the event selection. The histograms have been normalised to the number of events in each of the samples.*

$Z \rightarrow \mu^+\mu^-$ and $t\bar{t}$ processes, which are expected to contribute to the background in the lower mass regions, below 180 GeV, have much larger cross sections than that of the signal events, as shown in Table 6.1. Events from these background processes can be rejected by exploiting the fact that the muons from heavy quark decays are expected to be significantly less isolated than those from Z boson decays and originate from secondary displaced vertices. As a result, the four muons in candidate $H \rightarrow ZZ^{(*)} \rightarrow 4\mu$ events are subject to additional requirements based on both calorimeter and track isolation criteria and their impact parameter significance.

Calorimeter Isolation

The calorimeter isolation discriminant is determined from the sum of the transverse energies deposited in the calorimeter within a cone of radius $\Delta R = 0.2$ around the muon. The transverse energy deposited by the muon itself, along with any other calorimeter deposits within an inner cone of $\Delta R = 0.01$ around the muon, are rejected from the sum. The summed transverse energy deposited is normalised to the transverse momentum of the muon and the discriminant is defined as the least isolated of the four selected muons in the event. In this analysis, the summed, normalised transverse energy deposited is required to be less than 0.23. The calorimeter isolation of the least isolated muons in signal and background events passing the preselection stage of the event selection are

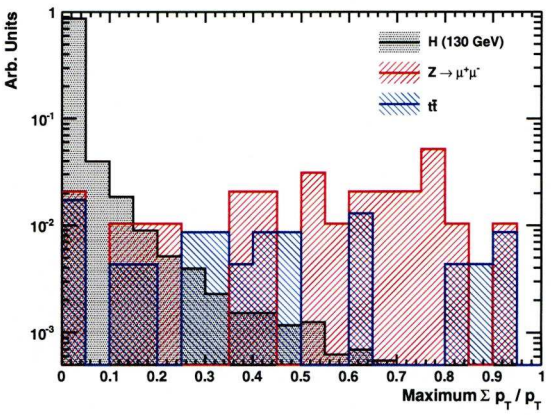

Figure 6.4: *The maximum normalised track isolation of the four selected muons in both signal and background events passing the preselection and kinematic reconstruction stages of the event selection. The histograms have been normalised to the number of events in each of the samples.*

shown in Figure 6.3.

Track Isolation

The track isolation discriminant is determined from the sum of the transverse momenta of the inner detector tracks within a cone of radius ΔR =0.2 around the muon. The tracks are requried to have at least one hit in the B-layer of the pixel detector and a minimum p_{T} of 1 GeV is imposed. The transverse momentum of the muon's inner detector track, along with that of any other inner detector track within a cone of ΔR =0.1 around the muon, is removed from the sum. The summed transverse momentum of the inner detector tracks is normalised to the transverse momentum of the muon's inner detector track and the discriminant is defined as the least isolated of the four selected muons in the event. In this analysis, the summed, normalised transverse momentum of the inner detector tracks is required to be less than 0.15. The track isolation of the least isolated muons in signal and background events passing the preselection stage of the event selection are shown in Figure 6.4.

Impact Parameter Signficance

In addition to the muon isolation criteria, a further rejection of background events can be achieved by considering the muon transverse impact parameter significance, defined

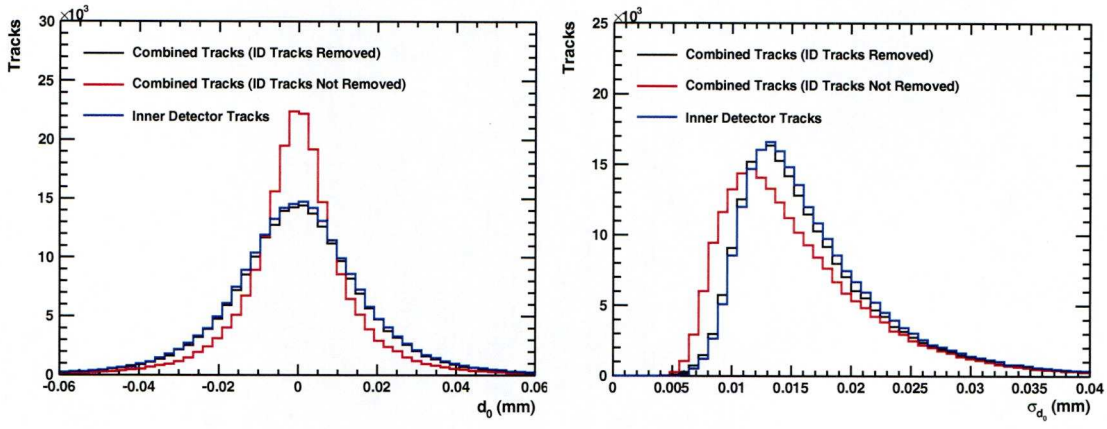

Figure 6.5: *The distributions of the transverse impact parameter d_0 (left) and its error σ_{d_0} (right) for combined muon tracks, with and without the removal of the inner detector track component from the vertex fit. The distributions of the transverse impact parameter and its error for the inner detector tracks themselves are also shown for comparison.*

as the distance of closest approach in the transverse plane of the muon track (d_0) divided by its error (σ_{d_0}). The impact parameter is defined with respect to the event's primary vertex in order to remove the effect of the spread in the beam spot position, which is 15 μm in both x and y. The error on the transverse impact parameter is determined from the errors on the detector hits from which the tracks are reconstructed, the error associated with the extrapolation of the track to the primary vertex and the error on the position of the primary vertex. When determining the impact parameter of the muon tracks the muon's inner detector track is removed from the primary vertex fit such that an unbiased impact parameter can be calculated with respect to the re-fitted vertex. The discriminant is defined as the maximum muon impact parameter significance of the four selected muons in the event.

The manner in which the impact parameters of combined muon tracks are treated in this analysis deviates from the methodology of the baseline analysis. For combined muon tracks the baseline analysis did not remove the original inner detector track, from which the combined track was created, from the primary vertex fit. As a result, the pull of the combined muon track on the primary vertex resulted in smaller impact parameters than expected. In this analysis, for combined muon tracks, the corresponding inner detector track is removed from the primary vertex fit before calculating the

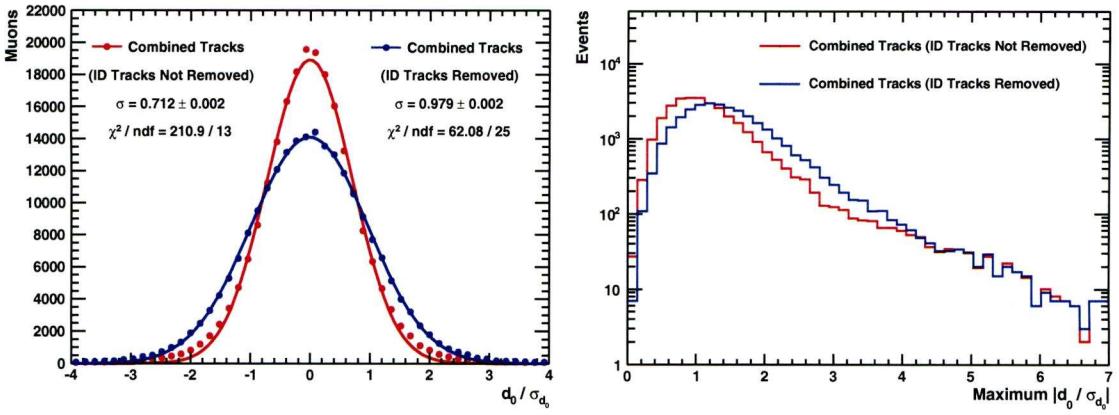

Figure 6.6: *The muon impact parameter significance for combined muon tracks (left) and the maximum impact parameter significance of combined muon tracks in selected candidate $H \rightarrow ZZ^{(*)} \rightarrow 4\mu$ events, with and without the removal of the inner detector track component from the vertex fit.*

impact parameter of the combined muon track with respect to the re-fitted primary vertex. The removal of this high p_T inner detector track from the primary vertex fit also leads to an increase in the error on the vertex fit and, as a result, the error on the calculated impact parameters are also larger than those that were observed in the baseline analysis. Both of these effects can be seen in Figure 6.5 which compares the distributions of the transverse impact parameter and its error for each of the two analysis methods. In both cases, the discriminating variable in the rejection of events from background processes is the maximum transverse impact parameter significance of the four selected muons in the event. The resulting distributions of the transverse impact parameter significance of the combined muon tracks for each of the two analysis methods are shown in Figure 6.6. The distributions suggest that the method used in this analysis, in which the inner detector components of the combined muon tracks are removed from the primary vertex fit, provides a more accurate estimate of the impact parameter significance.

In this analysis, the maximum transverse impact parameter significance of the muons is required to be less than 3.5. The maximum transverse impact parameter significance of the muons passing the preselection stage of the event selection is shown in Figure 6.7.

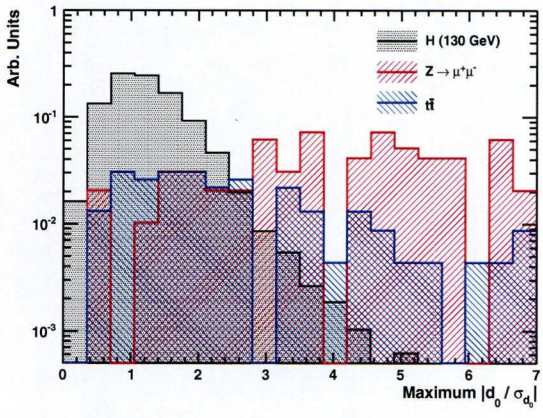

Figure 6.7: *The maximum transverse impact parameter significance of the four selected muons in both signal and background events passing the preselection and kinematic reconstruction stages of the event selection.*

6.4 Results

In order to determine the sensitivity to $H \rightarrow ZZ^{(*)} \rightarrow 4\mu$ events, a signal window is applied to the invariant mass of the four muons ($m_{\mu^+\mu^-\mu^+\mu^-}$) in candidate $H \rightarrow ZZ^{(*)} \rightarrow 4\mu$ events that have passed all event selection criteria. The signal window is defined as $m_H \pm 2\sigma_{m_H}$, where σ_{m_H} is the experimental width of the four muon mass distribution, as shown in Table 6.4. The increase in the experimental Higgs boson width with m_H is attributed to both an increase in the natural width of the Higgs boson and a decrease in the experimental precision, owing to the degradation in p_{T} resolution at high p_{T}, as discussed in Section 5.3.3. Since the Higgs boson couples more strongly to vector bosons than to fermions, the natural width of the Higgs boson increases significantly in the mass range where the di-boson decay channels open up. As such, for $m_H > 230$ GeV [57] the natural width of the Higgs boson dominates over the experimental resolution.

The percentage of signal events passing each of the event selection criteria, including the signal window, are shown in Table 6.5 for each of the signal samples considered. For comparison, the number of background events passing each of the $m_H = 130$ GeV event selection criteria are shown in Table 6.6. Both tables also show the number of events expected with an integrated luminosity of 1 fb^{-1}, which is the amount of $\sqrt{s} = 7$ TeV data expected to be collected by the ATLAS experiment between 2010 and

m_H (GeV)	σ_{m_H} (GeV)
130	1.6
140	1.7
150	1.9
160	2.2
170	2.3
180	2.4
190	2.7
200	2.9
300	6.7
400	17.2
500	33.6
600	50.9

Table 6.4: *The experimental width of the four muon mass distributions used to define the signal region [42].*

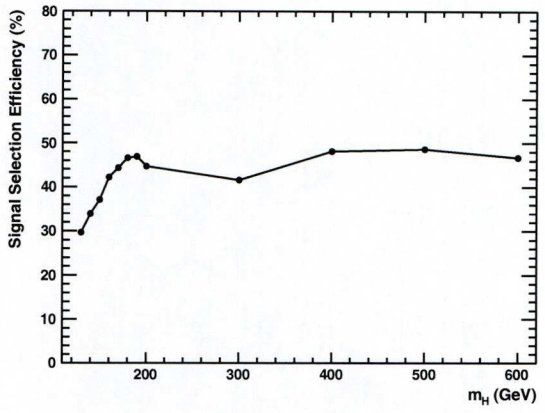

Figure 6.8: *The $H \rightarrow ZZ^{(*)} \rightarrow 4\mu$ selection efficiency as a function of m_H.*

2011, according to the latest LHC schedule [42]. The resulting signal selection efficiency as a function of m_H is shown in Figure 6.8. In summary, the total number of signal and background events expected to pass the full event selection, including the signal window, with 1 fb^{-1} of $\sqrt{s} = 7$ TeV collisions is shown in Table 6.7. Only the $ZZ^{(*)} \rightarrow 4l$ background is shown since none of the inclusive $Z \rightarrow \mu^+\mu^-$ events or $t\bar{t}$ events survive the full event selection process. The analysis also studied a dedicated background sample of approximately 200,000 $Zb\bar{b} \rightarrow \mu^+\mu^- + p$ events, where p = 0,1,2,3 as an alternative to the inclusive $Z \rightarrow \mu^+\mu^-$ sample but again, none of these background events survived the full event selection. The expected invariant mass distributions for the signal and background, normalised to 1 fb^{-1}, are shown in Figure 6.9 and Figure 6.10.

6.5 Systematic Uncertainties

An evaluation of the sensitivity of the ATLAS experiment to $H \rightarrow ZZ^{(*)} \rightarrow 4\mu$ events is dependent upon the number of observed signal candidate events and the number of expected background events within a given window. The signal selection efficiency and the background estimation in this window both have associated theoretical and experimental uncertainties, in addition to the statistical uncertainty of the process under study. The experimental uncertainties come from detector related uncertainties whilst the theoretical uncertainties originate from the calculations of cross sections and generator level Monte Carlo approximations. The main systematic uncertainties relating to the $H \rightarrow ZZ^{(*)} \rightarrow 4\mu$ analysis are described below [41].

	Signal m_H (GeV)											
	130	140	150	160	170	180	190	200	300	400	500	600
Trigger	98.32	98.74	99.07	99.26	99.34	99.27	99.26	99.35	99.61	99.64	99.56	99.54
	(0.69)	(1.02)	(1.07)	(0.46)	(0.23)	(0.51)	(1.55)	(1.69)	(0.92)	(0.67)	(0.28)	(0.12)
Preselection	56.96	62.62	64.27	67.25	68.75	69.30	70.41	68.87	71.83	74.41	75.98	75.15
	(0.40)	(0.65)	(0.70)	(0.31)	(0.16)	(0.35)	(1.10)	(1.17)	(0.66)	(0.50)	(0.21)	(0.09)
m_{12} Window	48.02	56.12	59.75	63.95	66.38	67.85	69.95	68.43	71.30	73.69	75.37	74.41
	(0.34)	(0.58)	(0.65)	(0.30)	(0.15)	(0.35)	(1.09)	(1.17)	(0.66)	(0.49)	(0.21)	(0.09)
m_{34} Window	40.84	46.13	49.53	56.84	60.28	65.06	67.07	63.81	58.42	61.15	62.49	62.33
	(0.28)	(0.48)	(0.54)	(0.26)	(0.14)	(0.33)	(1.05)	(1.09)	(0.54)	(0.41)	(0.17)	(0.07)
Calorimeter Isolation	39.29	44.98	48.26	55.16	58.31	62.81	64.58	61.60	57.30	60.03	61.44	61.26
	(0.28)	(0.46)	(0.52)	(0.26)	(0.13)	(0.32)	(1.01)	(1.05)	(0.53)	(0.40)	(0.17)	(0.07)
Track Isolation	36.71	42.29	45.63	52.19	55.46	59.61	60.99	58.85	56.59	59.64	60.92	60.93
	(0.26)	(0.44)	(0.49)	(0.24)	(0.13)	(0.31)	(0.95)	(1.00)	(0.52)	(0.40)	(0.17)	(0.07)
Impact Parameter	36.38	41.85	45.18	51.77	55.06	59.12	60.38	58.52	56.29	59.17	60.51	60.68
Significance	(0.26)	(0.43)	(0.49)	(0.24)	(0.13)	(0.30)	(0.94)	(1.00)	(0.52)	(0.39)	(0.17)	(0.07)
Signal Window	29.72	33.92	37.07	42.20	44.32	46.57	46.87	44.70	41.54	48.13	48.59	46.74
	(0.21)	(0.35)	(0.40)	(0.20)	(0.10)	(0.24)	(0.73)	(0.76)	(0.38)	(0.32)	(0.13)	(0.06)

Table 6.5: *The percentage of selected signal events (top) and the expected number of signal events for 1 fb^{-1} of $\sqrt{s} = 7$ TeV collisions (bottom) at each stage of the event selection process.*

	Background			
	$ZZ^{(*)}$	$Z \to \mu^+\mu^-$	$Zb\bar{b}$	$t\bar{t}$
Trigger	51.98 (52.93)	81.65 (730951.71)	87.18 (8963.75)	36.80 (32118.17)
Preselection	4.75 (4.84)	1.95×10^{-3} (17.48)	5.60×10^{-2} (4.98)	1.32×10^{-1} (115.35)
m_{12} Window	4.63 (4.71)	1.81×10^{-3} (16.22)	5.23×10^{-2} (4.64)	2.44×10^{-2} (21.33)
m_{34} Window	4.41 (4.49)	4.02×10^{-4} (4.60)	1.77×10^{-2} (1.62)	7.89×10^{-3} (6.88)
Calorimeter Isolation	4.25 (4.33)	8.05×10^{-5} (0.72)	1.33×10^{-3} (0.14)	4.78×10^{-3} (4.18)
Track Isolation	4.15 (4.23)	4.02×10^{-5} (0.36)	0 (0)	0 (0)
Impact Parameter Significance	4.11 (4.18)	0 (0)	0 (0)	0 (0)
Signal Window	0.03 (0.03)	0 (0)	0 (0)	0 (0)

Table 6.6: *The percentage of selected background events (top) and the expected number of background events for 1 fb^{-1} of $\sqrt{s} = 7$ TeV collisions (bottom) at each stage of the event selection process. The result corresponds to the selection criteria applied for $m_H = 130$ GeV.*

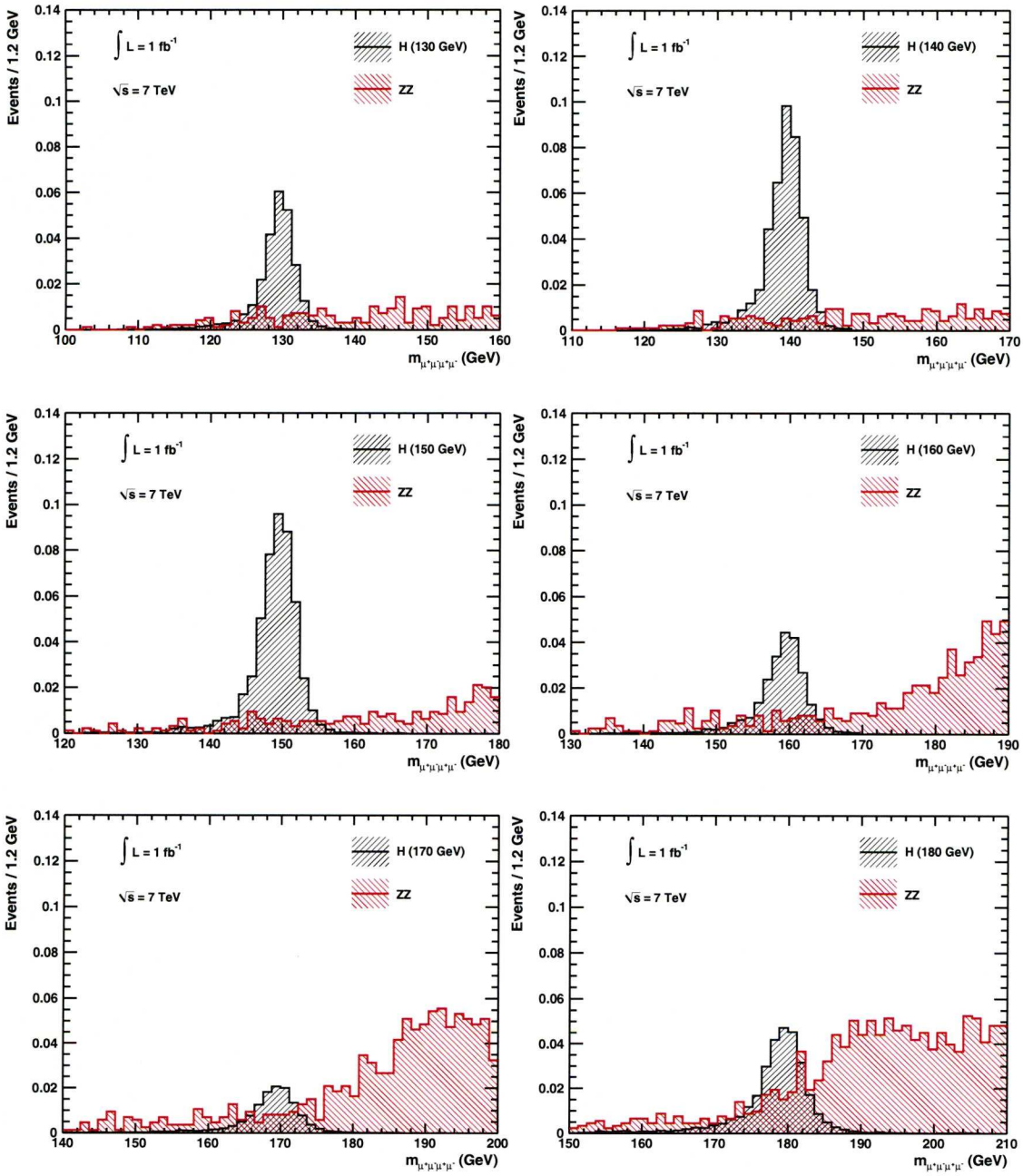

Figure 6.9: *The invariant mass distributions of the four muons in the candidate* $H \rightarrow ZZ^{(*)} \rightarrow 4\mu$ *events passing all the event selection criteria prior to the application of the signal window. The results are shown for the signal samples with* $m_H \leq 180$ GeV. *Only the* $ZZ^{(*)} \rightarrow 4l$ *background is shown since none of the inclusive* $Z \rightarrow \mu^+\mu^-$ *or* $t\bar{t}$ *events survive to this stage of the event selection process.*

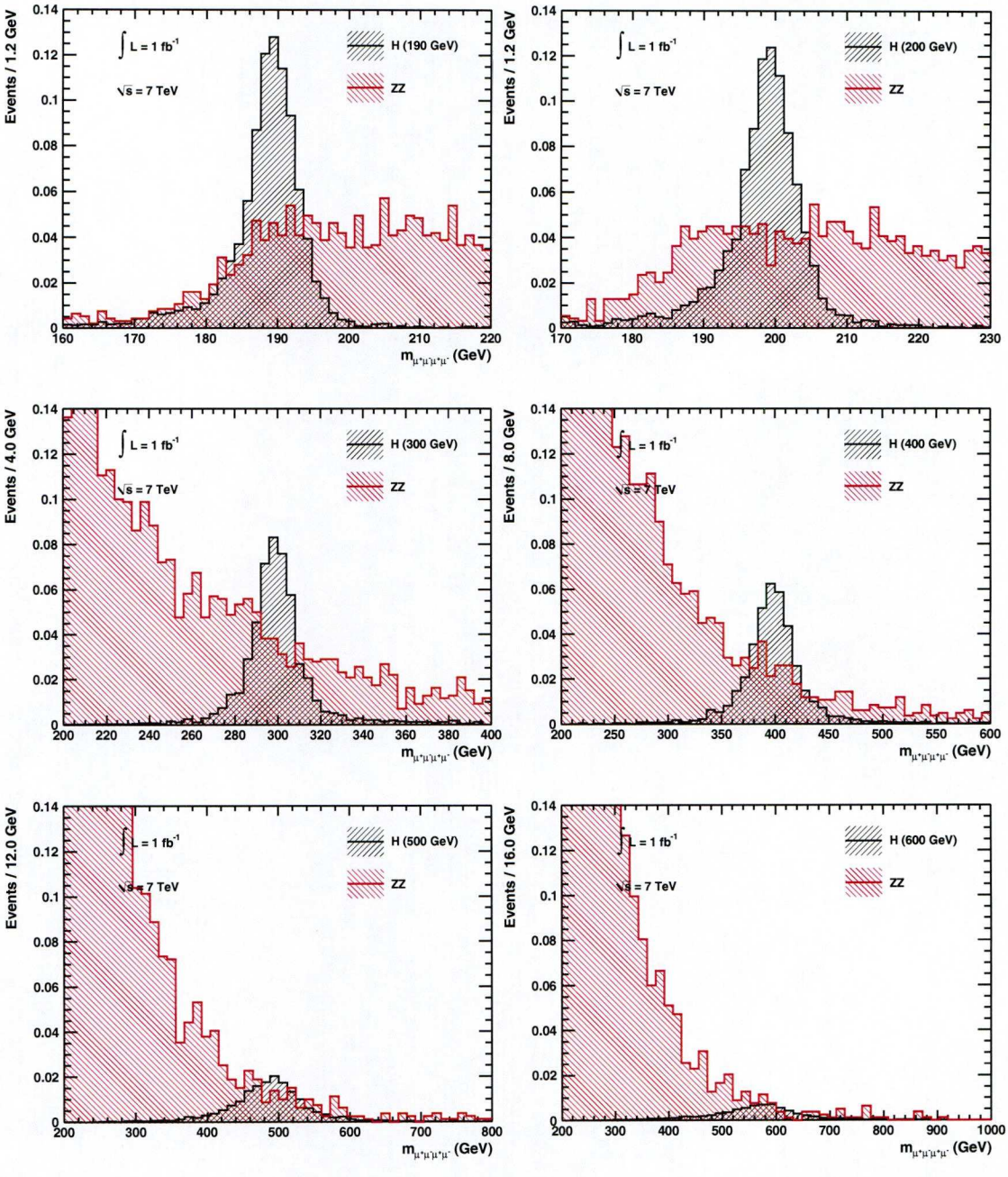

Figure 6.10: *The invariant mass distributions of the four muons in the candidate* $H \to ZZ^{(*)} \to 4\mu$ *events passing all the event selection criteria prior to the application of the signal window. The results are shown for the signal samples with* $m_H > 180$ GeV. *Only the* $ZZ^{(*)} \to 4l$ *background is shown since none of the inclusive* $Z \to \mu^+\mu^-$ *or* $t\bar{t}$ *events survive to this stage of the event selection process.*

m_H (GeV)	H	$ZZ^{(*)}$
130	0.21	0.03
140	0.35	0.02
150	0.40	0.04
160	0.20	0.05
170	0.10	0.07
180	0.24	0.16
190	0.73	0.39
200	0.76	0.40
300	0.38	0.25
400	0.32	0.21
500	0.13	0.14
600	0.06	0.11

Table 6.7: *The expected number of signal and background events for 1 fb^{-1} of $\sqrt{s} = 7$ TeV collisions after the full event selection criteria, including the application of the signal window.*

6.5.1 Theoretical

Theoretical uncertainties in the parton distribution functions (PDFs) and those related to the choice of the renormalisation and factorisation scales lead to uncertainties in the predicted cross sections for the signal and background processes.

The nature of the uncertainty is dependent upon the process in question. Scale uncertainties are usually estimated by varying the scales within a factor of two around the nominal scale chosen, whilst PDF uncertainties typically lead to uncertainties in the predicted cross sections of the order of 10% [41].

6.5.2 Experimental

Experimental uncertainties come from uncertainties relating to the integrated luminosity accumulated and the muon reconstruction performance. The precision with which the integrated luminosity accumulated can be measured is estimated to be 10%. The muon reconstruction performance can be determined from data, with a finite precision that is dependent upon the integrated luminosity. As such, the uncertainties relating to muon reconstruction performance have been estimated by the ATLAS Muon Peformance Group assuming an integrated luminosity of 1 fb^{-1}. The uncertainty in the muon identification efficiency is estimated to be 0.3% for $p_T < 100$ GeV, increasing to 3% at 1 TeV. The uncertainty in the muon p_T scale arising from uncertainties in the bending power of the magnetic fields is estimated to be 0.3%. Finally, uncertainties in the muon p_T resolution arising from uncertainties in the knowledge of the material distribution are estimated to be 4% for $p_T < 100$ GeV, increasing to 100% at 1 TeV. In addition, uncertainties in the alignment precision of the tracking detectors will also lead to uncertainties in muon performance. No estimate had previously been made of the uncertainties in the muon reconstruction performance originating from detector misalignments and thus their subsequent impact on the sensitivity to $H \to ZZ^{(*)} \to 4\mu$ events was unknown. This forms the subject of the following chapter.

6.6 Expected Exclusion Limits

The latest expectations for the sensitivity of the ATLAS detector to the Standard Model Higgs boson in the four lepton final state with 1 fb^{-1} of 7 TeV collisions are shown in Figure 6.11. The sensitivity is expressed as the median expected upper limit on the

production cross section at 95% confidence level, as a function of m_H. These expected limits are obtained by means of cross section rescaling, using the expected sensitivity prospects of the ATLAS detector at $\sqrt{s}$ =10 TeV[12] [42]. The scaling procedure implicitly assumes that the event selection efficiency is the same at the two centre-of-mass energies. This assumption has been checked by comparing kinematic distributions at generator level and by running the full analysis chain on selected samples. It was found that there is little difference in the kinematic distributions and that the event selection efficiencies agree to within 2% [57], providing confidence that the assumption is a reasonable one. After rescaling the cross section to obtain the sensitivity prospects of the ATLAS detector at $\sqrt{s}$ = 7 TeV, the limits themselves are then extracted using the profile likelihood method [41] at various values of m_H. The limits at these mass points are then interpolated to provide exclusion limits across the entire mass range.

The systematic uncertainties, as discussed in Section 6.5, are taken into account in the calculation of the exclusion limits. However, they are found to have a small effect on the sensitivity for exclusion, which is predominantly affected by the statistical fluctuations on the observed number of background events. In addition, the pile-up and cavern background present in the early running conditions are not expected to have any significant impact on the exclusion limits presented in Figure 6.11 [57].

In conclusion, the expected exclusion limits show that with the 1 fb^{-1} of 7 TeV data that is to be collected from now until 2011, the ATLAS detector cannot exclude the Standard Model Higgs boson in the four muon final state at 95% confidence level, for any value of m_H. The most sensitive mass region is that around m_H = 200 GeV, where an upper limit of 1.3 times the Standard Model prediction is expected. However, these expected exclusion limits are based on a conservative cut-based analysis and it is possible that a number of enhancements could be made in the context of a more aggressive approach. Furthermore, the combination of decay channels will increase the sensitivity of the ATLAS detector and should allow for the exclusion of a broad range of masses. The $H \to ZZ^{(*)} \to 4l$ channel will provide a significant contribution in determining this combined sensitivity, especially for $m_H > 200$ GeV, where the search

[12]The sensitivity prospects of the ATLAS detector for the $H \to ZZ^{(*)} \to 2e2\mu$ and $H \to ZZ^{(*)} \to 4e$ decay channels are documented in [42] and the systematics uncertainties relating to these analyses are described in [41]

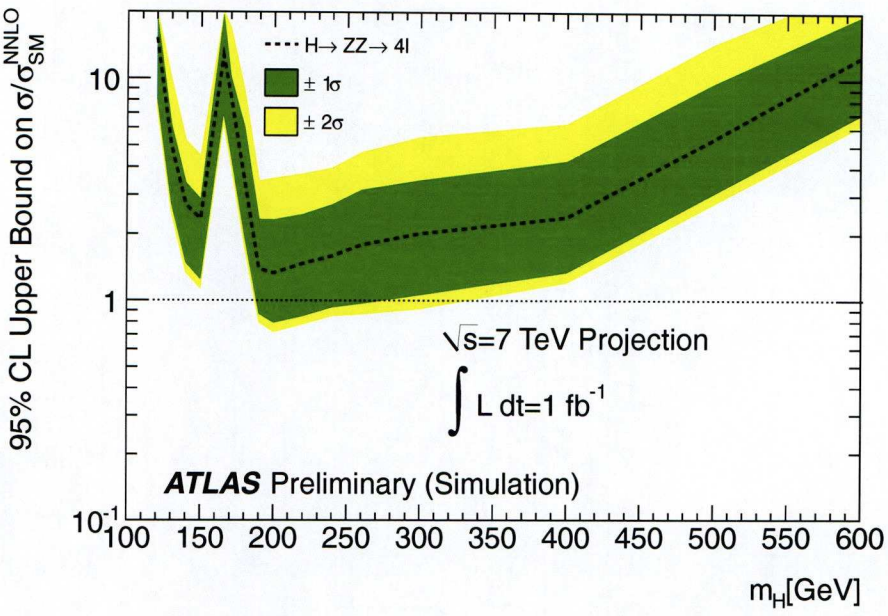

Figure 6.11: *The median expected (for the background only hypothesis) upper limits on Standard Model Higgs boson production in the four muon final state at 95% confidence level. These results are presented in terms of σ/σ_{SM}, the ratio of the expected upper limit to the rate predicted by the Standard Model, as a function of m_H. A value of σ/σ_{SM} less than or equal to one indicates that ATLAS can exclude the Standard Model Higgs boson at 95% confidence level. The shaded bands indicate the 68% and 95% probabililty regions in which σ/σ_{SM} is expected to fluctuate [58].*

for the Standard Model Higgs boson is based exclusively on the $H \rightarrow ZZ^{(*)}$ decay modes.

Chapter 7

Impact of Detector Misalignments on the Sensitivity to $H \rightarrow ZZ^* \rightarrow 4\mu$

In order to achieve the physics potential of the ATLAS experiment, accurate tracking and vertexing will be of crucial importance. The precision with which reconstructed track and vertex parameters can be determined is clearly dependent upon the level of alignment between the detector elements in each of the tracking detectors. As discussed in Chapter 2, it is estimated that the inner detector module positions must be known with a precision of 10 μm in the bending plane to ensure that the track parameters are not degraded by any more than 20%. Similarly, it is estimated that the muon spectrometer chamber positions must be known with a precision of 30 μm to achieve the design resolution of 10% at $p_{\mathrm{T}} = 1$ TeV. For both tracking systems, this level of alignment will not be achieved until after many months of collision data have been collected. Even then a correct convergence of the alignment process is not always guaranteed, as there are some coherent deformations of detector elements to which the alignment procedures are relatively insensitive. Such global systematic deformations, known as weak modes, may even be introduced by the alignment process itself and are likely to remain afterwards. The alternative topology of cosmic muon events may help to constrain some of these weak modes although ultimately additional external and physical constraints will also be required. Understanding the effects of detector misalignments on the tracking and vertexing performance is therefore of crucial importance

in determining the subsequent effects on physics analyses.

In order to study the impact of detector misalignments on the senstivity to $H \rightarrow ZZ^* \rightarrow 4\mu$ events, for which no estimates had previously been made, Monte Carlo samples of 60,000 $H \rightarrow ZZ^* \rightarrow 4\mu$ events with $m_H = 130$ GeV at $\sqrt{s} = 10$ TeV were privately generated with different misalignment scenarios. Inner detector misalignments, muon spectrometer misalignments and relative misalignments between the two tracking systems were all considered in the simulations. Simulated hits were then reconstructed assuming the nominal ATLAS detector description and, where appropriate, error scaling was included to compensate for the detector misalignments introduced. Every step in the production of these misaligned $H \rightarrow ZZ^* \rightarrow 4\mu$ samples was performed using the official ATLAS Monte Carlo production software.

7.1 Detector Misalignments

For both the inner detector and the muon spectrometer, three different misalignment scenarios were considered. For one such scenario, each of the detectors were simulated with their expected as-built alignment precision. For the inner detector, alignment corrections were determined from a first pass alignment exercise performed by the inner detector alignment community as part of the commissioning of the inner detector alignment software [59]. These preliminary alignment constants are considered to represent an estimate of the expected alignment precision for the earliest data. It was intended that the muon spectrometer alignment community would perform a similar procedure on the as-built muon spectrometer description, although such an alignment was never performed. For both detectors, these misalignment scenarios are the most severe of the three considered. In fact in both cases, the resulting alignment precisions are known to be worse than the current estimates. Nevertheless, these severely misaligned scenarios are useful in studying the relative effects of the different levels of misalignment. Prior to collision data taking, the inner detector and the muon spectrometer alignment groups each provided sets of alignment constants designed to represent the alignment precision that could be expected after 1 day and after 100 days of collision data. These alignment constants provide the most accurate description of the ATLAS detector and, as such, their impact on the senstivity to $H \rightarrow ZZ^* \rightarrow 4\mu$ events will therefore be the main focus of this study.

7.1.1 Inner Detector

The as-built inner detector description includes both translational and rotational misalignments of detector elements, randomly generated from flat distributions of various widths, centered on zero. For the largest misalignment applied, the widths of the distributions were of the order 1 mm and 1 mrad [60]. To account for possible weak modes, a limited number of systematic deformations were also incorporated into the detector description. As part of the commissioning of the inner detector alignment, what was known as the Computing Services Challenge (CSC) alignment exercise was performed on this misaligned geometry. This so-called CSC alignment was based on the minimisation of track residuals and proceeded as follows:

- The pixel and the SCT were aligned internally using simulated multi-muon events in which all the muons originated from a single vertex.
- Further alignment using simulated cosmic ray events, with and without the magnetic field, was performed to try to remove the weak mode distortions.
- Finally, the TRT was aligned using the simulated multi-muon events; firstly with respect to the aligned pixel detector and SCT and then internally.

It is likely that residual misalignments will remain after the first pass alignment due to both statistical limitations of the alignment procedure and the presence of these weak mode deformations. Determining the size of these residual misalignments is difficult, particularly when weak modes are present. Nevertheless, the residual misalignments that do remain can be considered to be representative of the alignment precision that can be achieved in very early data.

More recently, the ATLAS inner detector alignment community have provided additional alignment constants representing the expected alignment precision after 1 day and after 100 days of collisions data. These alignment constants artificially introduce the detector misalignments by displacing the nominal coordinates of the detector elements in each of the three sub-detectors. The magnitudes of these displacements were defined by randomly smearing the nominal coordinates with gaussian distributions of various widths, centered on zero. These widths, for both the day 1 and day 100 alignment constants, are shown in Table 7.1 [61].

	Day 1		Day 100	
	Barrel	Endcaps	Barrel	Endcaps
Pixel	20 μm	50 μm	10 μm	10 μm
SCT	20 μm	50 μm	10 μm	10 μm
TRT	100 μm	100 μm	50 μm	50 μm

Table 7.1: *The widths of the gaussian distributions from which the inner detector module displacements were randomly generated for the day 1 and day 100 alignment constants.*

The gaussian widths for the day 1 alignment constants were determined by quadratically subtracting the width of the track residual distribution in simulated cosmic muon events with a nominal detector description, from the width of the track residual distribution observed in aligned cosmic data. The resulting alignment precision to be expected on day 1 is slightly more optimistic than the alignment precision of the aligned as-built detector description described previously. In particular, because the day 1 and day 100 alignment constants do not include any rotational misalignments of detector elements nor do they incorporate any weak mode deformations. The gaussian widths for the day 100 alignment constants have subsequently been designed to represent a best-estimate of the alignment precision to be expected after 100 days of collision data.

7.1.2 Muon Spectrometer

The as-built muon spectrometer description includes both rotational and translational misalignments of the muon spectrometer chambers, randomly generated from gaussian distributions of widths 1 mm and 1 mrad centered on zero [41]. Unlike the as-built inner detector description, the as-built muon spectrometer description was not subject to alignment and, as such, the resulting alignment precision is therefore considered by the muon spectrometer alignment community to be over-pessimistic. The muon spectrometer chamber misalignments do not include any systematic radial displacements of the chambers with respect to each other, nor do they account for relative misalignments between the two drift tube multilayers that comprise each chamber. Both of these additional misalignments would be expected to have a strong impact on the tracking

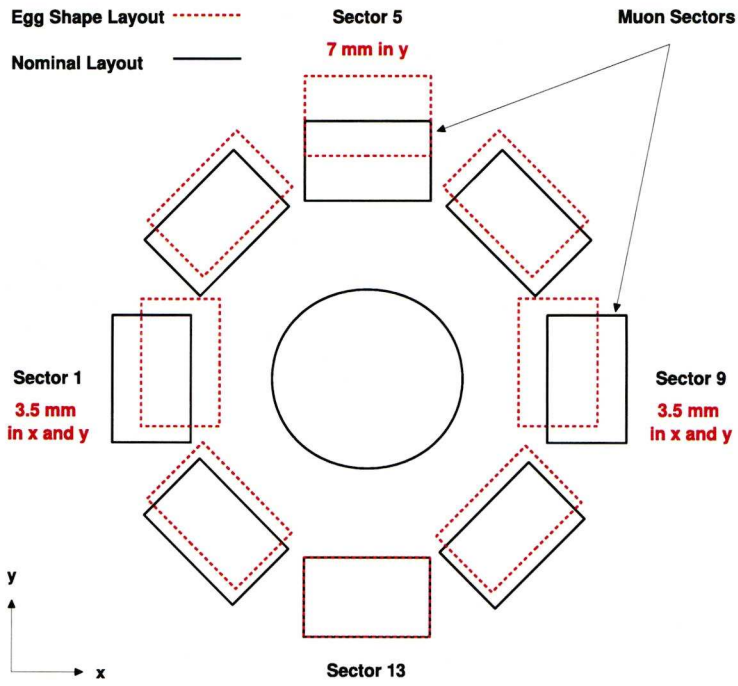

Figure 7.1: *The egg shape description of the muon spectrometer, indicating the systematic shifts of the chambers and the resulting inter-detector misalignments [62]. Only the odd numbered muon spectrometer sectors are shown.*

performance in the muon spectrometer.

The day 1 and day 100 alignment constants were motivated by observations from both cosmic data and the muon spectrometer optical alignment system. The magnitude of the misalignments are described by an upper bound on the expected track sagitta bias. In the barrel, the day 1 alignment constants represent an uncertainty in the track sagitta of approximately 100 μm, except for the side sectors where the uncertainty on the track sagitta is larger. For the day 100 alignment constants, the uncertainty in the track sagitta is under 100 μm everywhere in the barrel. In the endcaps, both the day 1 and the day 100 alignment constants represent an uncertainty of 45-50 μm on the track sagitta.

To investigate the impact of relative misalignments between the inner detector and the muon spectrometer, the chambers in each barrel sector of the muon spectrometer were systematically shifted and rotated about their nominal positions to form the so-called egg shape geometry in the global $x - y$ plane, as shown in Figure 7.1. Here, the chambers in sector 5 are shifted by 7 mm in y and the chambers in sectors 1 and 9 are

shifted by 3.5 mm in both x and y. The chambers in sector 13 are not displaced, nor are the chambers in the endcaps. All other chambers are shifted and rotated such that they are tangent to the assumed egg shape. The chambers within each sector are not displaced with respect to each other and as such, the egg shape geometry only introduces relative global misalignments between the ϕ sectors of the muon spectrometer. The misalignments are somewhat arbitrary in their direction and magnitude but nevertheless allow for the study of the impact of global muon spectrometer deformations and the subsequent misalignments in relation to the inner detector.

7.2 Muon Identification and Reconstruction Performance

The impact of detector misalignments on the sensitivity to $H \rightarrow ZZ^* \rightarrow 4\mu$ events will ultimately originate from the impact of the misalignments on the identification and reconstruction of the final state muons. The peformance of the STACO reconstruction chain, in terms of the identification efficiency, the $1/p_{\mathrm{T}}$ scale and the fractional $1/p_{\mathrm{T}}$ resolution has therefore been determined using 60,000 $H \rightarrow ZZ^* \rightarrow 4\mu$ events with $m_H = 130$ GeV, in which muons are required to have $p_{\mathrm{T}} > 5$ GeV and $|\eta| < 2.5$. These performance metrics are defined in Chapter 5 and all of the different misalignment scenarios described earlier in Section 7.1 have been considered.

7.2.1 Identification Efficiency

Neither the inner detector misalignments nor the muon spectrometer misalignments are observed to have significant impact on the muon indentification efficiency. For comparison, the identification efficiencies observed for the nominal detector description and for the most severe misalignment scenario are shown in Figure 7.2.

The observed insensitivity of the muon indentification efficiency to the detector misalignments can be attributed to the inclusion of track error scaling in the event reconstruction. This scaling inflates the track hit errors so that the tracking algorithms can still identify and reconstruct the muon tracks despite the detector misalignments. Although the application of track error scaling maintains high muon identification efficiencies in both the inner detector and the muon spectrometer, the misalignments can still introduce track parameter biases and degrade track parameter resolutions.

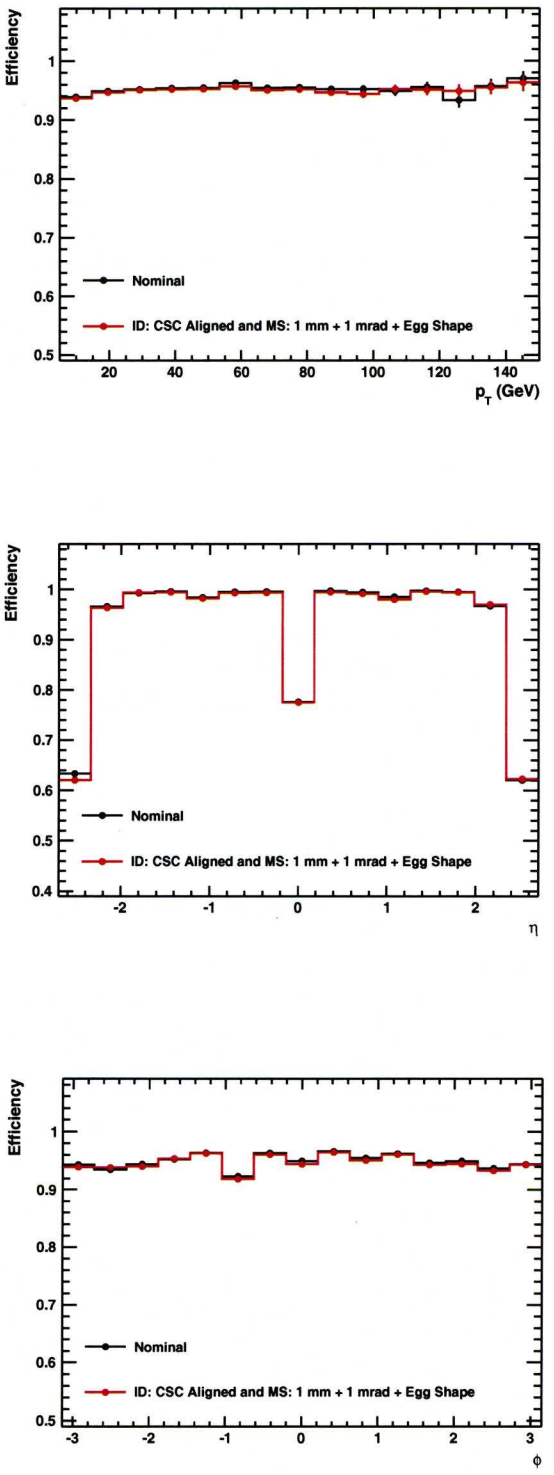

Figure 7.2: *The muon identification efficiencies, inclusive of all muon categories, in both nominal and misaligned detectors as a function of* p_{T} *(top),* η *(middle) and* ϕ *(bottom).*

7.2.2 $1/p_{\mathrm{T}}$ Scale

The $1/p_{\mathrm{T}}$ scale of combined muon tracks for the nominal detector description and for the most severe misalignment scenario are shown in Figure 7.3. Such tracks should be sensitive to the inner detector misalignments, the muon spectrometer misalignments and the relative misalignments between the two detectors. However, none of the misalignments appear to have any significant impact on the muon $1/p_{\mathrm{T}}$ scale. This can be attributed to the fact that most of the detector misalignments are random misalignments, generated from distributions of specific widths, centered on a translation or rotation equal to 0. For most of these random misalignments the effects are local and tend to cancel out along the full length of a track. It would therefore be expected that the muon $1/p_{\mathrm{T}}$ scale is more sensitive to global systematic deformations, such as the weak modes incorporated into the as-built inner detector description or the distinctive ϕ asymmetry introduced by the egg shape description of the muon spectrometer. Although Figure 7.3 would suggest that neither of these global misalignments have any significant impact on the reconstructed $1/p_{\mathrm{T}}$ scale, it should be mentioned that summing over positive and negative charged tracks can mask some effects. Furthermore, the misalignments considered are by no means comprehensive and, as such, alternative global systematic deformations may have a more significant impact on the muon $1/p_{\mathrm{T}}$ scale.

7.2.3 $1/p_{\mathrm{T}}$ Resolution

The impact of the different inner detector misalignment scenarios on the fractional $1/p_{\mathrm{T}}$ resolution of inner detector muon tracks and combined muon tracks are shown in Figure 7.4.

Since the inner detector alignment procedure is track-based, the achievable alignment precision in the early stages will be dominated by statistical limitations. As a result, a significant improvement in the fractional $1/p_{\mathrm{T}}$ resolution is observed with the alignment precision at day 100, in comparison to the alignment precision at day 1, for which the fractional $1/p_{\mathrm{T}}$ resolution becomes comparable with the nominal resolution.

The fractional $1/p_{\mathrm{T}}$ resolution remains relatively flat as a function of ϕ with the alignment precisions at day 1 and day 100. However, for the aligned, as-built inner detector description the fractional $1/p_{\mathrm{T}}$ resolution shows some degree of structure in ϕ,

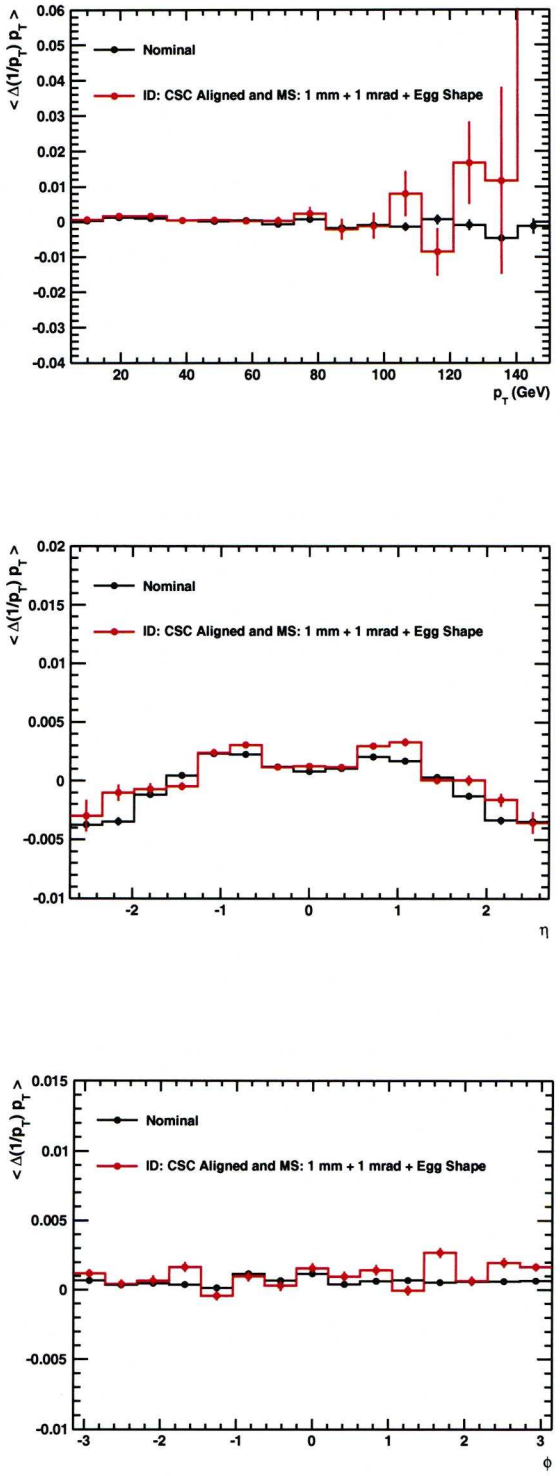

Figure 7.3: *The $1/p_{\mathrm{T}}$ scale of combined muon tracks in both nominal and misaligned detectors as a function of p_{T} (top), η (middle) and ϕ (bottom).*

which could indicate a sensitivity to the residual, global systematic deformations that have remained after the alignment process.

The impact of the different muon spectrometer misalignment scenarios on the fractional $1/p_{\mathrm{T}}$ resolution of muon spectrometer tracks and combined muon tracks are shown in Figure 7.5. The fractional $1/p_{\mathrm{T}}$ resolution that can be achieved in the muon spectrometer with the alignment precision at day 1 is already comparable to the nominal fractional $1/p_{\mathrm{T}}$ resolution. The fact that the muon spectrometer performs so well, even at day 1, is due to the long cosmic muon campaign prior to collision data taking, that allowed for a better understanding of the detector. However, even with the alignment precision at day 100, a significant degradation in the fractional $1/p_{\mathrm{T}}$ resolution is observed for combined muon tracks in the range $2.0 < |\eta| < 2.7$. No degradation in the fractional $1/p_{\mathrm{T}}$ resolution of the muon spectrometer tracks is observed in this η range, which suggests that the origin of the problem may lie in the combination of the inner detector tracks with the muon spectrometer tracks.

The more severe misalignments present in the as-built muon spectrometer description are observed to have a significant impact on the fractional $1/p_{\mathrm{T}}$ resolution of the muon spectrometer tracks. However, when these tracks are combined with inner detector tracks, the fractional $1/p_{\mathrm{T}}$ resolution improves considerably, suggesting that the inner detector plays an important role in the p_T range under study and that the alignment of the inner detector will therefore be of crucial importance.

The egg shape description of the muon spectrometer introduces a distinctive ϕ asymmetry and results in the relative misalignment of the muon spectrometer sectors with respect to the inner detector. These misalignments have already been shown to have a limited impact on the muon identification efficiency and on the muon $1/p_{\mathrm{T}}$ scale and, as can be seen in Figure 7.6, the misalignments also have very little impact on the muon fractional $1/p_{\mathrm{T}}$ resolution. This would suggest that muon identification and reconstruction are effectively insensitive to misalignments of this nature. However, this apparent insensitivity could be due to the fact that for the process under study, the fractional $1/p_{\mathrm{T}}$ resolution has a strong reliance on the inner detector measurements, in which case effects may appear at higher p_{T}. Furthermore, the global systematic deformations of the egg shape are very particular and it is possible that relative misalignments between the inner detector and the muon spectrometer will, in reality, be larger and more complex.

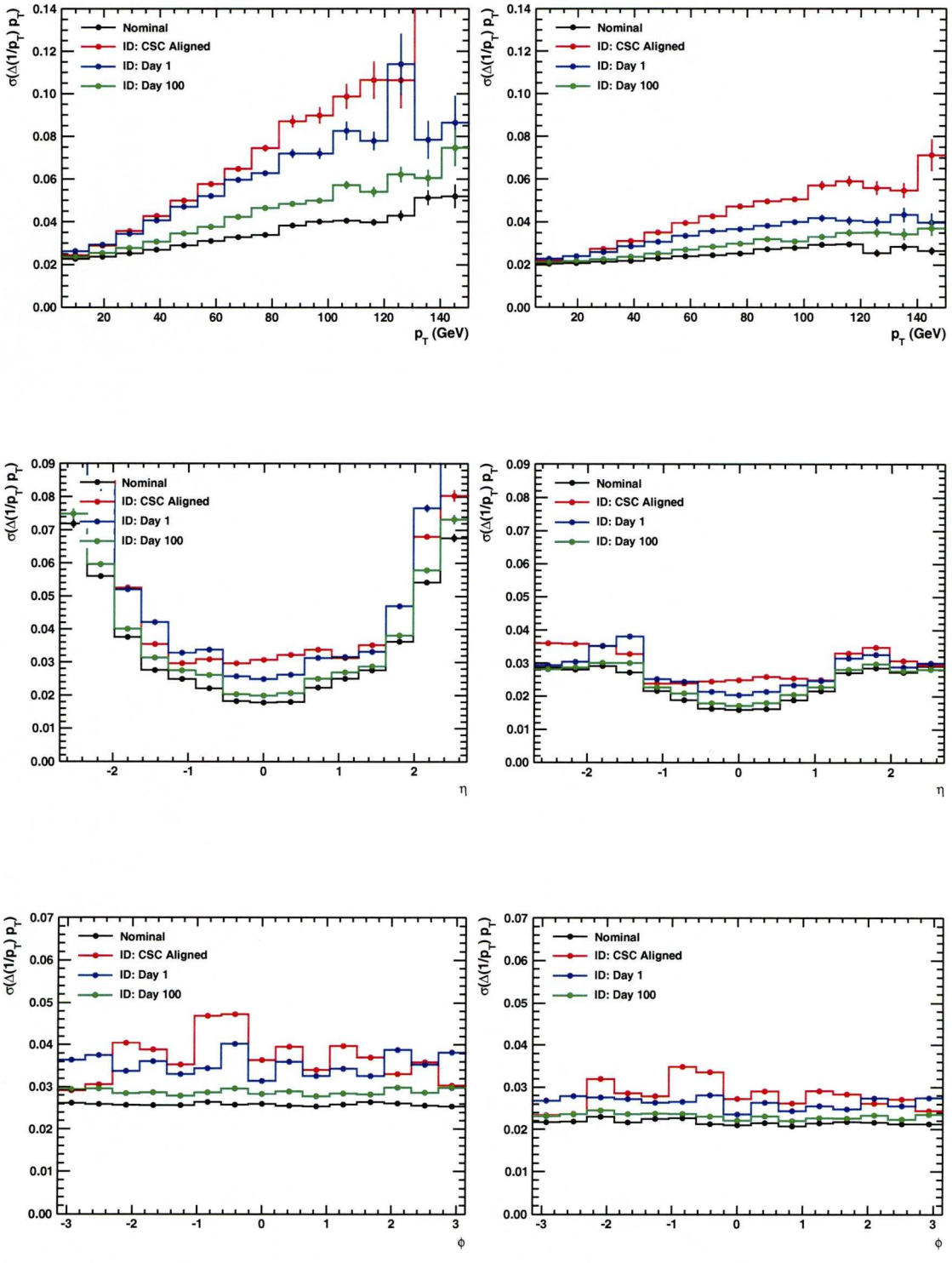

Figure 7.4: *The fractional $1/p_{\mathrm{T}}$ resolution of inner detector muon tracks (left) and combined muon tracks (right) for the different inner detector misalignment scenarios as a function of p_{T} (top), η (middle) and ϕ (bottom).*

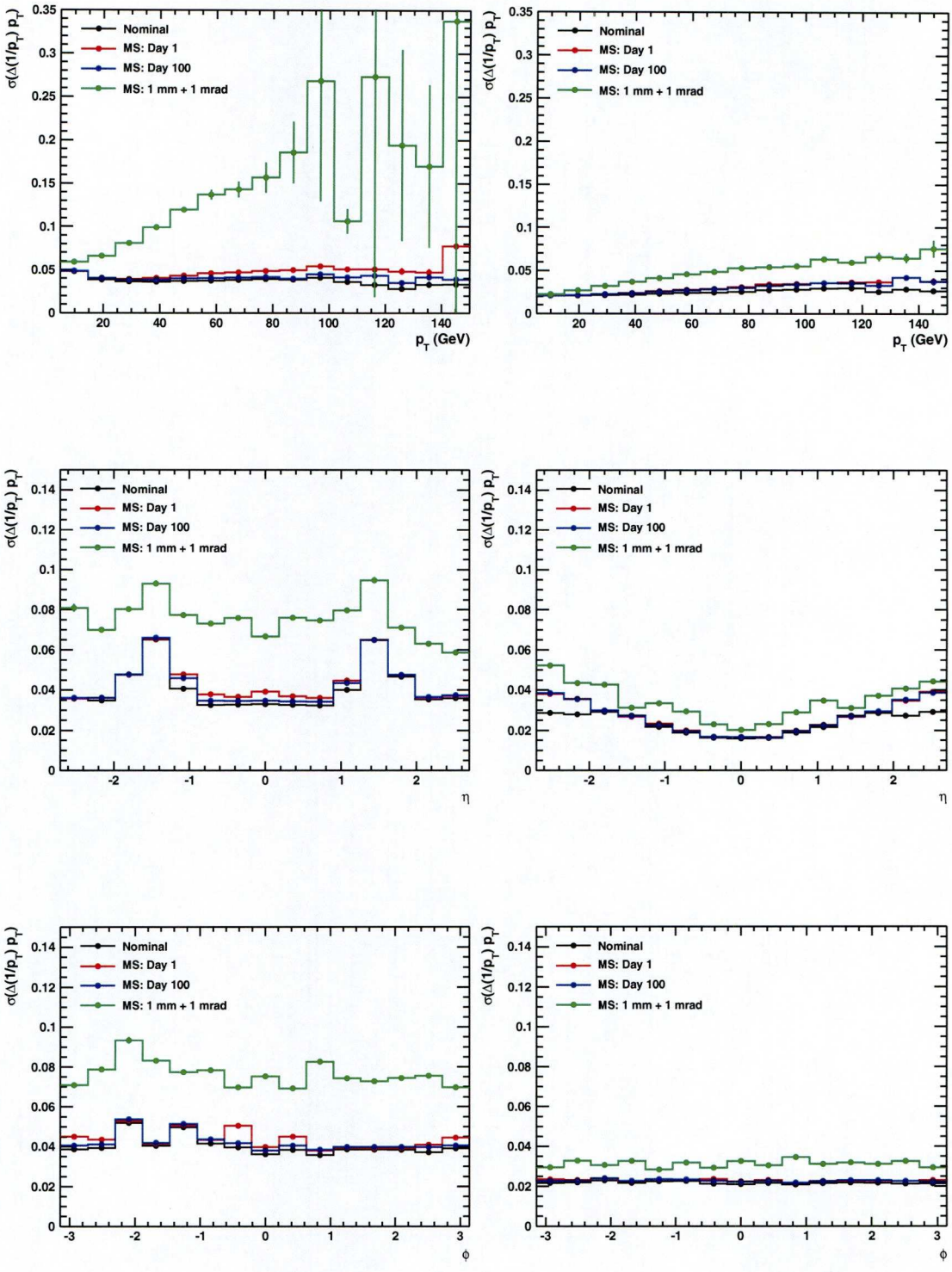

Figure 7.5: *The fractional $1/p_{\mathrm{T}}$ resolution of extrapolated muon spectrometer tracks (left) and combined muon tracks (right) for the different muon spectrometer misalignment scenarios as a function of p_{T} (top), η (middle) and ϕ (bottom).*

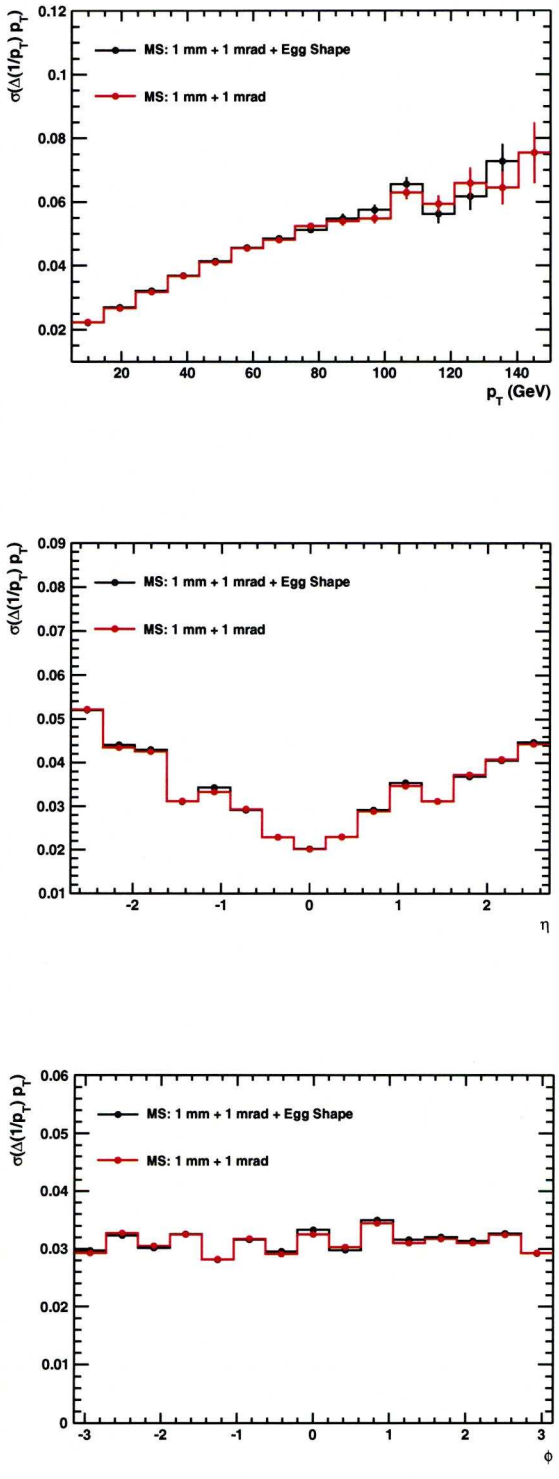

Figure 7.6: *The fractional $1/p_{\mathrm{T}}$ resolution of combined muon tracks for the as-built muon spectrometer description, both with and without the egg shape deformation, as a function of p_{T} (top), η (middle) and ϕ (bottom).*

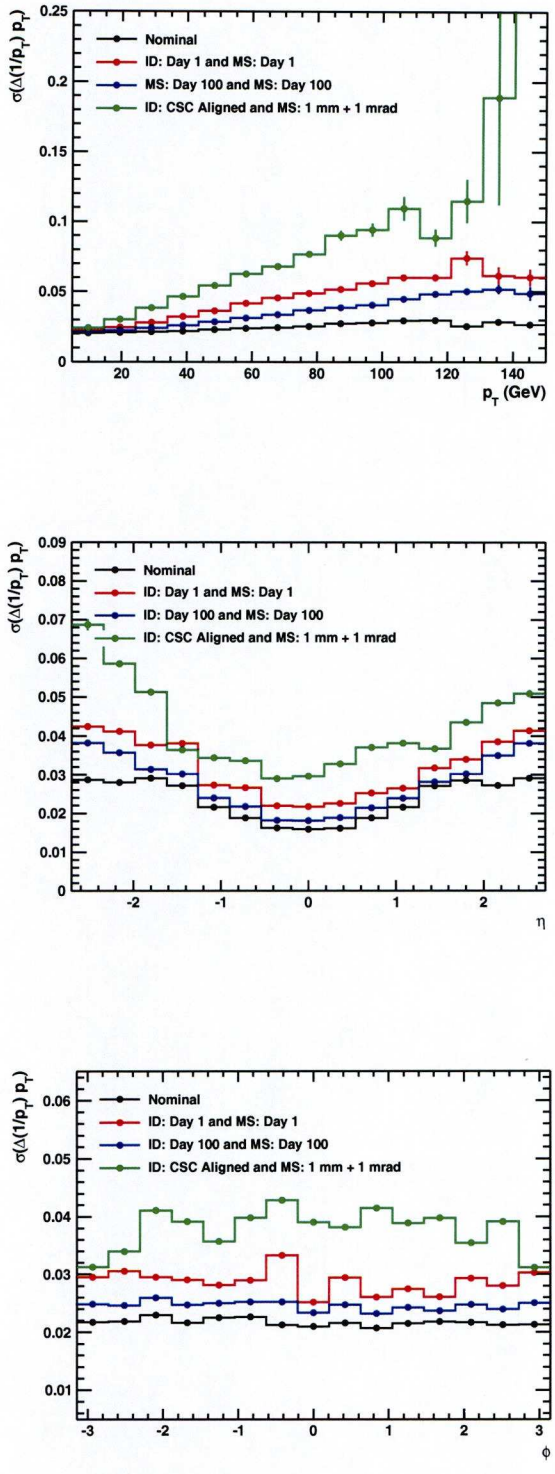

Figure 7.7: *The fractional $1/p_{\mathrm{T}}$ resolution of combined muon tracks for the different inner detector and muon spectrometer misalignment scenarios as a function of p_{T} (top), η (middle) and ϕ (bottom).*

Although it can be informative to consider the effects of the inner detector misalignments and the muon spectrometer misalignments independently, a combination of the misalignments represents the most realistic description of the ATLAS detector. The impact of the different inner detector and muon spectrometer misalignment scenarios combined, on the fractional $1/p_{\mathrm{T}}$ resolution of combined muon tracks is shown in Figure 7.7. It can be seen that a significant improvement in the fractional $1/p_{\mathrm{T}}$ resolution of combined muon tracks can be achieved with the alignment precision at day 100, in comparison to the alignment precision at day 1. Even with the expected alignment precision at day 100, further improvements in the fractional $1/p_{\mathrm{T}}$ resolution can be achieved, particularly at high p_{T} and in the forward regions beyond $|\eta| = 2$. Since the fractional $1/p_{\mathrm{T}}$ resolution achievable in the muon spectrometer at day 1 is already very close to the nominal fractional $1/p_{\mathrm{T}}$ resolution, any improvement in the fractional $1/p_{\mathrm{T}}$ resolution of the combined muon tracks will orginate from improvements in the alignment precision of the inner detector. This serves to further illustrate the importance of the inner detector measurements in the performance of the combined muon tracks.

7.3 Sensitivity to the Relative Misalignment of the Tracking Detectors

In the muon spectrometer the alignment is performed by an optical alignment system [63, 64], in which the chambers within each sector are aligned with respect to each other. The alignment between sectors and the alignment with the inner detector relies on track based alignment procedures. During the lifetime of the ATLAS experiment, it is possible that relative misalignments between the inner detector and the muon spectrometer, such as those described by the egg shape, will appear over time. Although the egg shape description of the muon spectrometer has been observed to have little impact on the muon identification and reconstruction performance, it is nevertheless important to know how such misalignments may be identified and measured with track based methods. This is particularly important since although the inner detector and muon spectrometer alignment communities in the ATLAS experiment are very large, much less man-power has been invested in the relative alignment of the two tracking detectors.

One variable that is more sensitive to the egg shape deformations is the longitudinal

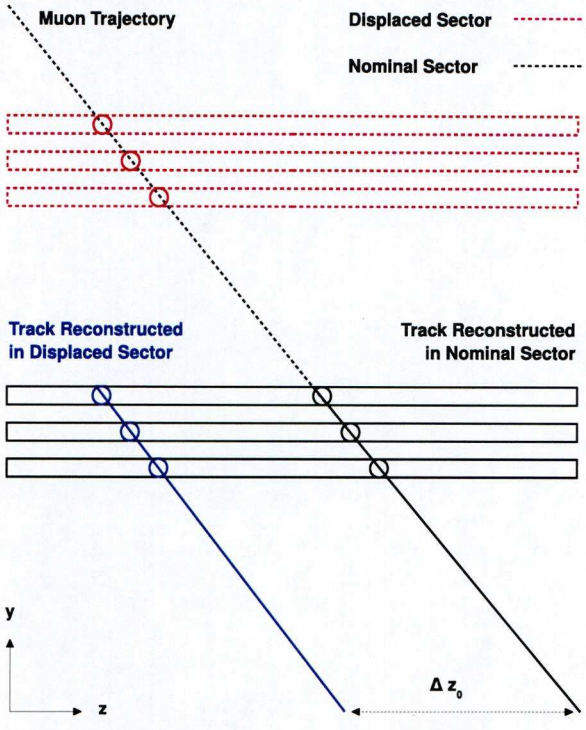

Figure 7.8: *The impact of shifts in the sectors of the muon spectrometer on the longitudinal impact parameters of muon spectrometer tracks extrapolated back to the interaction point. When the sector is displaced from its nominal position, the muon spectrometer hits are shifted with respect to where they would have been in a nominally aligned sector. This is illustrated above, whereby a muon in the misaligned sector would leave the top three red hits which are displaced with respect to the bottom three black hits that the same muon would leave in a nominally aligned sector. Since the track reconstruction is unaware of the sectors displacement, it assumes that the sector is located in its nominal position and, as such, the track reconstruction assumes that the measured hits are where the blue hits are. The subsequent tracks are therefore shifted with respect to the tracks that would have been reconstructed in a nominally aligned sector.*

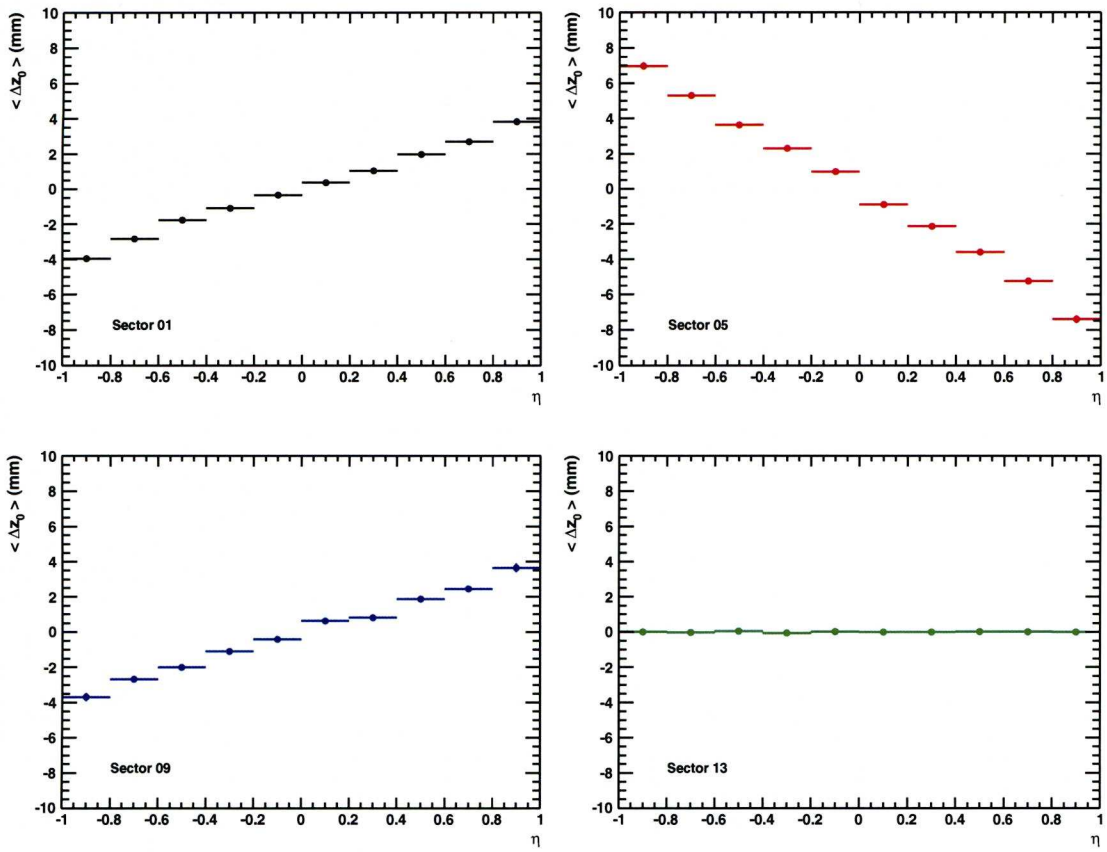

Figure 7.9: *The observed shift in the measured z_0 of extrapolated muon spectrometer tracks in various sectors when comparing detector descriptions with and without the egg shape deformation.*

impact parameter (z_0) of muon spectrometer tracks that have been extrapolated back to the interaction point [62]. Since the event reconstruction is unaware of the misalignments, tracks that are reconstructed from hits in the chambers of the displaced muon spectrometer sectors will be shifted with respect to the true muon trajectories. This is illustrated in Figure 7.8. As a result, the displacements of the sectors lead to observable shifts in the measured impact parameters of extrapolated muon spectrometer tracks. Furthermore, the magnitude and direction of the observed shifts in the impact parameters relate strongly to the magnitude and direction of the displacements of the sectors, as shown in Figure 7.9. This sensitivity to the egg shape deformations indicates that a direct comparison of the impact parameters of matched inner detector tracks and extrapolated muon spectrometer tracks may provide an additional track-based method of aligning the muon spectrometer with respect to the inner detector.

7.4 Impact on the Sensitivity to $H \rightarrow ZZ^* \rightarrow 4\mu$

In order to determine the impact of detector misalignments on the sensitivity to $H \rightarrow ZZ^* \rightarrow 4\mu$ events, it is necessary to understand the effects of the misalignments on each of the signal selection criteria and the subsequent impact on the signal selection efficiency. The detector misalignments are expected to have a significant impact on both the Z mass width, the H mass width and the d_0/σ_{d_0} distribution, which is used as a discriminant in the rejection of background $Zb\bar{b}$ and $t\bar{t}$ events. The impact of the detector misalignments on each of these features is described below.

7.4.1 Z Mass Width

The invariant mass distribution for the leading di-muon pairs in candidate $H \rightarrow ZZ^* \rightarrow 4\mu$ events that have passed the event preselection are fitted with gaussian distributions, from which the width is taken to reflect the Z mass width. The measured widths of the gaussian distributions for each of the misalignment scenarios considered are shown in Table 7.2. The combined impact of both the inner detector misalignments and the muon spectrometer misalignments on the Z mass width is shown in Figure 7.10. With the alignment precision at day 1 the measured Z mass width is 3.18 ± 0.03 GeV, which represents a 39% increase with respect to the nominal detector description. A significant improvement can be achieved with the expected alignment precision at day 100,

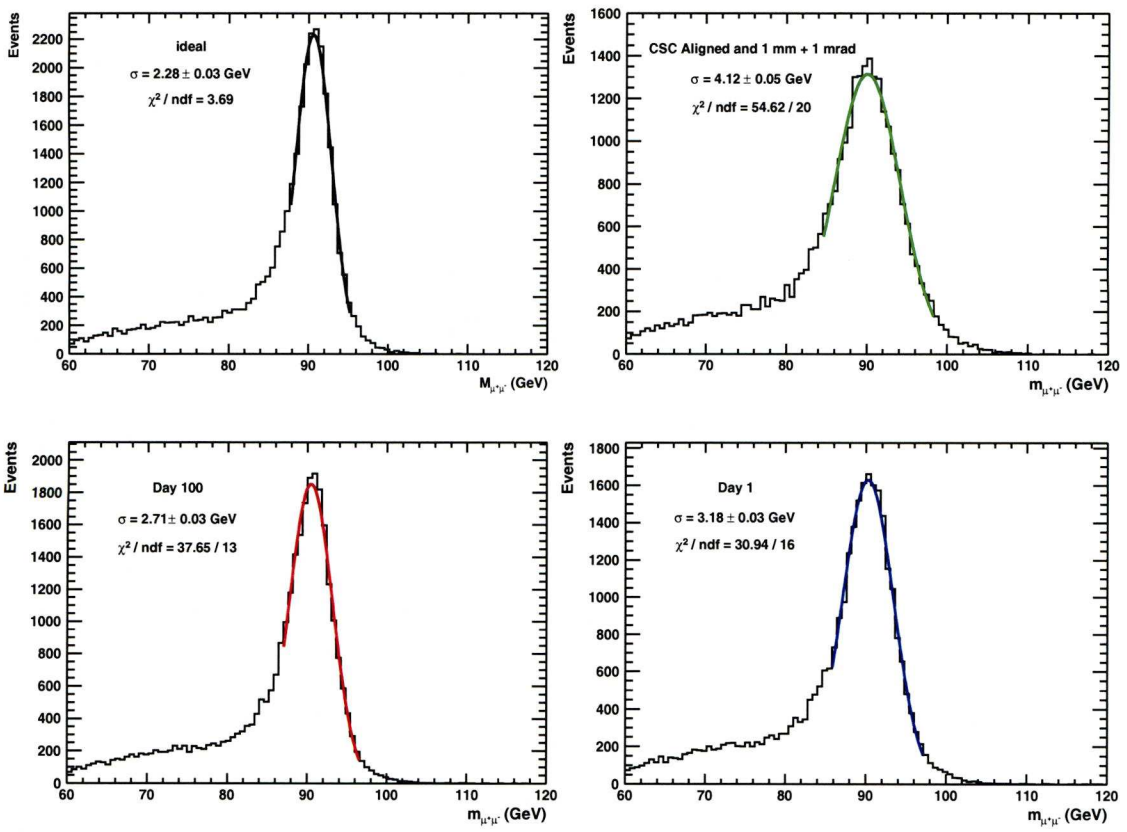

Figure 7.10: *The invariant mass distributions of the leading di-muon pairs in candidate $H \rightarrow ZZ^* \rightarrow 4\mu$ events that have passed the event preselection.*

for which the Z mass width is measured to be 2.71 ± 0.03 GeV, representing a 19% increase with respect to the nominal detector description.

7.4.2 H Mass Width

The invariant mass distribution for the four muons in candidate $H \rightarrow ZZ^* \rightarrow 4\mu$ events that have passed all event selection criteria are fitted with gaussian distributions, from which the width is taken to reflect the H mass width. The measured widths of the gaussian distributions for each of the misalignment scenarios considered are shown in Table **??**. The combined impact of both the inner detector misalignments and the muon spectrometer misalignments on the H mass width is shown in Figure 7.11. With the alignment precision at day 1 the measured H mass width is 2.54 ± 0.02 GeV, which represents a 46% increase with respect to the nominal detector description. A large improvement can be achieved with the expected alignment precision at day 100, for which the H mass width is measured to be 2.04 ± 0.02 GeV, representing a 17%

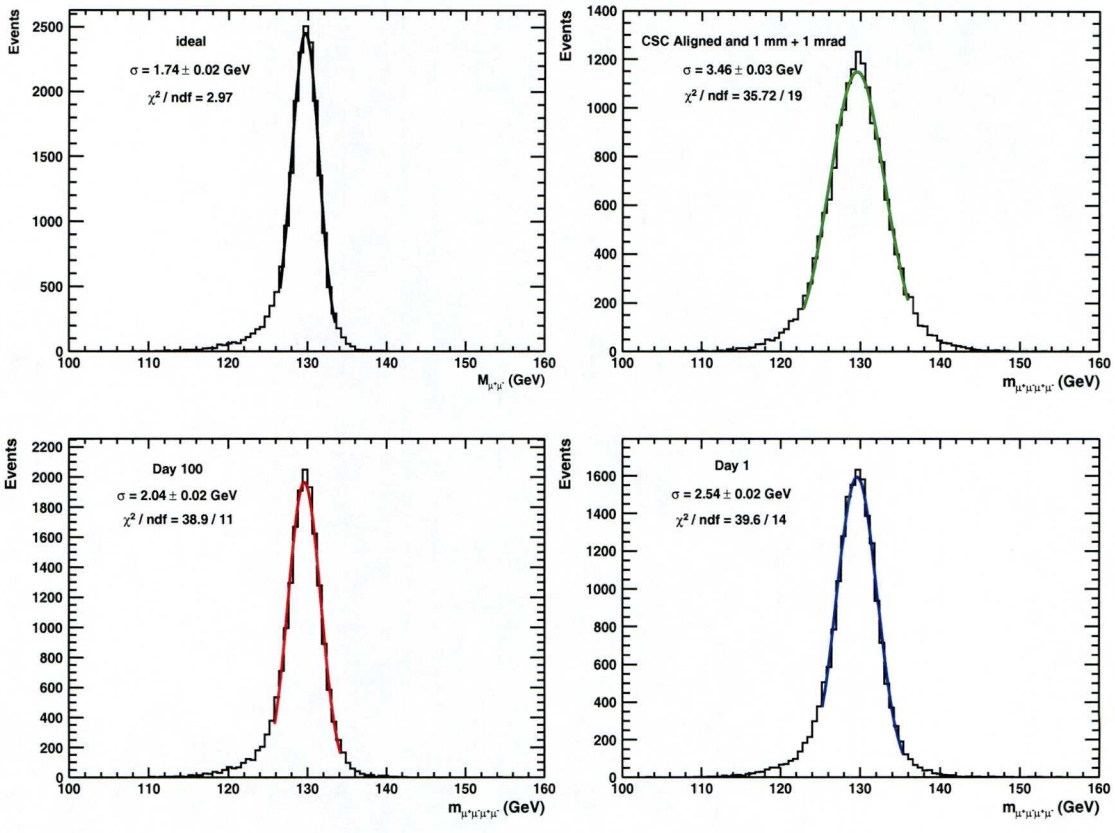

Figure 7.11: *The invariant mass distributions of the four muons in candidate $H \rightarrow ZZ^* \rightarrow 4\mu$ events that have passed all event selection criteria.*

increase with respect to the nominal detector description.

7.4.3 Transverse Impact Parameter Significance

Although impact parameters can be measured for extrapolated muon spectrometer tracks, the resulting resolution is very poor in comparison to that of inner detector tracks and combined muon tracks and, as such, the inner detector completely dominates the measurement of muon impact parameters. The impact of the inner detector misalignments on d_0, σ_{d_0} and d_0/σ_{d_0} for both inner detector muon tracks and combined muon tracks is shown in Figure 7.12. The effects of the misalignments are to broaden the muon d_0 distribution and to shift the σ_{d_0} distribution towards higher values. Furthermore, it would appear that the larger the misalignments, the greater the effect. The observed shift in the muon d_0 distribution for the aligned, as-built inner detector is due to the presence of the residual, global systematic deformations. The fact that the muon d_0 distributions for the inner detector alignment precisions at day 1 and day

		Z Mass Width (GeV)	H Mass Width (GeV)
Nominal		2.28 ± 0.03	1.74 ± 0.02
ID Misaligned	CSC Aligned	2.93 ± 0.03	2.35 ± 0.02
	Day 1	2.89 ± 0.03	2.23 ± 0.02
	Day 100	2.54 ± 0.03	1.86 ± 0.02
MS Misaligned	1 mm + 1mrad	3.43 ± 0.04	2.81 ± 0.02
	Day 1	2.38 ± 0.03	1.86 ± 0.02
	Day 100	2.32 ± 0.03	1.84 ± 0.02
Both Misaligned	CSC Aligned + 1 mm + 1 mrad	4.12 ± 0.05	3.46 ± 0.03
	Day 1	3.18 ± 0.03	2.54 ± 0.02
	Day 100	2.71 ± 0.03	2.04 ± 0.02

Table 7.2: *The widths of the gaussian distributions that were fitted to the invariant mass distributions of the leading di-muon pairs in candidate $H \rightarrow ZZ^* \rightarrow 4\mu$ events that have passed the event preselection.*

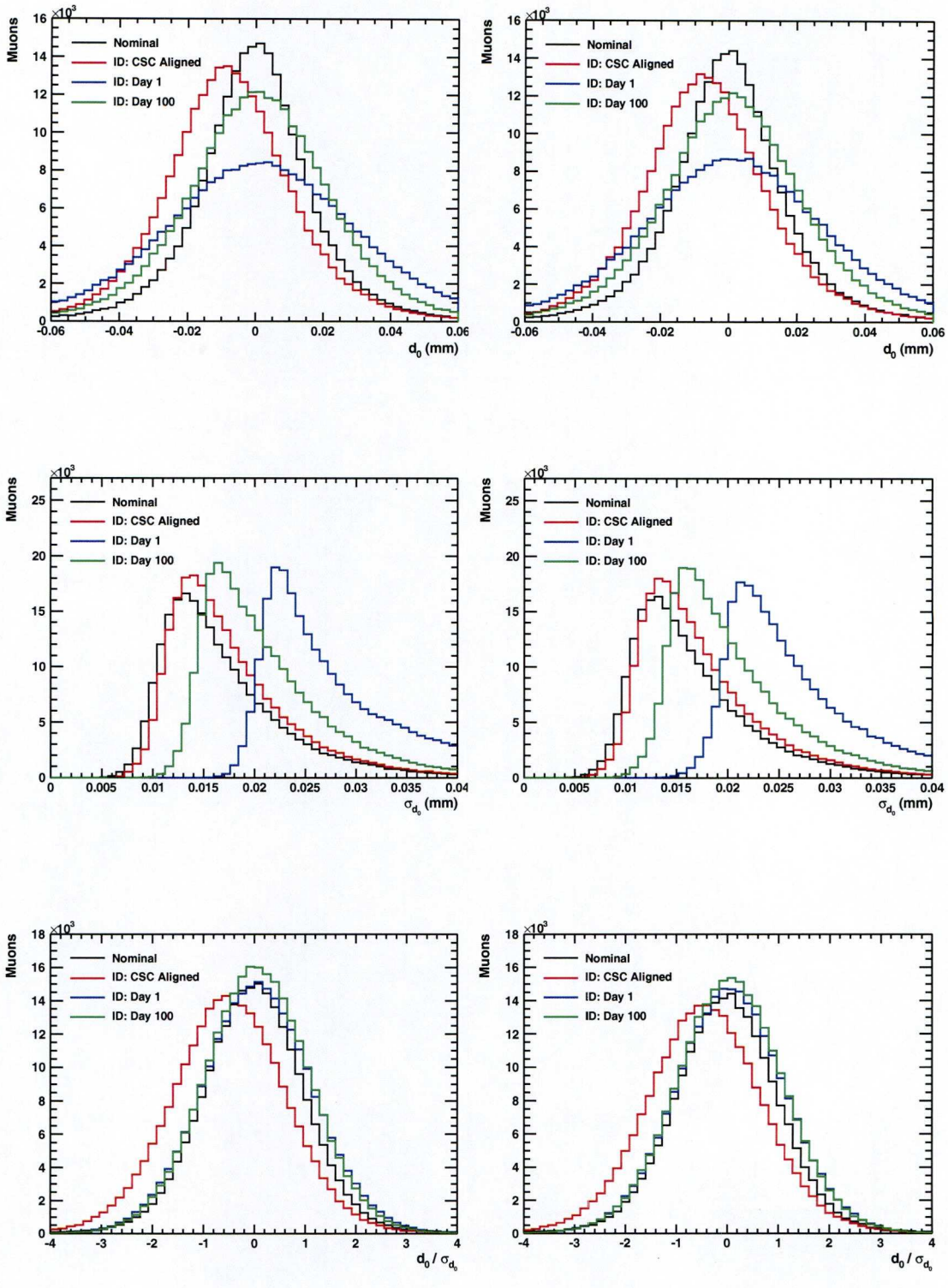

Figure 7.12: *The d_0 (top), σ_{d_0} (middle) and d_0/σ_{d_0} (bottom) distributions of both inner detector muon tracks (left) and combined muon tracks (right) for the different inner detector misalignment scenarios.*

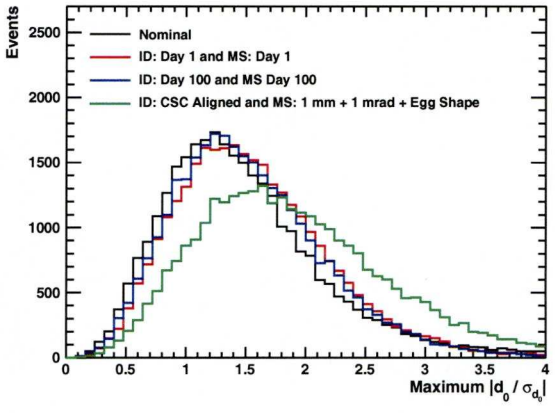

Figure 7.13: *The maximum $|d_0/\sigma_{d_0}|$ of the four selected muons passing the preselection and kinematic reconstruction stages of the event selection for the different inner detector misalignment scenarios.*

100 are centered on zero, is due to the fact that the misalignments are random misalignments. The effects on the d_0 and σ_{d_0} distributions subsequently lead to a slight broadening of the d_0/σ_{d_0} distribution. This broadening of the d_0/σ_{d_0} distribution is somewhat unexpected as by definition the width of this distribution should be equal to unity. A deviation from this value is indicative of a mis-estimation of σ_{d_0}. The fact that the misalignments have an almost identical quantitative effect on both the inner detector muon tracks and the combined muon tracks indicates the dominance of the inner detector measurements in the determination of the impact parameters for the combined muon tracks.

The discriminating variable in the rejection of events from background processes is the maximum impact parameter significance of the four muons in the candidate $H \rightarrow ZZ^* \rightarrow 4\mu$ event. The observed broadening of d_0/σ_{d_0} distribution with the inner detector misalignments subsequently leads to a shift in the distribution of the maximum d_0/σ_{d_0} in candidate $H \rightarrow ZZ^* \rightarrow 4\mu$ events, as shown in Figure 7.13.

7.4.4 Signal Selection Efficiency

The observed degradation of the Z mass width, the H mass width and the broadening of the muon d_0/σ_{d_0} distribution due to the presence of the detector misalignments may lead to a decrease in the signal selection efficiency. To determine this effect, the full $H \rightarrow ZZ^* \rightarrow 4\mu$ analysis, outlined in Chapter 6, has been applied to each of the misaligned

	Nominal	ID Misaligned		MS Misaligned		Both Misaligned	
		Day 1	Day 100	Day 1	Day 100	Day 1	Day 100
Trigger	97.42 (58446)	97.35 (58403)	97.35 (58403)	97.39 (58427)	97.40 (58436)	97.33 (58392)	97.31 (58376)
Preselection	51.92 (31148)	51.76 (31055)	51.77 (31057)	51.82 (31086)	51.83 (31093)	51.92 (31149)	51.91 (31144)
m_{12} Window	43.53 (26112)	43.33 (25997)	43.32 (25987)	43.55 (26127)	43.52 (26107)	43.41 (26042)	43.39 (26033)
m_{34} Window	36.98 (22186)	36.70 (22020)	36.73 (22037)	36.97 (22178)	36.83 (22095)	36.77 (22060)	36.67 (21997)
Calorimeter Isolation	33.68 (20203)	33.42 (20052)	33.44 (20061)	33.64 (20184)	33.53 (20114)	33.46 (20076)	33.38 (20028)
Track Isolation	31.40 (18840)	31.11 (18667)	31.14 (18680)	31.33 (18793)	31.21 (18726)	31.13 (18677)	31.03 (18614)
Impact Parameter Significance	30.55 (18327)	30.61 (18364)	30.75 (18449)	30.48 (18288)	30.35 (18208)	30.67 (18403)	30.65 (18389)
Signal Window	26.39 (15830)	24.53 (14715)	26.08 (15647)	26.01 (15607)	26.01 (15609)	23.56 (14132)	25.53 (15316)

Table 7.3: *The cut flow for the $H \rightarrow ZZ^* \rightarrow 4\mu$ samples with inner detector misalignments. The numbers in the table represent the percentage of events passing each selection cut. The number of events passing each of the selection cuts is also shown in brackets.*

Monte Carlo samples. The cut flow tables for the different misalignment scenarios are shown in Table 7.3. Since the current alignment precisions of the inner detector and the muon spectrometer are known to be better than that described by the as-built detector descriptions, only the alignment precisions at day 1 and day 100 are considered. The most significant effect of the detector misalignments appears in the final stages of the analysis with the application of the signal mass window, with small variations occuring at the other kinematic and impact parameter significance based selection criteria.

For the inner detector misalignments, a significant improvement of 1.55% can be achieved with the alignment precision at day 100, in comparison to the alignment precision at day 1. For the muon spectrometer alignment precision at day 1, the signal selection efficiency is already within 0.38% of the signal selection efficiency achievable with the nominal detector description and very little improvement is made with the alignment resolution at day 100.

When both the inner detector and the muon spectrometer are misaligned, the signal selection efficiency at day 100 is 1.97% greater than that at day 1. Since little improvement is achieved in the muon spectrometer alignment precision between day 1 and day 100, this increase in the signal selection efficiency can be attributed to the improvements in the inner detector alignment precision.

The combined impact of the inner detector misalignments and the muon spectrometer misalignments, with respect to the nominal detector description, leads to a relative decrease in the signal selection efficiency of 10.7% at day 1 and 3.3% at day 100.

7.5 Relative Performance of the Tracking Detectors

Since the day 1 and day 100 alignment constants are designed to represent the expected alignment precision at particular times, the relative performance of the inner detector and the muon spectrometer at these times can be studied, in order to see if there is any benefit in using only one of the two tracking detectors. This is of particular interest to the $H \rightarrow ZZ^* \rightarrow 4\mu$ analysis, in which the vast majority of selected muons will have both an inner detector track and a muon spectrometer track. However, such a study can only be of relevance if the muon reconstruction efficiency remains high, even in the presence of detector misalignments, so that the inner detector tracks can still be identified as muons by matching them to muon spectrometer activity. Fortunately, as

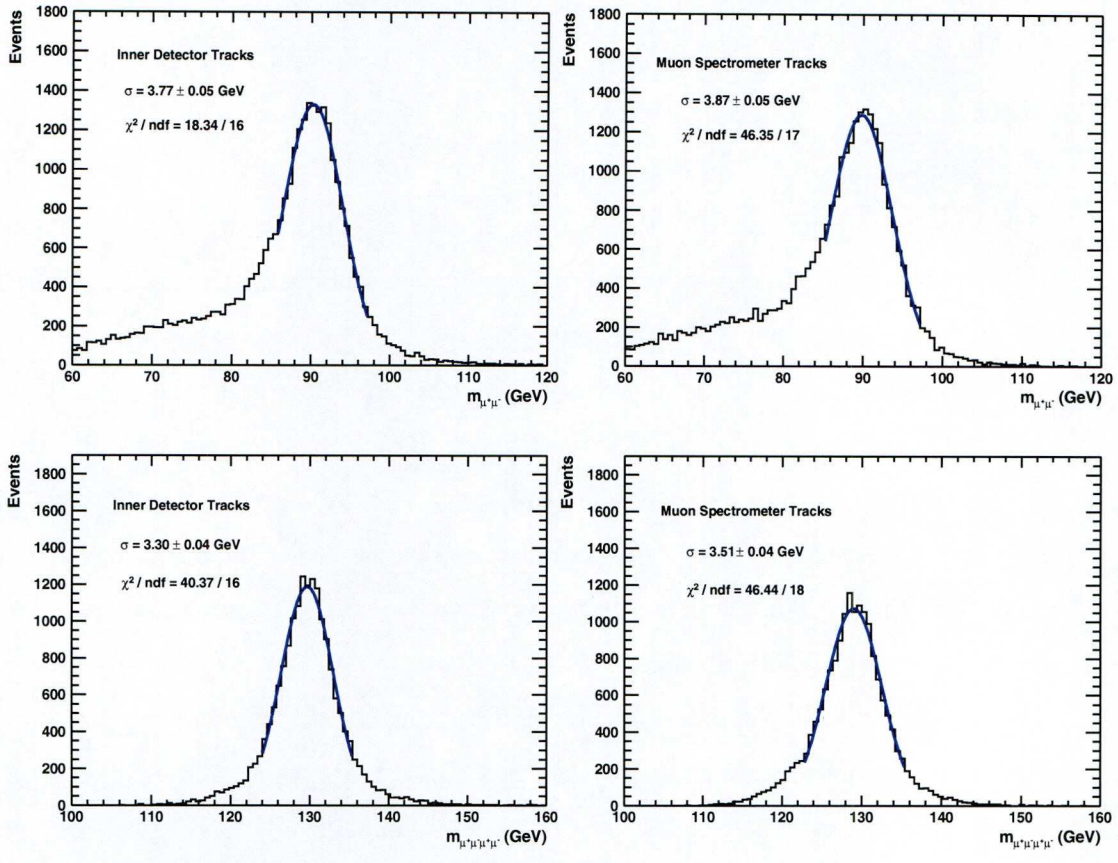

Figure 7.14: *The invariant mass distributions for the leading di-muon pair (top) and all four muons (bottom) in selected candidate H→ZZ*→4μ events, using only the inner detector tracks (left) and the muon spectrometer tracks (right) with the expected alignment precision at day 1.*

can be seen in Figure 7.2, high identification efficiencies can still be maintained even for the most pessimistic alignment scenario considered in these studies.

To compare the relative performance of the two tracking detectors, the H→ZZ*→4μ analysis was repeated twice; once using only inner detector tracks and once using only muon spectrometer tracks. This required that all combined muons in the muon collection were recalibrated prior to the analyses, such that each muon takes on the track parameters of either the inner detector track or the muon spectrometer track from which it was constructed. The resulting invariant mass distributions of the leading di-muon pairs and the four muons in all candidate H→ZZ*→4μ events, for the inner detector only analysis and the muon spectrometer only analysis are shown in Figure 7.14 and Figure 7.15, respectively. The corresponding cut flow tables for these analyses are

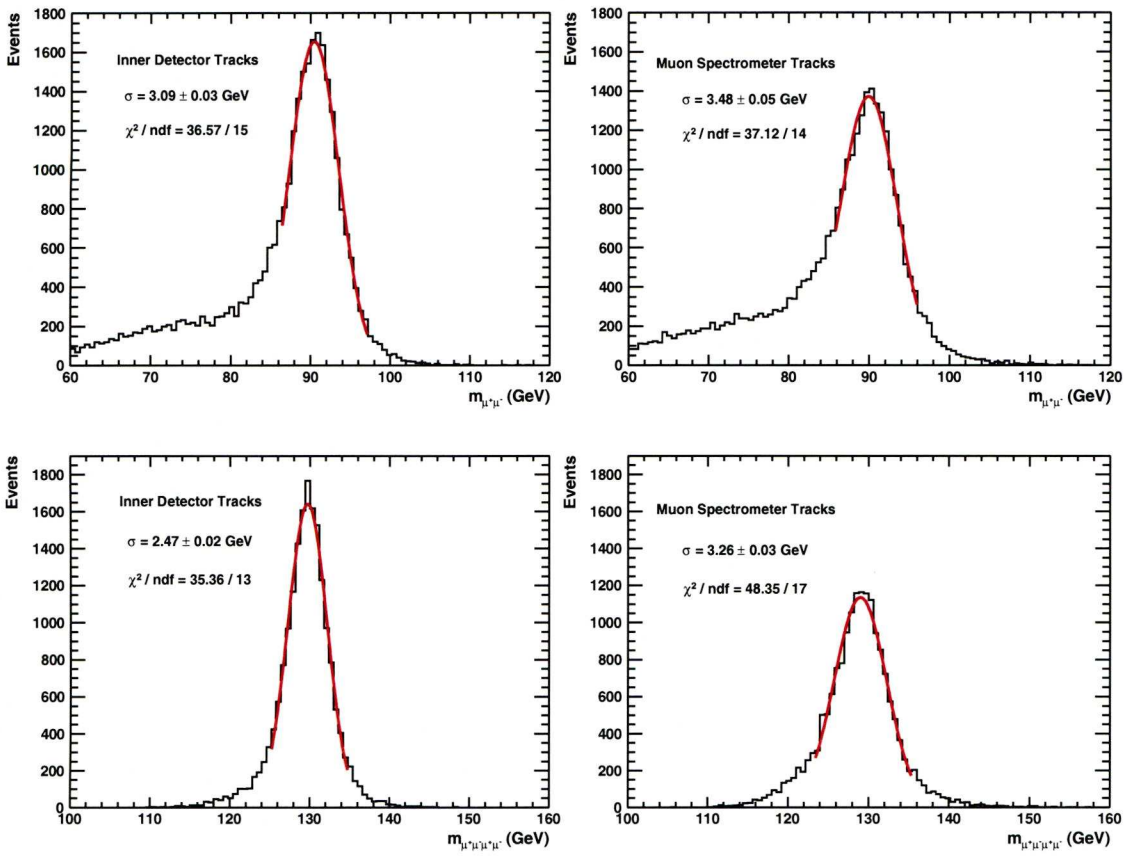

Figure 7.15: *The invariant mass distributions for the leading di-muon pair (top) and all four muons (bottom) in selected candidate $H \rightarrow ZZ^* \rightarrow 4\mu$ events, using only the inner detector tracks (left) and the muon spectrometer tracks (right) with the expected alignment precision at day 100.*

	Nominal	Day 1		Day 100	
		ID Tracks	MS Tracks	ID Tracks	MS Tracks
Trigger	97.42 (58446)	97.33 (58392)	97.33 (58392)	97.31 (58376)	97.31 (58376)
Preselection	51.92 (31148)	51.93 (31156)	50.94 (30562)	51.95 (31168)	50.91 (30540)
m_{12} Window	43.53 (26112)	42.62 (25572)	41.45 (24868)	43.47 (26079)	41.41 (24841)
m_{34} Window	36.98 (22186)	36.25 (21746)	34.87 (20921)	36.82 (22092)	34.73 (20834)
Calorimeter Isolation	33.68 (20203)	33.02 (19808)	31.76 (19054)	33.57 (20140)	31.63 (18976)
Track Isolation	31.40 (18840)	30.77 (18459)	29.52 (17708)	31.22 (18730)	29.37 (17624)
Impact Parameter Significance	30.55 (18327)	30.35 (18206)	29.09 (17453)	30.84 (18503)	29.03 (17419)
Signal Window	26.39 (15830)	19.67 (11803)	17.74 (10643)	23.95 (14371)	18.25 (10949)

Table 7.4: *The cut flow for the $H \rightarrow ZZ^* \rightarrow 4\mu$ sample with both inner detector misalignments and muon spectrometer misalignments. In this case the analysis has been performed using only inner detector tracks or smuon spectrometer tracks. The numbers in the table represent the percentage of events passing each selection cut. The number of events passing each of the selection cuts is also shown in brackets.*

also shown in Table 7.4. The results show that when both tracking detectors are misaligned, the combination of the inner detector and the muon spectrometer provides significantly better performance that the individual tracking detectors, in terms of the signal selection efficiency. The inner detector only analysis leads to a decrease in the relative signal selection efficiency of 25.5% at day 1 and 9.2% at day 100. However, the inner detector still provides better performance than the muon spectrometer. The muon spectrometer only analysis leads to a decrease in the relative signal selection efficiency of 32.8% at day 1 and 30.8% at day 100. The fact that the inner detector appears to be less sensitive to the misalignments than the muon spectrometer further illustrates the importance of the inner detector measurements in the reconstruction of combined muons in the p_{T} range under study.

7.6 Summary

In summary, the impact of the expected alignment precision in the inner detector and the muon spectrometer after 1 day and 100 days of collision data have been studied. In addition, the impact of global deformations in the tracking detectors have also been considered, in particular the effects of relative misalignments between the inner detector and the muon spectrometer. Although these global egg-shape misalignments are not found to have any significant impact on the muon identification and reconstruction performance, the misalignments are very specific and may well be underestimated. The fact that the longitudinal impact parameter of extrapolated muon spectrometer tracks is sensitive to these misalignments, provides a means for their identication and an estimation of their magnitude.

The day 1 and day 100 alignment constants on the other hand are found to have a more significant impact on the muon identification and reconstruction performance. Through the subsequent broadening of the Z and H mass widths and the broadening of the the d_0/σ_{d_0} distribution, the misalignments lead to a relative decrease in the H$\rightarrow$ZZ$^*\rightarrow 4\mu$ selection efficiency of 10.7% at day 1 and 3.3% at day 100. With a given esimate of the alignment precision in the tracking detectors, the results of this study can potentially be extrapolated in order to obtain an estimate for the resulting systematic uncertainty on the H$\rightarrow$ZZ$^*\rightarrow 4\mu$ selection efficiency.

Chapter 8

Conclusion

In order for the ATLAS experiment to achieve its physics potential its detector components must operate stably and reliably over their full lifetimes. However, in the harsh experimental environment of the LHC the inner detector will be subjected to extreme levels of radiation, which can have a significant impact on the performance of its silicon sensors. Previous predictions for the long-term performance of the silicon microstrip sensors of the SCT were based on the Second Order radiation damage parameterisation and involved a number of assumptions which are no longer accurate. As such, the predictions needed to be revised using the most up-to-date operational information available. However, since the initial predictions were made an alternative radiation damage parameterisation, known as the Hamburg parameterisation, has been developed and the two parameterisations were found to show significant variation for long periods of annealing. This thesis presents new measurements of the evolution of both the depletion voltage and the charge collection with annealing time in an irradiated silicon microstrip sensor of the SCT. The data are compared to the predictions of the two radiation damage parameterisations in order to determine which parameterisation best describes the measurements. The data suggest that the effect of annealing on the depletion voltage is slower that that predicted by either of the two radiation damage parameterisations. Furthermore, for long annealing times the measured depletion voltage is significantly less than that predicted by either of the two radiation damage parameterisations. A strong correlation is observed between the measured depletion voltage and the measured charge collection. However, the data also show that with increasing bias voltage the charge collection does not begin to saturate until $\sim$100 V

greater than the measured depletion voltage. This is of particular significance since it is ultimately the charge collection efficiency that limits the sensor performance. In conclusion, although the data appear to be generally more consistent with the predictions of the Hamburg parameterisation, the measurements suggest that predictions for the long-term performance of the SCT silicon microstrip sensors based on either of the two parameterisations would be overly pessimistic.

Within the physics programme of the ATLAS experiment the discovery or exclusion of the Standard Model Higgs boson is of high priority. In searching for this elusive particle the four muon final state will be of particular importance as it provides one of the cleanest experimental signatures. This thesis presents the ATLAS experiment's sensitivity prospects for the Standard Model Higgs boson in the four muon final state with 1 fb^{-1} of 7 TeV collision data. Although the expected number of signal events is small, the signal can be clearly distinguished from the background (of which the $ZZ^{(*)}$ continuum is by far the dominant contribution) for most of the mass points considered. However, the ATLAS experiment cannot exclude the Standard Model Higgs boson in four muon final state alone at 95% confidence level, for any value of m_H. With the inclusion of the $H \rightarrow ZZ^{(*)} \rightarrow 4e$ and $H \rightarrow ZZ^{(*)} \rightarrow 2e2\mu$ decay modes the most sensitive mass region is that around $m_H = 200$ GeV, where an upper limit of 1.3 times the Standard Model prediction is expected. Any potential observation of the Standard Model Higgs boson in the four muon final state will depend crucially upon the performance of the tracking detectors and, in particular, their alignment precision. Since the alignment precisions will not reach design specifications until many months of collision data have been collected, it is essential that the impact of detector misalignments is well understood. This thesis therefore addresses the impact of detector misalignments on the muon identification and reconstruction performance and the subsequent impact on the sensitivity of the ATLAS detector to the Standard Model Higgs boson in the four muon final state. The impact of the detector misalignments on muon reconstruction ultimately leads to a broadening of the Z mass width, the H mass width and the d_0/σ_{d_0} distribution, which is used as a discriminant in the rejection of background processes. The alignment precision expected after 1 day (100 days) of collision data results in a relative increase in the Z and H mass widths of 39% (19%) and 46% (17%), respectively. The subsequent relative decrease in the signal selection efficiency for $m_H = 130$ GeV is 10.7% (3.3%). With a given estimate of the alignment precision in the inner de-

tector and the muon spectrometer, these observations can potentially be extrapolated to obtain an estimate of the resulting systematic uncertainty on the signal selection efficiency.

Bibliography

[1] `https://twiki.cern.ch/twiki/bin/view/Atlas/OSCARSoftwareFramework`.

[2] L. Evans and P. Bryant. LHC Machine. *JINST*, 3:S08001, 2008.

[3] G. Aad et al. The ATLAS Experiment at the CERN Large Hadron Collider. *JINST*, 3:S08003, 2008.

[4] The ATLAS Collaboration. *ATLAS Detector and Physics Performance: Technical Design Report, 2 Volumes.* CERN, 1999. CERN-LHCC-99-014, CERN-LHCC-99-015.

[5] R. Adolphi et al. The CMS Experiment at the CERN LHC. *JINST*, 3:S08004, 2008.

[6] A. A. Alves Jr et al. The LHCb Detector at the LHC. *JINST*, 3:S08005, 2008.

[7] K. Aamodt et al. The ALICE Experiment at the CERN LHC. *JINST*, 3:S08002, 2008.

[8] O. Adriani et al. The LHCf Detector at the CERN Large Hadron Collider. *JINST*, 3:S08006, 2008.

[9] G. Anelli et al. The TOTEM Experiment at the CERN Large Hadron Collider. *JINST*, 3:S08007, 2008.

[10] The ATLAS Collaboration. *ATLAS Inner Detector: Technical Design Report, 2 Volumes.* CERN, 1997. CERN-LHCC-97-016, CERN-LHCC-97-017.

[11] The ATLAS Collaboration. *ATLAS Liquid-Argon Calorimeter: Technical Design Report.* CERN, 1996. CERN-LHCC-96-041.

[12] The ATLAS Collaboration. *ATLAS Tile Calorimeter: Technical Design Report.* CERN, 1996. CERN-LHCC-96-042.

[13] The ATLAS Collaboration. *ATLAS Muon Spectrometer: Technical Design Report.* CERN, 1997. CERN-LHCC-97-022.

[14] P. A. Coe et al. Frequency Scanning Interferometry in ATLAS: Remote, Multiple, Simultaneous and Precise Distance Measurements in a Hostile Environment. *Meas. Sci. Tech.*, 15:2175–2187, 2004.

[15] M. Aleksa et al. Measurement of the ATLAS Solenoid Magnetic Field. *JINST*, 3:P04003, 2008.

[16] R. Bates et al. Reassessment of Cooling Requirements for the ATLAS Barrel SCT. Technical Report ATL-COM-INDET-2009-093, CERN, 2009.

[17] A. Ahmad et al. The Silicon Microstrip Sensors of the ATLAS Semiconductor Tracker. *Nucl. Instr. Meth. A*, 578:98–118, 2007.

[18] Hamamatsu Photonics Co. Ltd., 1126-1 Ichino-cho, Hamamatsu, Shizuoka 431-3196, Japan.

[19] CiS Institut fur Mikrosensorik gGmbH, Konrad-Zuse-Strasse 14, 99099 Erfurt, Germany.

[20] F. Campabadal et al. Design and Performance of the ABCD3TA ASIC for Readout of Silicon Strip Detectors in the ATLAS Semiconductor Tracker. *Nucl. Instr. Meth. A*, 552:292–328, 2005.

[21] H. Spieler. *Semiconductor Detector Systems.* Oxford University Press, 2005.

[22] M. Huhtinen. Simulation of Non-Ionising Energy Loss and Defect Formation in Silicon. *Nucl. Instr. Meth. A*, 491:194–215, 2002.

[23] S. R. Messenger et al. Limits to the Application of NIEL for Damage Correlation. *IEEE Transactions on Nuclear Science*, 51:3201–3206, 2004.

[24] Annual Book of ASTM Standard. *Standard Practice for Characterizing Neutron Energy Fluence Spectra in Terms of an Equivalent Monoenergetic Neutron Fluence*

for Radiation Hardness Testing of Electronics. American Society for Testing and Materials, 1994.

[25] A. Vasilescu and G. Lindstroem. Displacement damage in silicon, online compilation. `http://sesam.desy.de/members/gunnar/Si-dfuncs.html`, 2000.

[26] G. Lutz. *Semiconductor Radiation Detectors.* Springer, 1999.

[27] M. Moll. *Radiation Damage in Silicon Particle Detectors: Microscopic Defects and Macroscopic Properties.* PhD thesis, University of Hamburg, 1999. DESY-THESIS-1999-040.

[28] P. Dervan et al. Evolution of depletion voltage and leakage current. `http://atlas.kek.jp/si-soft/Vd/SCT_evolution.pdf`, 2009.

[29] F. Anghinolfi et al. SCTA - A Rad-Hard BiCMOS Analogue Readout ASIC for the ATLAS Semiconductor Tracker. *IEEE Transactions on Nuclear Science*, 44:298–302, 1997.

[30] P. Hernandez. Neutrino physics. arXiv:1010.4131, 2010.

[31] G. W. Bennett et al. Final Report of the E821 Muon Anomalous Magnetic Moment Measurement at BNL. *Phys. Rev. D*, 73:072003, 2006.

[32] P. W. Higgs. Broken Symmetries, Massless Particles and Gauge Fields. *Phys. Rev. Lett.*, 12:132–133, 1964.

[33] P. W. Higgs. Spontaneous Symmetry Breakdown Without Massless Bosons. *Phys. Rev.*, 145:1156–1163, 1966.

[34] G. S. Guralnik et al. Global Conservation Laws and Massless Particles. *Phys. Rev. Lett.*, 13:585–587, 1964.

[35] I. J. R. Aitchison and A. J. G. Hey. *Gauge Theories in Particle Physics Volume 2.* Institute of Physics Publishing, 2004.

[36] F. Halzen and A. D. Martin. *Quarks and Leptons.* John Wiley and Sons, 1984.

[37] the L3 Collaboration the OPAL Collaboration The ALEPH Collaboration, the DELPHI Collaboration and the LEP Working Group for Higgs Boson Searches. Search for the Standard Model Higgs Boson at LEP. *Phys. Lett. B*, 565:61–75.

[38] The CDF Collaboration and the D0 Collaboration. Combination of Tevatron Searches for the Standard Model Higgs Boson in the W^+W^- Decay Mode. *Phys. Rev. Lett.*, 104:061802, 2010.

[39] The ALEPH Collaboration, The CDF Collaboration, The D0 Collaboration, The DELPHI Collaboration, The L3 Collaboration, The OPAL Collaboration, The SLD Collaboration, The LEP Electroweak Working Group, The Tevatron Electroweak Working Group, and The SLD Electroweak Heavy Flavour Groups. Precision electroweak measurements and constraints on the standard model.

[40] A. Djouadi. The Anatomy of Electro-Weak Symmetry Breaking I: The Higgs Boson in the Standard Model. *Phys. Rept.*, 457:1–216, 2008.

[41] The ATLAS Collaboration. *Expected Performance of the ATLAS Experiment: Detector, Trigger and Physics.* CERN, 2009. CERN-OPEN-2008-020.

[42] C. Anastopoulos et al. ATLAS Sensitivity Prospects for the Standard Model Higgs Boson in the Decay Channel $H \to ZZ^{(*)} \to 4\ell$ at $\sqrt{s} = 10$ and 7 TeV. Technical Report ATL-PHYS-INT-2010-062, CERN, 2010.

[43] S. Dittmaier et al. Handbook of lhc higgs cross sections: 1. inclusive observables. arXiv:1101.0593, 2011.

[44] S. Hassani et al. A Muon Identification and Combined Reconstruction Procedure for the ATLAS Detector at the LHC Using the (MUONBOY, STACO, MuTag) Reconstruction Packages. *Nucl. Instr. Meth. A*, 572:77–79, 2007.

[45] T. Lagouri et al. A Muon Identification and Combined Reconstruction Procedure for the ATLAS Detector at the LHC at CERN.

[46] T. Cornelissen et al. Concepts, Design and Implementation of the ATLAS New Tracking (NEWT). Technical Report ATL-SOFT-PUB-2007-007, CERN, 2007.

[47] D. Wicke. A New Algorithm for Solving Track Ambiguities. Technical Report DELPHI-98-163-PROG-236, DELPHI-98-163-TRACK-92, CERN, 1998.

[48] D. Adams et al. Track Reconstruction in the ATLAS Muon Spectrometer with MOORE. Technical Report ATL-SOFT-2003-007, CERN, 2003.

[49] S. Tarem et al. Mugirl - muon identification in the atlas detector from the inside out. volume 1, pages 617–621, 2006.

[50] T. Sjstrand et al. PYTHIA 6.4 Physics and Manual. *J. High Energy Phys.*, 05:026. 570 p, 2006.

[51] N. Andari et al. Higgs Production Cross Sections and Decay Branching Ratios. Technical Report ATL-PHYS-INT-2010-030, CERN, 2010.

[52] Update to [51].

[53] T. Binoth et al. Gluon-induced qcd corrections to $pp \to zz \to \ell\bar{\ell}\ell'\bar{\ell}'$. arXiv:0807.0024, 2008.

[54] R. Asfandiyarov et al. Production Cross Section of the Higgs Boson and Other Standard Model Processes in pp Collisions at Different Center-of-Mass Energies. Technical Report ATL-COM-PHYS-2009-051, CERN, 2009.

[55] K. Nakamura and others (Particle Data Group). Review of Particle Physics, 2010-2011. *J. Phys. G: Nucl. Part. Phys.*, 37:075021, 2010.

[56] S. Frixione et al. Matching NLO QCD Computations and Parton Shower Simulations. *J. High Energy Phys.*, 06:029. 69 p, 2002.

[57] The ATLAS Collaboration. ATLAS Sensitivity Prospects for Higgs Boson Production at the LHC Running at 7 TeV. Technical Report ATL-PHYS-PUB-2010-009, CERN, 2010.

[58] The ATLAS Collaboration. ATLAS Sensitivity Prospects for Higgs Boson Production at the LHC Running at 7, 8 or 9 TeV. Technical Report ATL-PHYS-PUB-2010-015, CERN, 2010.

[59] J. Alison et al. Alignment of the Inner Detector Using Misaligned CSC Data. Technical Report ATL-COM-INDET-2008-014, CERN, 2009.

[60] A. Ahmad et al. Inner Detector As-Built Detector Description Validation for CSC. Technical Report ATL-COM-INDET-2007-012, CERN, 2007.

[61] E. Bouhova-Thacker et al. Impact of Inner Detector and Muon Spectrometer Misalignments on Physics. Technical Report ATL-PHYS-INT-2009-067, CERN, 2009.

[62] M. Schott et al. Impacts of Misalignment Effects on the Muon Spectrometer Performance. Technical Report ATL-MUON-PUB-2007-006, CERN, 2007.

[63] J. C. Barriere et al. The Alignment System of the Barrel Part of the ATLAS Muon Spectrometer. Technical Report ATL-MUON-PUB-2008-007, CERN, 2008.

[64] S. Aefsky et al. The Optical Alignment System of the ATLAS Muon Spectrometer Endcaps. Technical Report ATL-MUON-PUB-2008-003, CERN, 2008.